Studies on microscopic solvation process of alkali-metal atoms and NH_4 radical in clusters

TAKASU Ryozo

Department of Functional Molecular Science
School of Mathematical and Physical Science
The Graduate University for Advanced Studies

1996

Contents

Chapter I
General introduction

1. Preface

Electrons and metal ions in fluids play important roles in many aspects of chemical and biological phenomena and have been the subject of numerous investigations for many years. Although experimental and theoretical studies have attempted to understand the nature and the dynamics of solvation for these species, its microscopic aspect has not yet been fully understood. Recently, advances in molecular beam technique allow us to prepare various kinds of the gas-phase clusters and open new approaches to a microscopic investigation of the excess electrons and metal ions in fluids. The study of successively large clusters is analogous to modeling the process of solvation and provides us information on microscopic solvation. Thus, the cluster research may offer an opportunity to bridge the gap between the gas and condensed phases.

The purpose of this work is to investigate the geometrical structure, electronic structure, reactivity, and the energy dissipation process of the clusters containing metal atoms/ions and hypervalent molecules such as NH_4 radical to get information on the dynamics of microscopic solvation process.

In this chapter, first, the backgrounds, problems, and interests for the study on these clusters are described, and secondly, the contents of each chapter are addressed.

Electrons and metal ions in bulk solution

Studies of the properties of solutions have been recorded since antiquity. However, a concept of solvation as mutual interaction of a solute and a solvent is of much more recent origins in the early 19th century. Since then the solvation process has been the subject of intensive studies, because it is one of the most widespread phenomena on the earth. Many concepts have been established for the solvation phenomena, however, the details are beyond the scope of this chapter.

The solvation of electrons and metal ions has been the central issue among these studies. It has been generally accepted that there is a real boundary between the ion present in the solution surrounding the molecules nearest to it and the remaining mass of the solvent. And also, it is usually assumed that two solvation shells are situated around the ion, namely, the first and the second. The first solvent shell contains the molecules of the solvent in the direct vicinity of the ions, and this shell moves in the solvent together with the ion. The structure of this region is more orderly than the bulk solvent. The number of molecules of the solvent is termed the coordination number of the given ion. The second shell provides an intermediate zone between the first solvent shell and the bulk solvent.

As for the metal-ion solvation, the coordination number and the structure of the first solvent shell have been extensively studied using various spectroscopic methods such as optical spectroscopy, magnetic

resonance, dielectric spectroscopy, EXAFS, X-ray diffraction, and neutron diffraction [1]. However, in many cases more than one structural model may be compatible with the data obtained by these methods and the structural information are available in limited concentration ranges or for a special region within the time scale of dynamical processes. Perhaps the mass-spectrometric gas-phase solvation studies may provide the most valuable information as mentioned in the next section.

Electrons in polar fluids have intrigued scientists nearly over a century since the first observation of the solvated electrons in liquid ammonia [2]. Injection of electrons into liquid or solid water and ammonia gives rise to a localization of excess electrons in sites, which have been described as the clusters of H_2O and NH_3 molecules within the bulk [3], though the molecules themselves have no stable negative-ion states. Their broad absorption spectrum and other properties suggest a structure similar to an F-center in alkali halide crystals.

Despite much experimental and theoretical interests, the microscopic structure of these bulk phase states remains unclear. In 1946, Ogg introduced a cavity model to account for a number of observations pertaining to dilute solutions of alkali metals in liquid ammonia [4-7]. In this model, solvated electrons and dielectrons occupy cavities within the solvent, analogous to the F-center known to be single electrons and electron pairs, respectively, occupying anion vacancies in the crystals. This model was widely accepted, however, much of the evidence that Ogg used to support his proposal has turned to be incorrect or unsubstantiated. More recently, solvated solvent-anion complex (SAC) models of solvated electrons have been proposed to account for a number of their properties not adequately accounted for by the cavity model [8-10]. These models are based on the observation that measured paramagnetic shifts of nuclear resonance in dilute alkali metal-ammonia solutions indicate the existence

of a large unpaired electron ^{14}N contact interaction [11]; this fact is attributable to solvated electrons in close association with ammonia molecules in spite of the extremely narrow single line observed in the EPR spectrum of the electron. And also, the EPR spectra of e^-(aq) produced by irradiation of ice and glassy mixed-water have found to contain structural information and typically show an electron environment of 4-6 nearly equivalent H atoms [12]. A hydrated, highly distorted H_2O^- species have been suggested most recently to account for the results of photokinetic experiments on ultrafast time scale [13,14]. Although these studies provided us some insights into the intrinsic nature of solvated electrons, they also indicate implicitly that it seems to be impossible to get a definitive understanding for these issues with the bulk experiments alone. Under these circumstances, a new approach such as the cluster research for the solvated electron seem to be quite informative as mentioned in the next section.

Cluster researches on solvated electrons and solvated metal ions

Technological advances in the last decade have made possible the intensive exploration of a new realm of matter, to which has now been arisen widespread attention for a variety of reasons. This realm is given various names such as clusters, small particles, etc. depending on one's point of view. Our new ability to explore this intermediate range of matter causes us to reassess our understanding of its limiting forms, molecules or atoms versus bulk solids and liquids. Up to now, the physical and chemical properties of clusters have been extensively investigated for the purpose to bridge the gap between molecular or atomic systems and the condensed phase [15-17]. One of the remarkable

aspects of cluster research pertains to the exploration of microscopic solvation phenomena of an electron or a metal ion embedded in a cluster of solvent molecules. The experimental and theoretical studies of such heteroclusters allow for the investigation of specific cluster size effect, *i.e.*, the buildup of the solvation shell in small- and medium sized clusters, and the exploration of the gradual transition from the finite system to the infinite bulk medium for large clusters. In particular, the microscopic solvation of electrons and metal ions is of central importance for the understanding of the structure, energetics, spectroscopy, dynamics, and reaction kinetics in clusters.

As for the metal ion solvation, the gas-phase experiments on cluster ions have been used to study solvent shell structure [38-42]. Accurate characterization of properties of cluster ions will help us to develop the fundamental metal ion-neutral interaction potentials needed for structural modeling. Especially for the structural aspects of clusters containing metal and non-metal ions, high-pressure mass spectroscopy (HPMS) was perhaps the first experimental method proved to be successful [38]. These investigations have yielded a wealth of thermodynamic information such as enthalpies, entropies, and free energies of association for ion-neutral complexes. Sharp changes in the enthalpy of association as a function of cluster size were used to infer the number of molecules in the first solvent shell. Since the temperature of the solvated ions is well characterized in the HPMS technique, the results can be readily compared with solution studies or theoretical simulations [43]. However, with successively larger cluster ions, the enthalpy of association rapidly approaches the value of the enthalpy of vaporization of the bulk solvent. This has limited the application of HPMS to solvation studies of ions with small ion radii and low solvation numbers (typically $n \leq 6$).

Although the spectroscopic studies are expected to provide a much more detailed look into the properties of cluster ions, they are quite limited in number.

As for the electron solvation, negatively charged free water $(H_2O)_n^-$ (for $n \geq 2$) and ammonia $(NH_3)_n^-$ (for $n \geq 35$) clusters have been recently prepared by localization during the cluster nucleation process or *via* capture of very low-energy electrons by cold water clusters [18-22]. More recently, the photoelectron spectra of $(H_2O)_n^-$ (for n=2,6,7 and n=2-69) and $(NH_3)_n^-$ (for n=41-1100) have been examined, and vertical detachment energies (VDEs) has been determined form the spectra [23,24]. For both systems, the VDEs of the cluster anions increase smoothly with increasing sizes and depend on $n^{-1/3}$. The VDE ($n=\infty$) value obtained by extrapolation is found to be very close to the photoelectric threshold energy for the corresponding solvated electron system in the condensed phase. After these studies, the excess electron states in these clusters have been examined theoretically by employing the quantum path-integral molecular dynamics method [25-32]. These studies revealed that electron localization in polar molecular clusters occurs *via* surface or internal modes depending on cluster size and chemical composition, yielding results in agreement with the experimental observations; water cluster anions to be surface states for n<32 and internal states for n>64, with the transition occurring between n=32-64.

As mentioned in the previous section, the solvated electron has been observed traditionally in dilute solutions of alkali metals. Preparation of molecular clusters in supersonic beams allows us to study such aggregates as free species and thus to follow the building up of the liquid phase from its constituents.

IR spectroscopy has been used to study the gas-phase solvation of Cs^+ ion [49-52]. On the other hand, Farrar's group and Fuke's group have

performed electronic photodissociation experiments on clusters containing monovalent alkaline-earth metal ions such as $Sr^+(NH_3)_n$, $Mg^+(H_2O)_n$ and $Ca^+(H_2O)_n$ [53-62]. In these studies, the stabilization of the ion-pair state as a function of the cluster size has been examined by the photodissociation spectroscopy.

Negative-ion photoelectron spectroscopy (PES) of clusters have had a direct impact on the questions concerning the nature of the solvated electron as mentioned previously [23,24]. As for the spectroscopic studies on solvated metal cluster ions, it is quite limited to that measurements of the photoelectron spectra of metal ions (such as Cu^- and Cu_2^-) embedded in water clusters have been made [80] and other few works; though the photoelectron spectroscopy has been applied for various systems such as metal clusters [44-46], semiconductor clusters [47], molecular clusters [48] and solvated halogen clusters [81,82]. PES has advantages that the electronic structure in the neutral state as well as electron binding energies are able to observe simultaneously. Therefore, the PES is a powerful method to characterize the size-dependent behavior of electron in clusters. The microscopic solvation and solvated electron formation processes of Li, Na, Na_2 in solvent clusters are examined by means of PES. The details will be described in Chapters III and IV.

Recently, the ionization potentials (IPs) of neutral Na [33-35] and Cs [36-37] atoms embedded in polar molecular clusters have been studied by Hertel and coworkers and Fuke and coworkers. Interestingly, for both metal atoms, the limiting value of water clusters for $n \geq 4$ coincides with the estimated IP of an excess electron solvated in bulk ice. Similar results are also obtained in the case of the Li system. The details will be described in Chapter III.

The NH_4 radical is known to be a typical Rydberg radical. It is isoelectronic with alkali-metal atom; a weakly bound 3*s* electron is

orbiting around the NH_4^+ core. The NH_4 radical has been firstly characterized in the gas phase by the emission spectroscopy [63], and the existence of mercury amalgams of ammonium and alkylammonium radicals has long been anticipated. In the gas phase, NH_4 has a very short lifetime because of the H atom tunneling reflecting the shallow potential well on its H atom elimination coordinate. The nature of NH_4 radical in clusters has been the subject of both experimental and theoretical studies and it has been found to have a long lifetime in small ammonia clusters [63-72]. Since NH_4 is isoelectronic with alkali atoms as mentioned above, the ammoniated NH_4 clusters may serve as a new testing material to get further insight into the electron localization modes in clusters. Moreover, the study on the stability of these clusters as a function of the number of solvent molecules may provide us some clues to reveal the aforementioned long standing problems in bulk solution. Time-resolved formation and decay process of NH_4 in ammonia cluster and stability of them are examined using the femto and nanosecond laser technique, and these will be described in Chapter V.

3. Scope for chapters

In order to reveal microscopic aspects of solvation dynamics in fluids, the size-dependent properties of the solvated clusters containing alkali-metal atoms/ions and NH_4 radical have been examined in the present studies. The photoionization experiments for the neutral clusters containing alkali-metal atoms and radical are carried out using a reflection-type time-of-flight mass spectrometer combined with techniques of femtosecond and nanosecond laser spectroscopies. Moreover, the photoelectron spectroscopy experiments using a magnetic-

bottle type photoelectron spectrometer have been examined for the clusters containing the alkali-metal atom anions to get information on their electronic structures. The details of the apparatus and the principles of these spectroscopies are described in Chapter II. The details for the experimental methods are described in the experimental section of each chapter.

In Chapter III, the photoionization and photodetachment processes of Li, Li^- and Na^- solvated with ammonia and water molecules are discussed in relation to the formation process of solvated electrons in the dilute alkali atom solution. The ionization potentials (IPs) of the Li-containing clusters are determined as a function of cluster size. The results show the convergence of IPs to the bulk limits with increasing *n*. In addition to the photoionization experiments, the photoelectron spectra (PESs) of their cluster anions are also investigated to get further information on the solvation state of neutral alkali atoms in clusters. In ammonia clusters, the drastic changes in the electronic structures of metal atoms are observed with increasing the cluster size. These features of IPs and PESs are discussed in conjunction with the ion-pair state formation [73,74].

In Chapter IV, the photoelectron spectra of Na dimer anion in ammonia clusters are discussed. In the PESs, the anomalous spectral behaviors specific to the electronic states are observed. The solvation process of Na_2 in solvent clusters are discussed with the results of theoretical calculations [75].

In Chapter V, the formation processes and stability of NH_4 radical in ammonia clusters are discussed. In section 1, the formation, solvation and decomposition processes of NH_4 radical and its ammoniated clusters are examined using the femtosecond and nanosecond pump-probe experiments. The lifetime of NH_4 is found to elongate by more than 10^6 times in ammonia clusters. Moreover, the ammonia dimer ion is found to

be formed mainly through the one-photon ionization of a new photolysis product such as an excited state NH_4*—NH_2 [76,77]. In Section 2, the stability and electronic structure of NH_4 in ammonia and ammonia-water binary clusters are discussed. The IPs of the solvated NH_4 are measured as a function of cluster size. The IP results show the similar trend to those for alkali atoms as mentioned previously; NH_4 behaves as alkali atoms and may form a Rydberg-type ion-pair state in small ammonia clusters [77-79].

References for Chapter I

[1] Conway, B. E.; *Ionic Hydration in Chemistry and Biophysics* (Elsevier, Amsterdam 1981).
[2] Kraus, C. A. *J. Am. Chem .Soc.* **1908**, *30*, 1323.
[3] Boag, J. W.; Hart, E. J. *J. Am. Chem. Soc.* **1962**, *84*, 4090.
[4] Ogg, Jr., R. A. *Phys. Rev.* **1946**, *69*, 668.
[5] Ogg, Jr., R. A. *Phys. Rev.* **1946**, *69*, 243; 544.
[6] Ogg, Jr., R. A. *J. Am. Chem. Soc.* **1946**, *68*, 155.
[7] Ogg, Jr., R. A. *J. Chem. Phys.* **1946**, *14*, 295.
[8] Feng, D. -F.; Kevan, L. *Chem. Rev.* **1980**, *80*, 1.
[9] Hameka, H. F.; Robinson, G. W.; Marsden, C. J. *J. Phys. Chem.* **1987**, 91, 3150.
[10] Tuttle, Jr. T. R.; Golden, S. *J. Phys. Chem.* **1991**, *95*, 5725.
[11] Golden, S.; C. Guttman, and T. R. Tuttle, Jr., *J. Chem. Phys.* **44**, 3791 (1966).
[12] Kevan, L. *Acc. Chem. Res.* **14**, 138 (1981).
[13] Alfano, J. C.; Walhout, P. K.; Kimura, Y.; Barbara, P. F. *J. Chem. Phys.* **1993**, *98*, 5996.
[14] Kimura, Y.; Alfano, J. C.; Walhout, P. K.; Barbara, P. F. *J. Phys. Chem.* **1994**, *98*, 3450.
[15] Castleman, Jr., A. W.; Keesee, R. G. *Science* **1988**, *241*, 36.
[16] Jortner, J. *Ber. Bunsenges. Phys. Chem.* **1987**, *88*, 188.
[17] *Physics and Chemistry of Small Clusters*, edited by Jena, P.; B. K. Rao, B. K.; Khanna, S. N. vol. 158 of *NATO ASI Series B* , (Plenum, New York, 1987).
[18] Haberland, H.; Ludewigt, C.; Schindler, H. -G.; Worksnop, D. R. *Surf. Sci.* **156**, 157 (1985).
[19] Haberland, H.; Schindler, H. -G.; and Worksnop, D. R. *J. Chem. Phys.* **1984**, *81*, 3742.
[20] Knapp, M.; Echt, O.; Kreisle, D.; Recknagel, E. *J. Chem. Phys.* **1986**, *85*, 636.
[21] Knapp, M.; Echt, O.; Kreisle, D.; Recknagel, E. *J. Phys. Chem.* **1987**, **91**, 2601.
[22] Haberland, H.; Schindler, H. -G.; Worksnop, D. R. *Ber. Bunsenges. Phys. Chem.* **1984**, *88*, 270.
[23] Coe, J. V.; Lee, G. H.; Eaton, J. G.; Sarkas, H. W.; Bowen, K. H.; Ludewigt, C.; Haberland, H.; Worsnop, D. R. *J. Chem. Phys.* **1990**, *92*, 3980.
[24] Lee, G. H.; Arnold, S. T.; Eaton, J. G.; Sarkas, H. W.; Bowen, K. H. *Z. Phys.* **1991**, *D20*, 9.
[25] Barnett, R. N.; Landman, U.; Cleveland, C. L.; Jortner, J. *Phys. Rev. Lett.* **1987**, *59*, 811.
[26] Barnett, R. N.; Landman, U.; Cleveland, C. L.; Jortner, J. *J. Chem. Phys.* **1987**, *88*, 4421, 4429.
[27] Landman, U.; Barnett, R. N.; Cleveland, C. L.; Scharf, D.; Jortner, J. *J. Phys. Chem.* **1987**, *91*, 4890.
[28] Barnett, R. N.; Landman, U.; Cleveland, C. L.; Kestner N. R.; Jortner, J. *J. Chem. Phys.* **1988**, *89*, 6670.
[29] Barnett, R. N.; Landman, U.; Cleveland, C. L.; Kestner, N. R.; Jortner, J. *Chem. Phys. Lett.* **1988**, *148*, 249.
[30] Barnett, R. N.; Landman, U.; Nitzan, A. *J. Chem. Phys.* **1988**, *89*, 2242.

[31] Barnett, R. N.; Landman, U. *Phys. Rev. Lett.* **1993**, *70*, 1775.
[32] Martyna, G. J.; Klein, M. L. *J. Chem. Phys.* **1992**, *96*, 7662.
[33] Schulz, C. P.; Haugstätter, R.; Tittes, H. -U.; Hertel, I. V. *Phys. Rev. Lett.* **1986**, *57*, 1703.
[34] Schulz, C. P.; Haugstätter, R.; Tittes, H. -U.; Hertel, I. V. *Z. Phys.* **1988**, *D10*, 279.
[35] Hertel, I. V.; Hüglin, C.; Nitsch, C.; Schulz, C. P.; *Phys. Rev. Lett.* **1991**, *67*, 1767.
[36] Misaizu, F.; Tsukamoto. K.; Sanekata, M.; Fuke, K. *Chem. Phys. Lett.* **1992**, *188*, 241.
[37] Fuke, K.; Misaizu, F.; Tsukamoto, K.; Sanekata, M. In *Physics and Chemistry of Finite Systems*; edited by Jena, P.; Khanna, S. N.; Rao, B. K. Vol. II, p. 925 (Kluwer, Dordrecht, 1992).
[38] Kebarle, P. *Ann. Rev. Phys. Chem.* **1977**, *28*, 445.
[39] Mark, T. D.; Castleman, Jr., A. W. *Adv. Rev. Mol. Phys.* **1986**, *20*, 65.
[40] Keesee, R. G.; Castleman, Jr., A. W. *J. Phys. Chem. Ref. Data.* **1986**, *15*, 1011.
[41] Armentrout, P. B. *Ann. Rev. Phys. Chem.* **1990**, *41*, 313.
[42] Bieske, E. J.; Maier, J. P. *Chem. Rev.* **1993**, *93*, 2603.
[43] Kochanski, E.; Constantin, E. *J. Chem. Phys.* **1987**, *87*, 1661.
[44] Hoe, J.; Ervin, K. M.; Lineberger, W. C. *J. Chem. Phys.* **1990**, *93*, 6987.
[45] Ganteför, G.; Gansa, M.; Meiwes-Broer, K. -H.; Lutz, H. O. *J. Chem. Soc. Faraday Trans.* **1990**, *86*, 2483.
[46] Cheshnovsky, O.; Taylor, K. J.; Conceicao, J.; Smalley, R. E. *Phys. Rev. Lett.* **1990**, *64*, 1785.
[47] Yang, S. H.; Pettiette, C. L.; Conceicao, J.; Cheshnovsky, O.; Smalley, R. E. *Chem. Phys. Lett.* **1987**, *139*, 233.
[48] Posey, L. A.; Johnson, M. A. *J. Chem. Phys.* **1988**, *88*, 5383.
[49] Liu, W. -L.; Lisy, J. M. *J. Chem. Phys.* **1988**, *89*, 605.
[50] Draves, J. A.; Luthey-Schulten, Z.; Liu, W. L.; Lisy, J. M. *J. Chem. Phys.* **1990**, *93*, 4589.
[51] Huisken, F.; Kulcke, A.; Laush, C. L.; Lisy, J. M. *J. Chem. Phys.* **1991**, *95*, 3924 .
[52] Selegue, T. S.; Moe, N.; Draves, J. A.; Lisy, J. M. *J. Chem. Phys.* **1992**, *96*, 7268.
[53] Shen, M. H.; Winniczek, J. W.; Farrar, J. M. *J. Phys. Chem.* **1987**, *91*, 6447.
[54] Shen, M. H.; Farrar, J. M. *J. Phys. Chem.* **1989**, *93*, 4386.
[55] Shen, M. H.; Farrar, J. M. *J. Chem. Phys.* **1991**, 94, 3322.
[56] Donnelly, S. G.; Farrar, J. M. *J. Chem. Phys.* **1993**, *98*, 5450.
[57] Schumuttenmaer, C. A.; Quan, J.; Donnelly, S. G.; DeLuca, M. J.; Varley, D. F.; DeLouise, L. A.; Miller, R. J. D.; Farrar, J. M. *J. Phys. Chem.* **1993**, *98*, 3077.
[58] Misaizu, F.; Sanekata, M.; Tsukamoto, K.; Fuke, K.; Iwata, S. *J. Phys. Chem.* **1992**, *96*, 8259.
[59] Fuke, K.; Misaizu, F.; Sanekata, M.; Tsukamoto, K.; Iwata, S. *Z. Phys.* **1993**, *D26*, 180.
[60] Misaizu, F.; Sanekata, M.; Fuke, K.; Iwata, S. *J. Chem. Phys.* **1994**, *100*, 1161.

[61] Sanekata, M.; Misaizu, F.; Fuke, K.; Iwata, S.; Hashimoto, K. *J. Am. Chem. Soc.* **1995**, *117*, 747.
[62] Sanekata, M.; Misaizu, F.; Fuke, K. *J. Chem. Phys.* **1996**, *104*, 9768.
[63] Herzberg. G. *Faraday Discuss. Chem. Soc.* **1981**, *71*, 163.
[64] Herzberg, G. *J. Astrophys. Astr.* **1984**, *5*,138.
[65] Watson, J. K. G. *J. Mol. Spectrosc.* **1984**, *107*, 124.
[66] Alberti, F.; Huber, K. P.; Watson, J. K. G. *J. Mol. Spectrosc.* **1984**, *107*, 133.
[67] Gellene, G. I.; Cleary, D. A.; Porter, R. *J. Chem. Phys.* **1982**, *77*, 3471.
[68] Gellene, G. I.; Porter, R. F. *J. Phys. Chem.* **1984**, *88*, 6680.
[69] Kassab, E.; Evleth, E. M. *J. Am. Chem. Soc.* **1987**, *109*, 1653.
[70] Evleth, E. M.; Cao, H. Z.; Kassab, E. in *Photophysics and photochemistry*, F.Lahmani ed. p.479 (Elsevier, Amsteram, 1985)
[71] Kassab, E.; Evleth, E. M. *J. Am. Chem. Soc.* **1987**, *109*, 1653.
[72] Evleth, E. M.; Kassab, E. *Pure & Appl. Chem.* **1988**, *60*, 209.
[73] Takasu, R.; Hashimoto, K.; Fuke, K. *Chem. Phys. Lett.* **1996**, *258*, 94.
[74] Takasu, R.; Misaizu, F.; Hashimoto, K.; Fuke, K. *J. Phys. Chem.* **1997**, *A101*, 3078.
[75] Takasu, R.; Misaizu, F.; Hashimoto, K.; Fuke, K. to be submitted.
[76] Fuke, K.; Takasu, R. *Bull. Chem. Soc. Jpn.* **1995**, *68*, 3309.
[77] Fuke, K.; Takasu, R. in *Structures and Dynamics of Clusters* Kondow, T.; Kaya. K.; Terasaki, A. eds. Universal Academy Press Inc. Tokyo, Japan. 1996, p.219.
[78] Fuke, K.; Takasu, R.; Misaizu, F. *Chem. Phys. Lett.* **1994**, *229*, 597.
[79] Takasu, R.; Fuke, K.; Misaizu, F. *Surf. Rev. Lett.* **1996**, *3*, 353.
[80] Misaizu, F.; Tsukamoto, K.; Sanekata, M.; Fuke, K. *Laser Chem.* **1995**, *15*, 195.
[81] Markovich, G.; Giniger, R.; Levin, M.; Cheshnovsky, O. *J. Chem. Phys.* **1991**, *95*, 9416.
[82] Arnold, D. W.; Bradforth, S. E.; Kin, E. H.; Neumark, D. M. *J. Chem. Phys.* **1995**, *102*, 3510.

Chapter II
Experimental

1. Time-of-flight mass spectrometer

Figure II-1 shows the schematic view of an apparatus for photoionization experiments. This system is a reflectron-type time-of-flight (TOF) mass spectrometer which consists of a three-stage differentially evacuated chambers, namely, cluster source, second and reflectron chambers. The cluster source chamber (*h*400, *d*400, *w*400 mm) is evacuated by two oil diffusion pumps (ULVAC/ULK-10A, 3000 *l*/s) backed by an evacuation unit (ULVAC/YM-300C) which consists of a mechanical booster and an oil rotary pumps. A pulsed nozzle (General Valve/Series 9) driven by a driver unit (General Valve/IOTA-ONE) is used as a cluster beam source. For metal-containing clusters, a conical throat is attached in front of the orifice of the pulsed nozzle. Sample metal rod (5 mm in diameter) is placed across the throat, and vaporization laser (second harmonic of Nd:YAG laser; Quanta-Ray/GCR-12, typically 2mJ/pulse) is collimated by a convex lens (*f*=500 mm) on the rod. For water-containing clusters, a reservoir is placed just behind the nozzle and is designed to be able to charge water externally. The temperatures of the nozzle and reservoir, monitored by thermocouple, are kept at *ca.* 120 and 80 °C to avoid clogging of the

nozzle orifice. The cluster beam is introduced into the second chamber through a skimmer. The second chamber (*h*400, *w*400, *d*600 mm) is evacuated by an oil diffusion pump (Edwards/Diffstak 250, 2000 *l*/s) backed by an evacuation unit (ULVAC/YM-100C) consisting of a mechanical booster and an oil rotary pumps. The reflectron TOF mass spectrometer shown in Figure II-2 is composed of the following parts; the double acceleration region designed after Wiley and McLaren [1], the first field-free ion drift region with an ion deflector and einzel lens, the ion deceleration and reflection regions, the second drift region for the reflected ions, and a microchannel plate detector (HAMAMATSU Photonics/F1552-23S). A set of ion optics which includes acceleration plates, einzel lens and deflectors is mounted in the second chamber. The pressure in the second chamber is typically *ca.* 10^{-7} Torr. The reflectron chamber is 800 mm long, and evacuated with an oil diffusion pump (Edwards/Diffstak 100) backed by an oil rotary pump (ULVAC/D-330D). The background pressure is typically 2×10^{-8} Torr. The reflector, placed at the end of the chamber, consists of a deceleration and reflection plates as well as 17 electrodes to produce a homogeneous reflection field. The reflector compensates the flight time difference caused by the initial kinetic energy distribution of the ions as follows. The ions which have higher translational energies penetrate into the deeper region of the reflector, while the lower-energy ions are reflected back at the shallow region of it. As a result, the ions which have the lower and higher energies travel along the shorter and longer paths, respectively. Thus the ions are focused on the detector and their TOF difference is minimized. The total flight length of the ion from the extraction grid to the ion detector is *ca.* 2 m. The principles of Wiley-McLaren type TOF mass spectrometer and reflectron as well as details of experimental conditions are described in Appendices 1-3 of

this chapter in detail. The ion signals are accumulated on the digital storage oscilloscope (LeCroy/9450) after amplification by a wide band preamplifier (NF Electronic Instruments/BX-31). The mass resolution of this system is *ca.* $\Delta M/M$=800.

2. Photoelectron spectrometer

The cross sectional view of the photoelectron spectrometer is shown in Figure II-5. The system consists of three-stage differentially evacuated chambers which correspond to a laser-vaporization cluster source, a Wiley-McLaren type TOF mass spectrometer, and a magnetic-bottle type TOF electron energy analyzer, respectively. The source chamber is evacuated by an oil diffusion pump (ULVAC/ULK-10A, 3000 *l*/s) backed by a evacuation unit (ULVAC/YM-100C) consisting of a mechanical booster and an oil rotary pumps. The background pressure is typically 1×10^{-7} Torr. A pulsed nozzle (R. M. Jordan/PSV, orifice diameter ≈0.5 mm) is placed on the ion-beam axis, and driven at a constant pulse duration of 60μs. A conical throat made of an aluminum block is attached in front of the orifice of pulsed nozzle. Sample metal rod (5 mm in diameter) which is designed to rotate and translate by a stepping motor is located at the throat as shown in Figure II-6. The vaporizing laser pulse (second harmonic of a Nd:YAG laser, Continuum/YG-661, typically 800 μJ/pulse) is focused by a convex lens (f=500 mm) and irradiated on the metal rod through a 1 mm-diameter hole. Negative ions directly produced in the source are extracted by pulsed electric fields (Velonex/350, 800V amplitude, 2 μs duration) and introduced into the second chamber through a skimmer. A set of ion optics (two sets of deflector and two sets of einzel lens) is mounted in

the second chamber evacuated by an oil diffusion pump (Edwards/Diffstak 160MN) backed by an oil rotary pump (Edwards/E2M-18). The background pressure is kept below *ca.* 5×10^{-8} Torr. The collimated ions are introduced into the detachment chamber evacuated by a turbo molecular pump (Seiko Seiki/STP 300) backed by an oil rotary pump (Edwards/E2M-12). The background pressure is typically 2×10^{-9} Torr. The ions of a given mass are isolated by a mass gate (voltages are supplied by HAMAMATSU/C3350 and KIKUSUI/PMA350-0.2A and switched by DEI/GRX-1.5KE) after flying 0.9 m. Then the ions are decelerated by a potential switching method using a home-made pulse generator. Mass spectra are recorded by detecting the ion signals as a function of flight time. As an ion detector, dual microchannel plates (HAMAMATSU/F1551-23S) is used. The signal of the microchannel plate is digitized in the storage oscilloscope (LeCroy/9350). For the photoelectron kinetic energy measurements, third or fourth harmonic of a Nd:YAG laser (Quanta-Ray/DCR-2A or GCR-12, typically 2mJ/pulse) is used as a detachment laser. Decelerated ions are irradiated with the detachment laser at right angles in the center of the third chamber. The detached electrons are collected and energy-analyzed by the magnetic bottle-type photoelectron spectrometer. This spectrometer has an advantage that all electrons emitted from the ions over nearly 4π sr are collected by a magnetic mirror effect combined with an electron paralleliser effect. In Figure II-7, the principle of magnetic bottle is illustrated. The magnetic bottle contains the divergent magnetic field, photoelectrons are detached in a region which is downhill from the peak of the strong magnetic field. The principle of magnetic bottle photoelectron spectrometer are described in Appendix 4 of this chapter. A stronger and weaker magnetic fields are produced with a Sm-Co magnet (0.08 T) and a

solenoid coil (0.2 mT). The current of the solenoid coil is provided by a regulated DC power supply (TAKASAGO/GP 050-2). The photoelectrons are detected by dual microchannel plates (HAMAMATSU/F1552-23S) after flying *ca.* 1.2 m in the electron TOF tube, which is magnetically shielded by μ-metal plates to avoid the disturbance of terrestrial magnetism and other magnetic field. The electron signals are accumulated in the digital storage oscilloscope (LeCroy/7200A) as a function of flight time and then transmitted to the microcomputer to convert into the photoelectron spectra. The calibration of photoelectron energy is carried out by using the detachment energy of the atomic anions (*i.e.* Li^- and Na^-). The resolution of the photoelectron spectrum is about 120 meV for the 1.23 eV peak of the Cu^- ion with a detachment laser at 355 nm (the kinetic energy of the photoelectron; 2.26 eV).

3. Appendices

1. Principle of Wiley-McLaren type TOF mass spectrometer

The principle of the TOF mass spectrometer, which was firstly reported in 1948 [2], is quite simple. The bunch of ions entering into or produced at the source region is accelerated with a single, constant electric field, E, in the source region with s in length. The ions with a constant translational energy are introduced to a field free region with l in length. A TOF, t, of an ion with mass M and charge e from the source region to the detector is given by

$$t = \sqrt{M} \cdot \left(\sqrt{\frac{2s}{eE}} + \frac{l}{\sqrt{2eE}} \right). \qquad \text{(II-1)}$$

The mass, M, is proportional to t^2 and thus can be determined from the observed TOF according to eq.II-1. The resolution, R, of the mass spectrometer is defined by the maximum mass number that can be resolved with an unit mass. By using eq. II-1, R can be expressed as

$$R = \frac{t_R}{2\Delta t} \qquad \text{(II-2)}$$

where t_R is the TOF of the ion with mass R and Δt is the difference between the TOF of mass R and R+1.

Although the single-acceleration-field mass spectrometer firstly developed has several advantages, for example, (1) obtainable mass range is unlimited, and (2) the total mass spectrum is obtained with high efficiency in short acquisition times, it has one inevitable defect of the poor mass resolution. This problem is caused by the two factors; the spatial and the velocity distributions of ions in the source region. It has turned out that the former factor in this problem is resolved by using a Wiley-McLaren type TOF mass spectrometer with double-electric fields [1]. In the double acceleration system as illustrated in Figure II-3, the ions are accelerated by two independent electric fields, E_s and E_d, in the regions given s and d in length, respectively. The total TOF, t, is the sum of the TOFs, t_s, t_d and t_l, of each region, s, d, and l, respectively, *i.e.*,

$$t = t_s + t_d + t_l. \qquad \text{(II-3)}$$

The TOF of each region is

$$t_s = \sqrt{\frac{2M}{e}} \cdot \sqrt{\frac{s}{E_s}}, \tag{II-4}$$

$$t_d = \sqrt{\frac{2M}{e}} \cdot \frac{\left(\sqrt{U} - \sqrt{sE_s}\right)}{E_d}, \tag{II-5}$$

and

$$t_l = \sqrt{2M} \cdot \frac{l}{2\sqrt{U}}, \tag{II-6}$$

where U is the total acceleration voltage expressed as

$$U = sE_s + dE_d, \tag{II-7}$$

under the approximation that the initial velocity of the ions is equal to zero. The condition of space focusing, which is defined by the condition that the ions with spatial distribution in the source reach the detector with minimum time distribution in the first order, is obtained by

$$\left(\frac{dt}{ds}\right)_{s=s_0} = 0, \tag{II-8}$$

where s_0 is the average first acceleration length of ions, which is typically equal to the half of the length between the first and second acceleration plates (see Figure II-3). From eqs. II-3-8, we obtain the relation,

$$l = 2s_0 k_0^{3/2}\left[1 - \frac{d}{s_0\left(k_0 + \sqrt{k_0}\right)}\right], \qquad \text{(II-9)}$$

where

$$k_0 = (s_0E_s + dE_d)/s_0E_s. \qquad \text{(II-10)}$$

In the design for the double-acceleration TOF mass spectrometer, the parameters of the mass spectrometer are given by eq. II-9; the parameters are the strengths of the acceleration fields, E_s and E_d, the distance between the first and second acceleration plates, $2s_0$ and d, and the total flight length of ions, l.

2. Principle of reflectron type TOF mass spectrometer

The second factor of the problem that limits the resolution in the TOF mass spectrometer, *i.e.*, the velocity distribution of ions, has been overcome by using the reflectron TOF mass spectrometer [3-5]. The mass resolution is highly improved by using an ion reflector which is able to compensate an initial ion-velocity distribution originated in a cluster source, and this mass spectrometer has turned out to be useful for the cluster research.

Schematic diagram of the reflectron TOF mass spectrometer is shown in Figure II-3. In this mass spectrometer, an ion reflector is placed between the Wiley-McLaren type mass spectrometer and the detector. Two electric fields, the deceleration and reflection fields, are applied in the ion reflector. The potential differences and interelectrode distances are U_T and d_T for the electric field of deceleration, and U_K and

d_K for the field of reflection, respectively. The reflection grids consist of 17 guiding plates, which are placed at regular intervals and interconnected by resistors in order to make a uniform electric field.

The trajectories of ions in the ion reflector are schematically shown in Figure II-4. The principle of the energy focusing in the reflectron TOF mass spectrometer, defined by the condition that the ions with energy distribution reach the detector with minimum time spread up to the second order, can be visualized in the extreme case as shown in the figure. Consider the pair of ions with the same mass, M, and the same initial kinetic energy, $e\delta U$, but with the opposite direction of velocity; one has a velocity with a direction to the drift region and the other with an opposite direction. In the first field free region, l, the ions have different kinetic energies, $e(U_0+\delta U)$ and $e(U_0-\delta U)$, respectively. The difference in arrival times to a detector is decreased by optimizing the condition of electric fields, so as to the one ion with $e(U_0+\delta U)$ turns back at a deeper point in the ion reflector, and so as to the another ion with $e(U_0-\delta U)$ turns back at a shallower point.

The time-of-flight of the ions after acceleration, t, in Figure II-3 is written by the sum of the TOFs of the first and second drift region, t_L, of the deceleration region, t_T, and of the reflection region t_K, *i.e.*,

$$t = t_L + t_T + t_K. \qquad \text{(II-11)}$$

Consider the condition that the energy of the accelerated ions, eU, has a distribution with an average energy of eU_0. The TOFs of the three regions are written as

$$t_{\mathrm{L}} = \frac{L}{\sqrt{\frac{2eU_0}{M}}} \cdot \frac{1}{\sqrt{k}}, \tag{II-12}$$

$$t_{\mathrm{T}} = \frac{4d_{\mathrm{T}}}{\sqrt{\frac{2eU_0}{M}}} \cdot \frac{U_0}{U_{\mathrm{T}}} \cdot \left(\sqrt{k} - \sqrt{k - \frac{U_{\mathrm{T}}}{U_0}} \right), \tag{II-13}$$

and

$$t_{\mathrm{K}} = \frac{4d_{\mathrm{K}}}{\sqrt{\frac{2eU_0}{M}}} \cdot \frac{U_0}{U_{\mathrm{K}}} \cdot \left(\sqrt{k - \frac{U_{\mathrm{T}}}{U_0}} \right), \tag{II-14}$$

where k is a factor defined by $k=U/U_0$, and L is total length of the two field free regions, *i.e.*, $L = l+l_2$. The energy focusing condition is expressed as

$$\left(\frac{dt}{dU} \right)_{U=U_0} = 0, \tag{II-15}$$

and

$$\left(\frac{d^2t}{dU^2} \right)_{U=U_0} = 0. \tag{II-16}$$

From eqs. II-11-16 we obtain

$$\frac{L}{4d_{\mathrm{K}}} \cdot \frac{U_{\mathrm{K}}}{U_0} \approx \sqrt{3}, \tag{II-17}$$

and

$$\frac{U_T}{U_0} \approx \frac{2}{3}. \qquad \text{(II-18)}$$

3. Experimental parameters of the reflectron TOF mass spectrometer used in the present study

The geometrical parameters of our homemade reflectron TOF mass spectrometer are as follows:

$s_0 = 10$ mm,
$d = 10$ mm,
$L = l + l_2 = 2000$ mm,
$l = 1400$ mm; $l_2 = 600$ mm,
$d_T = 12$ mm; $d_K = 100$ mm.

In the typical experimental condition for the observation of the mass spectrum of the ions initially produced in a cluster source, the source parameters after optimization are as follows;

E_s =200 V/cm,
$E_d = 2900$ V/cm,

and

$U_0 = 3100$ V.

Under this condition, the plane of the space focusing is estimated to be 116 cm from the end of acceleration region, by using eq. II-9. In the present apparatus, the focal point under a thin condition lies just in front

of the ion reflector. The electric potentials of the ion reflector can also be determined from eqs. II-17 and II-18 as

U_T(calc) =1074 V

and

U_K(calc) =3141 V.

These parameters are optimized experimentally as

U_T(exp)=960 V

and

U_K(exp)=3280 V.

Under these conditions, the mass resolution, R, of *ca.* 800 is achieved.

4. Principle of magnetic-bottle type photoelectron spectrometer

Magnetic field paralleliser for electron spectrometer

The essence of the parallelisation technique is illustrated in Figure II-7. An electron initially emitted at an angle θ_i to the z direction, and with an energy E and velocity v, undergoes helical motion in the magnetic field $\boldsymbol{B}_i$. The angular frequency of the motion is

$$\omega_i = e\boldsymbol{B}_i/m \qquad \text{(II-19)}$$

where e and m are the charge and mass of the electron. The radius of the orbit (*i.e.* the cyclotron radius) is

$$r_i = v \sin \theta_i/\omega_i \qquad \text{(II-20)}$$

and the angular momentum of the circular motion is

$$l_i = \frac{m^2 v^2 \sin^2 \theta_i}{e\boldsymbol{B}_i} \qquad \text{(II-21)}$$

If the variation of the magnetic field with z is adiabatic, by which we mean that if the field experienced by an electron changes negligibly in the course of one revolution of the helical motion, then the angular momentum is a conserved quantity. This implies that the angle θ_f of the helical motion on the region of the low field ($\boldsymbol{B}_f$) is given by

$$\frac{\sin\theta_f}{\sin\theta_i} = \sqrt{\frac{\boldsymbol{B}_f}{\boldsymbol{B}_i}} \qquad \text{(II-22)}$$

The transverse component of the velocity is therefore reduced. Since the total velocity is unchanged the longitudinal component increases from $v\cos\theta_i$ to

$$v_{zf} = v\sqrt{1-\left(\frac{\boldsymbol{B}_f}{\boldsymbol{B}_i}\right)\sin^2\theta_i}\ . \qquad \text{(II-23)}$$

The electron trajectories are therefore parallelised in the type of magnetic field shown in the Figure II-7.

In the photoelectron spectrometer used in this work, the electrons start in a field strength that is typically ≈0.08 T, are parallelised in a

distance of a few mm, and then drift in a uniform field of typically 0.2 mT to a detector placed 1.2 m from the electron source. Electrons emitted with initial angles θ_i to the z direction in the range from 0° to nearly 90° travel in the drift tube with angles θ_f in the range from 0° to

$$\theta_{f,max} = \sin^{-1}\sqrt{\frac{\boldsymbol{B}_f}{\boldsymbol{B}_i}} = 2.9 \text{ (degree)} \qquad \text{(II-24)}$$

The time of flight for the first 30 mm depends greatly on the angle θ_f, but the time of flight in the drift tube itself is

$$T_{drift} = \frac{l_{drift}}{v_{zf}} \approx \frac{l_{drift}}{v}\left(1+\frac{\boldsymbol{B}_f \sin^2\theta_i}{2\boldsymbol{B}_i}\right) \qquad \text{(II-25)}$$

which is almost independent of θ_i.

There are several factors to limit the resolution of the spectrometer, the most crucial limitation stems from the finite velocity of the negatively charged ions, v_I. Since velocity of the detached electron in the cluster center of mass, v_e, will range between v_e+v_I and v_e-v_I in the laboratory frame. One can thus assume a velocity spread of $2v_I$ for the electron. The resultant energy spread can be expressed as

$$dE_e = m_e v_e dv_e = \sqrt{2m_e E_e}\cdot 2\sqrt{\frac{2E_I}{m_I}} = 4\sqrt{\frac{m_e}{m_I}\cdot E_e E_I} \qquad \text{(II-26)}$$

where E_e and E_I denote the kinetic energies of the electron in the center of mass and of the clusters, respectively, while m_e and m_I denote the masses. For this reason, I decelerate the ions prior to the detachment. Because of a rather wide energy distribution of the ions (which is intrinsic to the laser vaporization cluster source) the typical ion velocity

after deceleration is several tens of eV. On deceleration to lower kinetic energy the electron signal decreases drastically in magnitude.

I shall now consider the effects which are intrinsic to the magnetic design of the spectrometer. The degree of parallelisation of the electrons on their entry to the drift tube is given by eq. II-24. The intrinsic limit on the resolution in the magnetic design can be then approximated as

$$\frac{dE_e}{E_e} = \frac{\boldsymbol{B}_f}{\boldsymbol{B}_i} \qquad \text{(II-27)}$$

There is a finite time upon which the electrons are redirected along the magnetic field line of the drift tube. It is zero for the electrons which are directed along the detection axis and are the longest for the electrons which are directed away from the flight tube and are reflected back by a magnetic field *via* a magnetic mirror mechanism. Under the adiabatic approximation, the reflection or redirection time is proportional to $\sqrt{E_e}$ and depends on the initial direction of the electrons and on the distribution of the magnetic fields. The time spread of isotropically detached electrons in a given magnetic field is proportional to $\sqrt{E_e}$. Thus, using the photons of lower energies is needed to reduce the E_e in order to get higher resolution.

Furthermore, various parameters affect the resolution of the spectrometer, such as the length of the drift region, the duration of laser pulse, the details of the magnetic fields, and the size of the laser focus as well. The influence of these parameters are supposed not to be crucial in the spectrometer used in the present work.

Magnetic mirror effect

The principle of magnetic mirror effect is described below. If we assume the magnetic field which has cylindrical symmetry around the z axis, we obtain the relation

$$\frac{\partial}{\partial r}(rB_r) + r\frac{\partial B_z}{\partial z} = 0 \qquad \text{(II-28)}$$

from $\nabla \cdot \boldsymbol{B} = 0$ in cylindrical coordinates. Thus we obtain

$$B_r = -\frac{1}{2} r \left(\frac{\partial B_z}{\partial z} \right)_{r=0}. \qquad \text{(II-29)}$$

The vector potential which expresses this magnetic field $\boldsymbol{A}$ is written as

$$\boldsymbol{A} = (0, \boldsymbol{A}_\theta, 0). \qquad \text{(II-30)}$$

The Lagrangian L about the charged particle moving in the magnetic field is given by

$$L = \frac{1}{2} m(v_r^2 + v_\theta^2 + v_z^2) + v_\theta A_\theta \qquad \text{(II-31)}$$

The solution on z is obtained as

$$\frac{d}{dt}(mv_z) = qv_\theta \frac{\partial A_\theta}{\partial z}. \qquad \text{(II-32)}$$

When we rewrite the vector potential of eq.II-32 with eq.II-29, and using relationships $r = r_L = v/\omega$ and $v_\theta = r_L\omega$, we obtain

$$\frac{d}{dt}(mv_z) = -\mu\frac{\partial B_z}{\partial z}. \qquad \text{(II-33)}$$

Eq.II-33 means that the particle experiences the force directed to lower magnetic field. We can regard the z component of the magnetic field as the potential energy.

If we assume that the electrons at detachment point access to mirror point with Larmor precession, we can obtain the relationship from the adiabatic invariance of μ,

$$\mu = \frac{mv_{\perp 0}^2}{2B_0} = \frac{mv_{\perp M}^2}{2B_M}, \qquad \text{(II-34)}$$

thus,

$$\frac{v_{\perp 0}^2}{v_{\perp M}^2} = \frac{B_0}{B_M} \qquad \text{(II-35)}$$

where, $\boldsymbol{B}_0$ and $\boldsymbol{B}_{\mathrm{M}}$ are the magnetic field strengths at the detachment region of the negative ion and turning point (mirror point) of electron, respectively. Since the kinetic energies of electrons are conserved during traveling with the Lorentz force, sums of squares of each component of motion are same at detachment point and mirror point. Thus,

$$v^2 = v_{//}^{\ 2} + v_{\perp}^{\ 2} = v_{//\mathrm{M}}^{\ 2} + v_{\perp\mathrm{M}}^{\ 2} = v_{\perp\mathrm{M}}^{\ 2}. \qquad \text{(II-36)}$$

From eq.II-35 and 36, we obtain

$$\frac{B_0}{B_M} = \frac{v_{\perp 0}^2}{v^2} = \sin^2\theta. \qquad \text{(II-37)}$$

We can conclude that the electrons which satisfy $v_{\perp 0}/v > \sqrt{B_0 / B_M}$ are reflected by the magnetic bottle, and the other electrons escape from them. The realm that satisfies $v_{\perp 0}/v < \sqrt{B_0 / B_M}$ is called "loss cone" and the ratio $\boldsymbol{B}_0/\boldsymbol{B}_M$ is called mirror ratio.

In practice, the strength of magnetic field $\boldsymbol{B}_i$ and $\boldsymbol{B}_f$ is optimized with measuring the resolution of the spectrometer. The optimal field is obtained as $\boldsymbol{B}_i$ = 0.08 T and $\boldsymbol{B}_f$ = 0.2 mT. Under these conditions, the resolution of the photoelectron spectrum is 120 meV for the 1.23 eV peak of the Cu^- ion with a detachment laser at 355 nm (the kinetic energy of the photoelectron; 2.26 eV).

References for Chapter II

[1] Wiley, W. C.; McLaren, I. H. *Rev. Sci. Instrum.* **1955**, *26*, 1150.
[2] Cameron, A. E.; Eggers, Jr., D. F. *Rev. Sci. Instrum.* **1948**, *19*, 605.
[3] Kataraef, V. I.; Mamyrin, B. A.; Shmikk, D. V. *Sov. Phys. -Tech. Phys.* **1972**, *16*, 1177.
[4] Mamyrin, B. A.; Kataraev, V. I.; Shmikk, D. V.; Zagulin, V. A. *Sov. Phys. JETP* **1973**, *37*, 45.
[5] Shinohara, H. *Shitsuryo bunseki* **1990**, *38*, 43.
[6] Kruit, P.; Read, F. H. *J. Phys. E: Sci. Instrum.* **1983**, *16*, 313.
[7] Cheshnovsky, O.; Yang, S. H.; Pettiette, C. L.; Craycraft, M. J.; Smally, R. E. *Rev. Sci. Instrum.* **1987**, *58*, 2131.

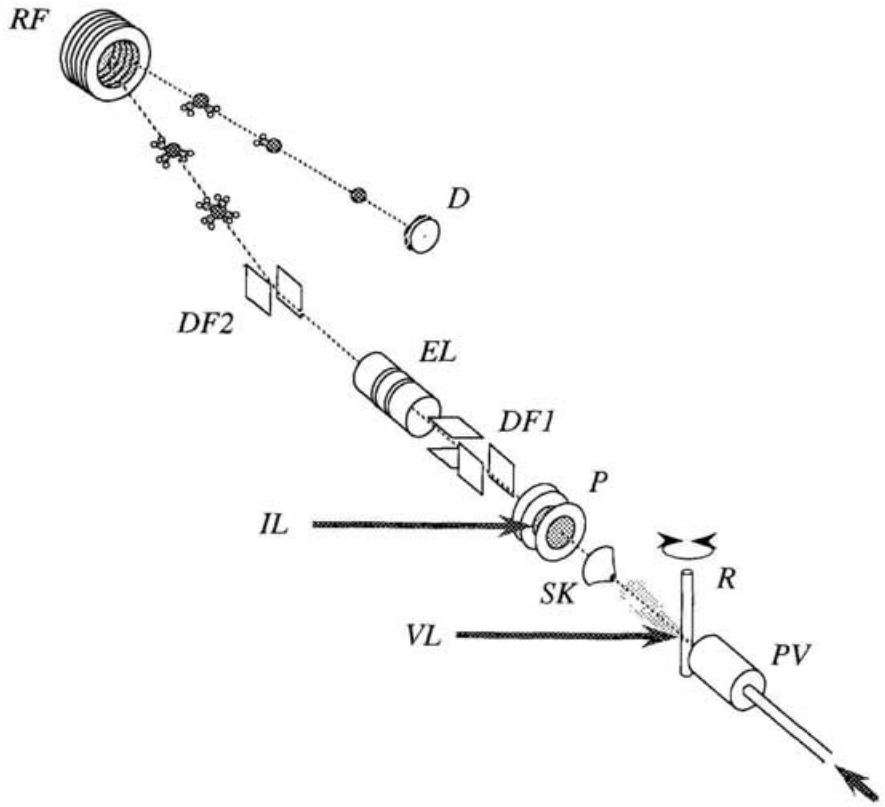

Figure II-1. Schematic representation of reflectron time-of-flight mass spectrometer. *PV*; pulsed valve, *R*; sample rod, *VL*; vaporization laser irradiation, *SK*; skimmer, *P*; acceleration plates, *IL*; ionization laser irradiation, *DF1*, *DF2*; deflectors, *EL*; einzel lens, *RF*; reflector, *D*; microchannel plate

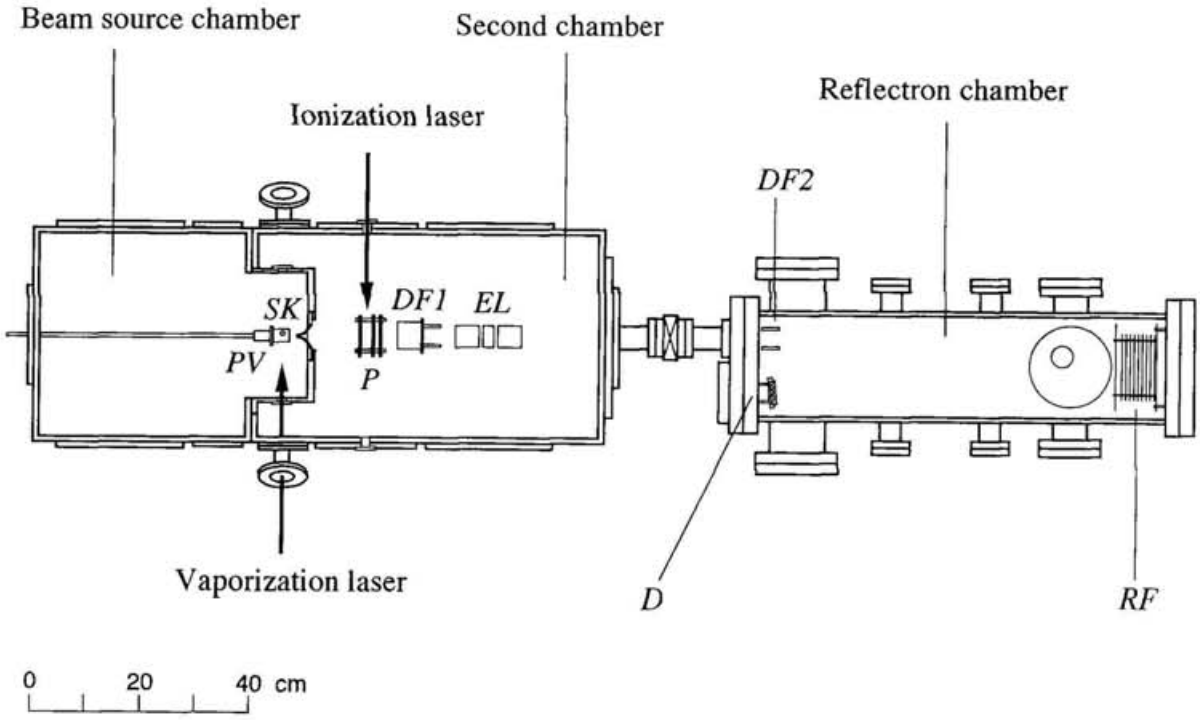

Figure II-2. Schematic top view of the reflectron type time-of-flight mass spectrometer used for photoionization spectroscopy. *PV*; pulsed valve, *SK*; skimmer, *P*; acceleration plates, *DF1,DF2*; deflectors, *EL*; einzel lens, *RF*; ion reflector, *D*;detector.

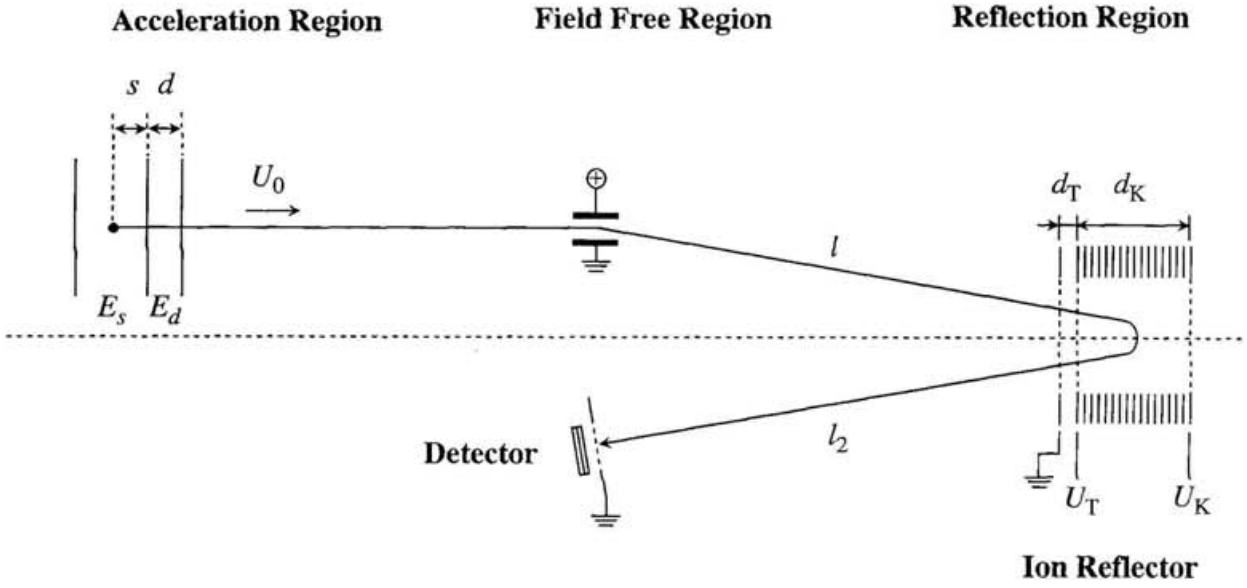

Figure II-3. Basic geometry and definition of the parameters of the reflectron type time-of-flight mass spectrometer. Values for the parameters in this figure are noted in the text.

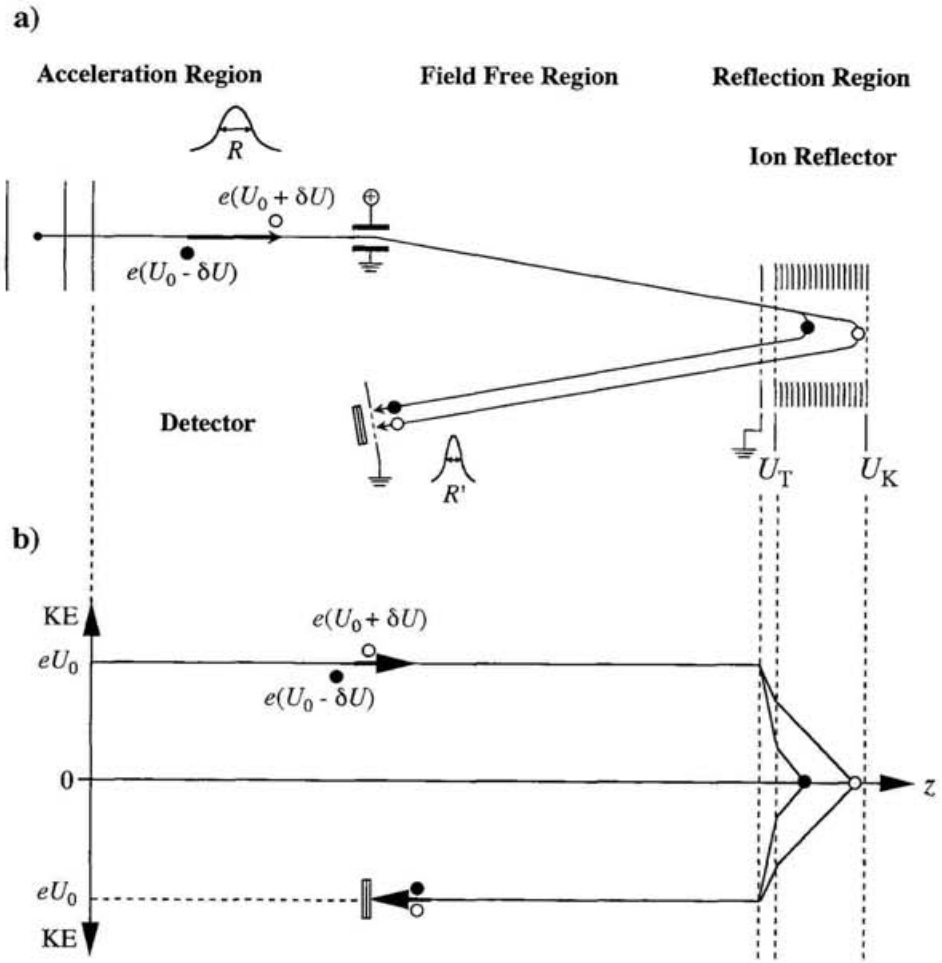

Figure II-4. (a) Schematic drawing of the different trajectories of ions with the kinetic energies, $e(U_0+\delta U)$ and $e(U_0-\delta U)$, respectively. (b) The electric field potentials that the ions experience.

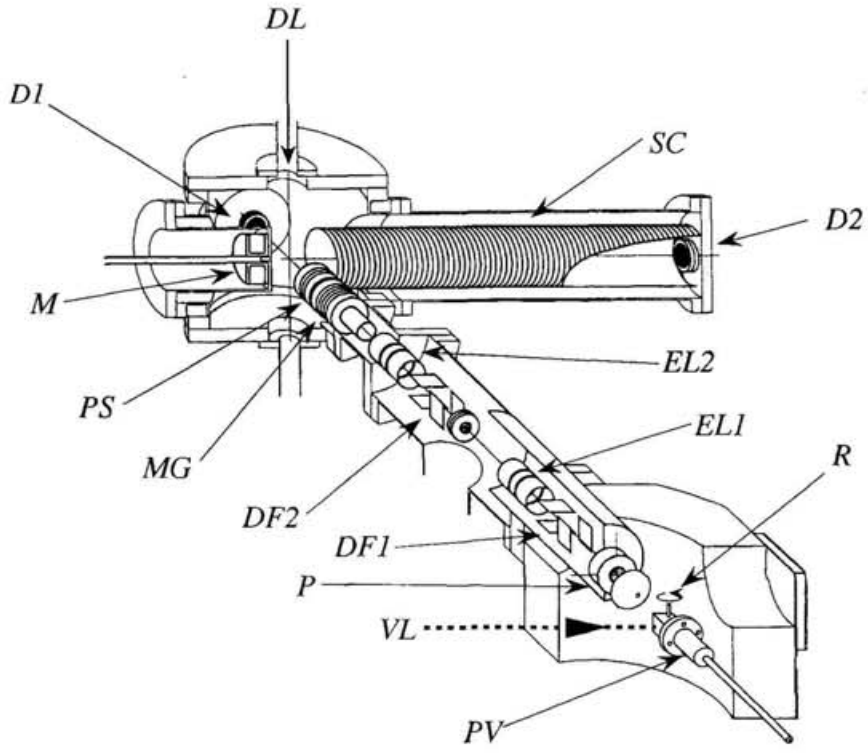

Figure II-5. Cross sectional view of the magnetic bottle type photoelectron spectrometer. *PV*; pulsed valve, *R*; sample rod, *VL*; vaporization laser irradiation, *P*; acceleration plates, *DF1*, *DF2*; deflectors, *EL1*, *EL2*; einzel lenses, *MG*; mass gate, *PS*; potential switch, *M*; permanent magnet, *SC;* solenoid coil, *DL*; detachment laser irradiation, *D1*; microchannel plate (for ion detection), *D2*; microchannel plate (for electron detection)

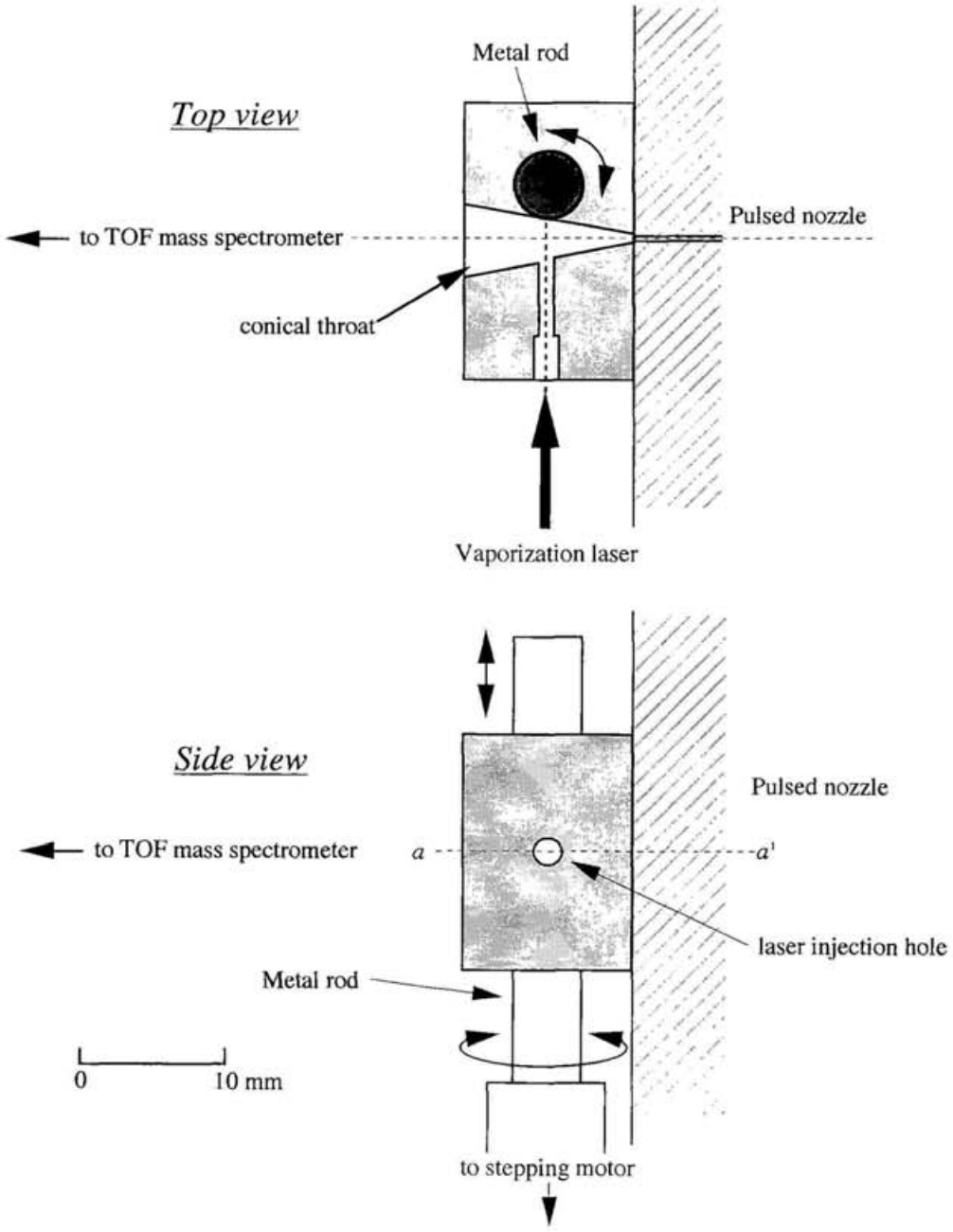

Figure II-6. Geometry of the cluster beam source used in photoelectron spectroscopy. (*upper*) Cross sectional top view at *a*-*a*' of the bottom figure. (*bottom*) Side view.

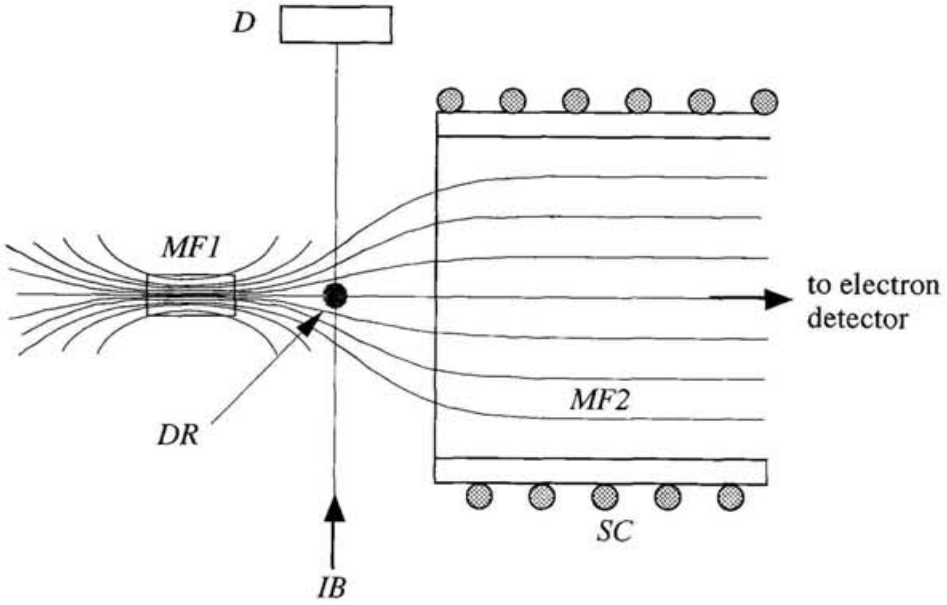

Figure II-7. Illustration of the magnetic bottle-type photoelectron spectrometer. *IB*; negative ion beam, *DR*; detachment region (detachment laser irradiation), *MF1*; stronger magnetic field, *MF2*; weaker magnetic field, *SC*; solenoid coil, *D*; ion detector

Chapter III
Microscopic solvation process of alkali atoms in finite clusters; photoelectron and photoionization studies

1. Introduction

Electrons in polar solvent have been the subject of intensive studies for the last decades [1]. Recent advances in ultrafast laser spectroscopy permit to obtain unique information on the dynamical aspects of the solvated electron, especially on the early stage of solvated-electron formation in solution. These studies have revealed various steps in the relaxation process of solvated electron [2,3]. In spite of these efforts, the microscopic structure and dynamics of solvated electron remain unresolved [4]. One of the most intriguing and difficult issues may be the many body interaction between a diffuse electron and solvent molecules. It seems to be difficult to fully understand the solvation dynamics of electron in polar solvent without detailed knowledge on the nature of the diffuse electron. On the other hand, these issues are significantly simplified in clusters, in which the fundamental interactions in solution may be retained. The cluster study enables us a direct comparison between the experimental and theoretical results and, as a result, will provide information on the intrinsic nature of solvated electron.

Several efforts have been made to explore the microscopic aspect of solvated electron in clusters. Negatively charged water and ammonia clusters, $(H_2O)_n^-$ and $(NH_3)_n^-$, have been prepared *via* capture of low-energy electrons by

solvent clusters [5,6]. The vertical detachment energies have been obtained for $(H_2O)_n^-$ and $(NH_3)_n^-$ with n up to ≈70 and 1100, respectively [7,8]. and the excess electron states have also been examined using quantum pass integral molecular dynamics simulations [9,10]. Moreover, the electronic spectra of $(H_2O)_n^-$ have been examined by the photodestruction spectroscopy [11]. Besides these studies, the polar-solvent clusters containing neutral alkali atoms have been studied. These clusters are the prototype of a dilute alkali metal solution, in which solvated electron has been investigated extensively, and may serve as a good model for linking the macroscopic with microscopic properties of alkali metal-solvent systems. In these clusters, the valence electron of alkali metal atom is expected to be transferred to a solvent cluster with sufficiently large n, and the ground state may have an ion-pair character as in the case of bulk fluids [1]. In order to probe the above transition, Hertel's and Fuke's groups have investigated the photoionization processes of the clusters consisting of alkali metal atoms such as Na [12] and Cs [13] with ammonia and water molecules. The ionization potentials (IPs) of both $Na(H_2O)_n$ and $Cs(H_2O)_n$ have found to rapidly converge to the photoelectric threshold of ice at n=4 (3.2 eV), while the IPs of metal-ammonia clusters decrease monotonously for n as large as 40; its limiting values again agree with the bulk photoelectric threshold of liquid ammonia at *ca.* 1.4 eV. These features in IPs have been discussed in terms of the stabilization of an ion-pair state correlating with the solvated electron state in bulk solution. Several theoretical groups have also made efforts to correlate the IP behaviors with the solvation state of alkali atoms [14-20]. However the experimental data are limited to the IP measurements, the microscopic solvation process of alkali-metal atoms in clusters has not yet been fully understood.

In this study, I investigate the photoelectron spectra of $Li^-(NH_3)_n$ (n≤16). The results clearly indicate the drastic change in the electronic structure of the 2^2P-type state as well as the higher excited state such as the 3^2S even for n<10,

suggesting the spontaneous ionization of the Li atom in clusters. I also examine the photoelectron spectra of $Na^-(NH_3)_n$ ($n \leq 12$) and $Na^-(H_2O)_n$ ($n \leq 7$). The spectra of ammoniated Na^- show the similar spectral change to those for Li^-, but the hydrated Na^- exhibits no such change; for the latter clusters, both 3^2S- and 3^2P-type bands are shifted to the higher vertical detachment energy with maintaining similar energy separation. In addition to these studies, I also examine the IPs of $Li(NH_3)_n$ ($n \leq 28$) and $Li(H_2O)_n$ ($n \leq 46$) to obtain further examples on the photoionization process of solvated alkali atoms. On the basis of these experimental results as well as those of the *ab initio* calculations, I will discuss the solvation state of alkali atoms in relation to the early stage of solvated-electron formation in finite clusters.

2. Experimental

Details of the experimental apparatus for the photoionization and photoelectron spectroscopies used in this work have been described in Chapter II. The photoionization spectroscopy is carried out by using the reflectron-type time-of-flight mass spectrometer. The Li and Na sample are purchased from Rare Metallic Co. Ltd. (99.9 % purity) and re-formed prior to use to fit with the nozzle beam source. For ammonia-containing clusters, a mixture of ammonia and Ar gases (40% ammonia) is used as a carrier gas. The ammonia (NH_3, minimum purity of 99.99 %, Nippon Sanso) is used without further purification. For water containing clusters, ion exchanged and then ultrafiltrated water is used. Clusters are photoionized with a frequency-tunable dye laser (Quanta-Ray/GCR-250/PDL-3 or Lambda Physik/LPX205i/FL2002) at the acceleration region of TOF mass spectrometer. The pulse energy is attenuated to several tens of μJ/pulse to avoid the multiphoton process. Photoionization mass spectra are obtained by

scanning the photon energy with an interval of *ca.* 0.01 eV in the region of 2.23-4.56 eV (556-272 nm). The ionization thresholds are determined within ±0.03 eV by analyzing the mass spectra. The error caused by field ionization is estimated to be about 0.01 eV in the present experimental conditions.

The photoelectron spectroscopy is carried out by means of the magnetic-bottle type photoelectron spectrometer described in Chapter II. The metal samples are set similar to the photoionization experiment described above. Ar gas of 2 atm mixed with water vapor or pure ammonia gas is used as a carrier gas.

3. Results

Ionization potentials of $Li(NH_3)_n$ and $Li(H_2O)_n$

The $Li(NH_3)_n$ clusters are produced up to n=50 by laser vaporization technique coupled with a supersonic expansion. Figure III-1 shows the mass spectrum of these cluster ions produced by the irradiation of an ArF excimer laser at 193 nm exhibits a strong magic behavior at n=4. I also detect the Li_2-ammonia clusters with a magic behavior at n=8. The ionization potentials (IPs) of $Li(NH_3)_n$ ($5 \le n \le 28$) determined by the photoionization threshold measurements decrease almost linearly with $(n+1)^{-1/3}$ and give the limiting value at $(n+1)^{-1/3}=0$ ($n \to \infty$) as 1.47 eV as shown in Figure III-2. This value agrees with the limiting values for $Cs(NH_3)_n$ and $Na(NH_3)_n$ and also with the photoelectric threshold of liquid ammonia (1.45 eV [8]).

Figure III-3a shows a typical mass spectrum of the clusters containing the Li atom and water molecules photoionized by 193 nm laser irradiation. $Li^+(H_2O)_n$ ions are detected for $n \le 50$ with a strong magic behavior at n=4; this magic behavior is observed even at the ionization wavelengths longer than 308

nm. The weak signals from clusters containing two and three Li atoms are also detected, but these clusters appear as the hydrogen-eliminated forms such as $Li_2^+OH(H_2O)_n$ and $Li_3^+O(H_2O)_n$, respectively. I cannot detect an aggregate such as $Li^+OH(H_2O)_n$, though the abundance of Li atoms is much higher than that of Li_2 in the present cluster source. In the literature, similar aggregates such as $Na_2OH^+(H_2O)_n$ have also been detected in sodium-water mixtures, while $NaOH^+(H_2O)_n$ have not been detected [24]. Recently, Buck and coworkers have investigated the reaction of Na_n with water clusters at the thermal collision energy using a crossed molecular beam apparatus [25]. They have found only $Na(H_2O)_n$ and no reaction products such as $NaOH^+(H_2O)_m$ and $Na_2OH^+(H_2O)_m$. The latter results suggest that the clusters are produced by much higher-energy collision in the present experiment; since I use the laser vaporization method to produce the Li atoms and its clusters, they may have a wide-spread kinetic-energy distribution [26].

In contrast to the case of the metal-ammonia clusters, the mass spectra of $Li(H_2O)_n$ show a drastic drop of the ion intensity in the ionization wavelength range from 390 to 400 nm as shown in Figures III-3b-d; the ion signals for $5 \leq n \leq 46$ disappear simultaneously at 397±2 nm as in the case of $Na(H_2O)_n$ and $Cs(H_2O)_n$ reported previously [12,13]. The IPs for $n \geq 5$ are estimated from the ionization thresholds to be 3.12±0.03 eV. I cannot determine the IPs for n=8 and 9 because of the interference of co-existing background ion signals. In Figure III-4, the IPs of $Li(H_2O)_n$ are plotted as a function of $(n+1)^{-1/3}$. For comparison, I also plot the results for $Cs(H_2O)_n$ being reported previously [13]. The IPs of these clusters decrease almost linearly for $n \leq 4$, and become constant at 3.12±0.03 and 3.10±0.03 eV for the Li- and Cs-water clusters with $n \geq 5$, respectively. These values are in agreement with the results for $Na(H_2O)_n$ (3.17 eV) [12] and the limiting value of the vertical detachment energy (VDE) for $(H_2O)_n^-$ (3.3 eV), and also the estimated photoemission threshold of hydrated electron (*ca.* 3.2 eV [8]).

Photoelectron spectra of $Li^-(NH_3)_n$ and $Na^-(NH_3)_n$

Figure III-5 shows the TOF mass spectrum of the negative ions of the lithium-ammonia clusters. The spectrum consists of three series of cluster ions such as Li_n^- ($n \leq 4$), $Li^-(NH_3)_n$ ($n \leq 16$), and $Li_2NH_2^-(NH_3)_n$ ($n \leq 7$). The abundance of $Li_2NH_2^-(NH_3)_n$ is estimated to be less than 20 % of that for $Li^-(NH_3)_n$. The intensities of $Li^-(NH_3)_n$ decrease rapidly from n=0 to 2 and exhibit a clear magic behavior at n=4. Figure III-6 shows the photoelectron spectra of $Li^-(NH_3)_n$ ($n \leq 16$) plotted as a function of the VDE. The photoelectron spectrum of Li^- consists of a strong band at 0.62 eV and a weak band at 2.49 eV, corresponding to the Li (2^2S)—$Li^-(^1S)$ and the Li (2^2P)—Li^- (^1S) transitions, respectively. For the 1:1 complex, three peaks are observed at 0.56, 2.05, and 2.78 eV. The first two peaks correspond to the transitions to the 2^2S- and 2^2P-type states derived from those of the Li atom, respectively, while the third one is ascribed to a transition to the 3^2S-type state as discussed later. Since the abundance of n=2 is very low as seen in Figure III-5, it is difficult to measure the photoelectron spectra accurately; the relative intensities of the ^2S and ^2P bands include some errors. The ^2S-type transitions of n=3 and 4 shift slightly to the lower binding energy, while the ^2P-type transitions of these clusters shift rapidly to the lower energy as large as more than 1 eV. For the larger clusters, the ^2S-type transition stays at almost constant VDE (*ca.* 0.45 eV) for $4 \leq n \leq 11$ and then shifts back to the higher VDE for $11 \leq n \leq 16$. On the other hand, the ^2P-type transition for $n \geq 4$ shifts further to the lower energy and almost superimposes on the transition to the neutral ground state for $n \geq 10$. The 3^2S-type transition is also found to be shifted to the lower VDE as large as *ca.* 2 eV and becomes much broader; the band cannot be distinguished for $n \geq 12$ and is expected to be superimposed on

the 2^2P-type band. The results of band positions are summarized in Figure III-7.

A typical mass spectrum of negative ions of sodium-ammonia clusters is shown in Figure III-8. Cluster ions $Na^-(NH_3)_n$ are mainly observed with a strong magic behavior at n=4 as in the case of $Li^-(NH_3)_n$. Figures III-9 and 10 show the photoelectron spectra of $Na^-(NH_3)_n$ with $n \leq 12$ and the observed band positions plotted as a function of n, respectively. As in the case of Li^-, the photoelectron spectrum of Na^- consists of a strong band at 0.55 eV and a weak band at 2.65 eV, corresponding to the transitions from the $Na^-(^1S)$ state to the neutral ground (3^2S) and excited state (3^2P), respectively. Although the PES of the 1:1 anion complex is rather noisy because of the low abundance of this ion in the cluster beam, the broad 3^2S-type band at *ca.* 0.5 eV may show the overlapping of two transitions; the main peak and shoulder are assigned to the detachment signals from two different isomers of $Na^-(NH_3)$ as discussed later. The very weak bands at near 2.4 eV can be assigned to the 3^2P-type transition, which split into two bands being due to the existence of isomers. As for n=2, the 3^2S-type band also exhibits the broad feature probably due to the presence of isomers, while the 3^2P-type transition rapidly shifts to the lower VDE and peaks at *ca.* 1.7 eV. For the larger clusters, the first band is slightly shifted to the lower VDE (*ca.* 0.04 eV) and its band width becomes smaller than those for n=2 and 3. On the other hand, the bands derived from the Na(3^2P) state shift further to the lower VDE as large as more than 1.4 eV with respect to that of Na^-. In contrast to the case of the Li^--ammonia system, I cannot observe the transition to the upper ^2S state.

Photoelectron spectra of $Na^-(H_2O)_n$

A typical mass spectrum for the negative ions of sodium-water clusters is displayed in Figure III-11. The $Na^-(H_2O)_n$ ions are observed with a magic behavior at n=4. The cluster ions assignable to $NaO^-(H_2O)_n$ and $(H_2O)_n^-$ are also detected in the higher mass region. Hydrated sodium hydroxide ions such as $NaOH^-(H_2O)_n$ are found to be insignificant, which is dissimilar to the case of copper-water negative ions reported by Misaizu *et al.* [23].

Figure III-12 shows the photoelectron spectra of $Na^-(H_2O)_n$ (n=0-7) obtained at the detachment energy of 4.67 eV (3.49 eV for $n \leq 1$). The spectra of $Na^-(H_2O)_n$ for n up to 7 all exhibit two bands as in the case of $Na^-(NH_3)_n$, but the bands shift in the opposite direction. For the 1:1 complex, the 3^2S-type band shifts to the higher VDE by 0.21 eV with respect to the $Na(3^2S)—Na^-(^1S)$ transition at 0.55 eV. As for the 3^2P-type band, the intensity is affected by the cutoff of the experimental detection efficiency in the higher VDE region. In the spectrum of n=2, the former band is observed at the VDE of 0.99 eV, while the latter band appears at *ca.* 3.8 eV. Both bands gradually shift further to the higher VDE with increasing n. These trends in the spectral shift are in marked contrast to those of the metal-ammonia systems. The amount of shifts for both the $3^2S—^1S$ and $3^2P—^1S$ transitions is almost the same and is as large as *ca.* 1.0 eV at n=7 with respect to those for Na^-. Moreover, the band width of the $3^2S—^1S$ type transition becomes much broader as n is increased through n=7.

4. Discussion

As mentioned previously, the clusters consisting of alkali atom and polar solvent molecules may serve as the most suitable model to explore microscopically the early stage of the solvated-electron formation in bulk metal-solution system. In bulk fluids, alkali metals spontaneously ionize, and

form solvated electrons and solvated metal ions. This process may be traced in the metal containing clusters with a stepwise manner. In order to probe the solvation state of metal atom in clusters, Hertel's and Fuke's group have examined the IPs of ammonia and water clusters containing Na [12] and Cs [13]. In the present work, I also study the photoelectron spectroscopy of the negative ions of these clusters. The photoelectron spectrum of the negatively-charged clusters gives information on the electronic structure of alkali-atom both in the neutral ground (^2S) and excited (^2P) states as well as the geometrical change between the anion and neutral states . In the following sections, I will discuss the solvation state of alkali atoms in detail on the basis of the results on the photoelectron and photoionization spectroscopies of these clusters, and also on the *ab initio* calculations reported in the separate paper [27, 34, 35].

Metal-ammonia clusters

Figure III-2 shows the summary of the IPs of ammoniated alkali atom clusters. Although the IPs of free atoms are different (5.392, 5.139, and 3.894 eV for Li, Na and Cs, respectively), the size dependence of these clusters are quite similar; the IPs decrease rapidly for $n \leq 4$, and decrease further for $n \geq 4$ with much slower rate. It is worth noticing that the IPs for $n \geq 4$ are almost the same irrespective of the kind of metal atoms and the limiting values of IPs are agree with the photoelectric threshold of liquid ammonia within the experimental errors (1.40-1.47 eV). These results clearly indicate that the IPs of the clusters for $n \geq 4$ depend on the solvent molecule but not on the kind of metal atoms. Fuke and coworkers discussed these observations in terms of the change in the electronic character of the neutral-ground-state metal atom from the covalent-type to the one-center (Rydberg-

like) ion-pair type with increasing n [13]. Hertel and coworkers analyzed the IP results on $Na(NH_3)_n$ by solving a one-electron Schrödinger equation in a dielectrically screened Coulomb potential [12]. They proposed the one-center Rydberg-like state for $n \leq 10$ and a two center localized state for $n > 10$. Stampfli and Bennemann [16] calculated the IP of metal-ammonia clusters using the polarizable electropole model. They suggested the single-center structure for the intermediate size ($6 < n < 25$) and the transition to two-center structure for the larger clusters; in the latter clusters, metal ion and electron are considered to be completely separated and form two centers as in the case of bulk solution. On the other hand, Hashimoto and Morokuma calculated the geometrical and electronic structures as well as IPs for both $Na(NH_3)_n$ and $Na^+(NH_3)_n$ ($n \leq 6$) by using an *ab initio* method with the 6-31+G(d) basis set and the Hartree-Fock method [20]. The optimized structures of neutral clusters are represented in the right column of Figure III-13. They found that both neutral and ion clusters with $n \geq 4$ have an interior structure where Na is surrounded by ammonia molecules. The calculations reproduce the observed IPs reasonably well and predict that the solvation energies of the cluster cations are much larger than those of the neutral clusters for $n \leq 6$, though the number of ammonia molecules in the first shell is four or five in both the neutral and ion clusters. They have also calculated the electron distribution of a singly-occupied molecular orbital (SOMO) of clusters in the neutral ground state as discussed later.

Although the above photoionization studies offer a clue to understanding the microscopic solvation process of alkali atoms in clusters, the experimental data provide information only on the energy difference between the neutral and ionized states, and thus it is difficult to obtain a deeper understanding of the solvation state of metal atoms. Moreover, as argued by Hashimoto [20] and Landman [15], the solvation state of alkali atom in clusters is determined by the delicate balance between the interaction of a diffuse electron with the

solvent molecules and the metal-solvent interaction; it seems to be difficult to describe the system using a semi-empirical model potential. In order to obtain further information on the electronic structure of solvated alkali atoms, I study the photoelectron spectroscopy of ammoniated alkali-atom anions as follows.

The photoelectron spectrum of alkali-atom anion consists of two bands due to the transitions from the ^1S anion state to the ^2S neutral ground and ^2P excited states; as shown in Figures III-6 and III-9, these bands are observed at the VDEs of 0.62 and 2.49 eV for Li^-, and at 0.55 and 2.65 eV for Na^-, respectively. The ^2P band of these anions is much weaker than the ^2S band because it corresponds to a two-electron excitation process and is formally forbidden. For $Li^-(NH_3)$, the spectrum exhibits two bands at the VDEs of 0.47 and *ca.* 2.6 eV derived from the above transitions of Li^- (see Figure III-6). Recently, Hashimoto and Kamimoto (HK) have calculated the geometry and electronic structure of both the negatively charged and neutral Li-ammonia clusters as well as the VDEs by the *ab initio* MO method [28]. The results are represented in Figures III-14 and 15. As shown in Figure III-15, $Li^-(NH_3)$ has two geometrical isomers with an energy difference of 8.2 kcal/mol including zero-point vibrational energy correction; the total binding energies of the two isomers are 11.3 and 3.1 kcal/mol, respectively. The stable isomer (type-I) has the structure similar to that of the neutral complex, in which ammonia molecule is bound to Li^- by the nitrogen atom, while, in the less stable isomer (type-II), NH_3 is bound to Li^- by the hydrogen atoms as in the cases of Cu^- and halide anions with water molecules [23,29-31]. The VDEs of the 2^2S state for the type-I and II isomers have also been calculated as 0.44 and 0.76 eV, respectively, at CCSD/6-311++G(d,p)//MP2/6-311++G(d,p) level with a frozen core approximation. Based on these theoretical results, the peak at 0.56 eV can be assigned to the 2^2S-type transition of the more stable isomer. Although theoretical results are not available, the band at *ca.* 2.0 eV can be

reasonably assigned to the 2^2P-type transition by considering the red-shift trend of this transition for larger clusters as seen in Figure III-6. As shown in Figure III-16, HK have also carried out similar calculations for $Na^-(NH_3)$ and found two geometrical isomers similar to the type-I and II of $Li^-(NH_3)$, but with a much smaller energy difference (1.4 kcal/mol); total binding energies and VDEs of the 3^2S-type transition for the two isomers are 4.3 kcal/mol and 0.35 eV, and 2.9 kcal/mol and 0.65 eV, respectively. These theoretical results suggest that the strong band and a shoulder observed at 0.6 eV and *ca.* 0.4 eV for $Na^-(NH_3)$ as shown in Figure III-9b correspond to the 3^2S-type transitions of the unstable (II) and stable (I) isomers, respectively. The fact, that the spectrum of the unstable isomer is observed with appreciable intensity for $Na^-(NH_3)$ and not for $Li^-(NH_3)$, seems to be consistent with much smaller difference in the total binding energy of two isomers for $Na^-(NH_3)$. The most significant difference in the spectra of these complexes is the appearance of the third band at 2.78 eV for $Li^-(NH_3)$, but not for $Na^-(NH_3)$ (see Figures III-6b and III-9b). As expected from the large shift of the ^2P-type transition upon complexation, a higher excited state such as the Li (3^2S) and Na(4^2S) levels, located at 3.99_3 and 3.74_1 eV above the ^1S anion levels, respectively, would be shifted to the present energy region. For $Li^-(NH_3)_n$ ($n \leq 11$), I also observe the similar weak bands at *ca.* 1 eV above the 2^2P-type transition as seen in Figure III-6. These arguments suggest that the 2.78-eV band of $Li^-(NH_3)$ can be assigned to the $3^2S—^1S$ transition corresponding to the two-electron excitation process. At present, I have no clear answer why the $4^2S—^1S$ transition cannot be observed for $Na^-(NH_3)$.

As for $Na^-(NH_3)_2$, the ^2S-type band shows a broad feature and may indicate the presence of isomers as shown in Figure III-9c. According to the HK's calculations [35] represented in Figure III-17, there are at least three relatively stable isomers. The more stable (I) and less stable (II) isomers have the similar structures to those of the 1:1 anion complex, in which two

ammonia molecules are bound to Na by the N and H atoms with C_2 symmetry, respectively; the total binding energies and VDEs of these isomers are 11.5 kcal/mol and 0.32 eV (type-I), and 5.8 kcal/mol and 0.78 eV (type-II), respectively. The other isomer (III) has a C_s geometry, in which one ammonia molecule is bound to Na^- by the N atom and the other ammonia molecule is bound to the first ammonia by N through hydrogen bond; the total binding energy and VDE are calculated to be 6.7 kcal and 0.26 eV, respectively. These theoretical results indicate that the type-I isomer becomes much more stable than the other isomers with increasing n and also the VDE of the isomer with N—H interaction (type-II) is shifted to the higher VDE by the ligation of the ammonia molecules. The latter trend in the spectral shifts is also observed in the spectra of the Na-water system as discussed below and due to much larger electrostatic interaction in the cluster anion than that in the neutral cluster. Therefore, the main peak at *ca.* 0.5 eV and the shoulder at *ca.* 0.4 eV can be assigned to the 3^2S-type transitions of isomers I and III, respectively, while a weak tail seen in the higher VDE region of the main peak may be tentatively ascribed to the transition of the isomer II. As mentioned previously, the ^2P-type transition is very weak because of its forbidden nature and also there exist isomers for small size clusters with similar binding energies. These factors as well as the low abundance of the $Na^-(NH_3)_2$ ions as demonstrated in Figure III-8 make it difficult to locate the peak position of the 3^2P-type band. I tentatively assign the band at *ca.* 1.7 eV to this transition for the most stable type-I isomer; the band shifts to the lower VDE by almost 1 eV with respect to that of Na^-. On the other hand, HK's calculations also predict three isomers for $Li^-(NH_3)_2$ with the similar structures as those of $Na^-(NH_3)_2$; total binding energies and VDEs are calculated to be 25.7 kcal/mol and 0.43 eV, 6.3 kcal/mol and 0.91 eV, and 14.2 kcal/mol and 0.31 eV for the type I-III isomers, respectively [27]. Based on these theoretical results, the strong band at 0.56 eV can be assigned to the transition to the neutral ground

state of the type-I isomer (Li^-—N interaction), while a weak shoulder at *ca.* 1.0 eV may correspond to the 2^2S transition of the type-II isomer. As mentioned in the previous section, $Li^-(NH_3)_2$ is the least abundant ion and the relative intensity of the spectrum in the energy region above 1 eV is not accurate enough for the intensity argument. But I believe that the band at *ca.* 1.5 eV correspond to the 2^2P transition of the type-I isomer.

The PES of $Na^-(NH_3)_3$ shown in Figure III-9d exhibits two peaks at 0.51 and 1.38 eV. The spectrum exhibits an abrupt decrease in the band width of the 3^2S transition from n=2 to 3; the band width becomes as sharp as that for Na^-. These results seem to be consistent with the HK's calculations that the type-I isomer of n=3, in which all ammonia molecules are bound to Na by the N atom, becomes more stable than the other isomers with Na—H bond. The spectra of $Na^-(NH_3)_n$ for $n\geq4$ also exhibit the sharp 3^2S transition and may indicate that the type-I isomer is increasingly favored for the larger clusters as predicted by the calculations. Thus the bands at 0.51 and 1.38 eV can be assigned to the 3^2S and 3^2P transitions of the type-I isomer. As for $Li^-(NH_3)_3$, the PES shown in Figure III-6d exhibits two transitions at 0.50 and *ca.* 1.0 eV. Unfortunately, the theoretical results are not available for $Li^-(NH_3)_n$ ($n\geq3$), however, the strongest band at 0.5 eV can be assigned to the 2^2S-type transition of the type-I isomer, while the shoulder at *ca.* 1.0 eV may correspond to that for the type-III isomer in analogy with the results on n=2. The spectrum of $Li^-(NH_3)_3$ also displays the other two bands at 1.41 and 2.30 eV, which are reasonably assigned to the transitions to the 2^2P and 3^2S-type states. These bands are shifted by 1.03 and 1.69 eV with respect to those for Li^-.

The above assignments of the photoelectron spectra for both $Li(NH_3)_n$ and $Na(NH_3)_n$ with $n\leq3$ indicate that the ^2S-type transition of the type-I isomer with the metal—N bond is also shifted to the lower VDE, though the amount of shift is much smaller than that for the ^2P-type transition; the shift in VDE

of $Li(NH_3)_n$ with respect to the $Li^-(^2S)$ are found to be about 0.06 and 0.12 eV for n=1 to 3, while those for $Na(NH_3)_{1,3}$ are *ca.* 0.15 and 0.04 eV, respectively. These results imply that the solvation energy of the neutral cluster is equal to or larger than that in the anion state as predicted by the HK's calculations [28] represented in Figure III-13. They have also calculated the electron distribution of SOMO for $Li(NH_3)_n$ and $Na(NH_3)_n$ in which the *ns* orbital of Li and Na is dominated, and found that the SOMO electron density for $n \leq 2$ is mainly distributed in the vicinity of the alkali atom and extends in space in the directions where NH_3 molecules do not exist. On the other hand, for n=3, the SOMO density is predicted to extend in space on and between the NH_3 molecules rather than on the metal atom. These calculations suggest that the stabilization energy of neutral clusters as large as that of the anion clusters seems to be due to the delocalization of SOMO in addition to the metal atom—N bond formation.

As mentioned previously, the experimental and theoretical results suggest that the type-I isomer with metal—N interaction is increasingly favored with increasing n for both the Li^-- and Na^--ammonia systems as in the case of neutral clusters. Thus the observed photoelectron bands for $n \geq 4$ are considered to be mainly due to the transitions of the type-I isomers. In other words, the photodetachment process of the clusters with $n \geq 3$ corresponds to the transition from the negative state to near the potential minimum of the neutral states. As seen in Figures III-5 and III-8, both $Na^-(NH_3)_n$ and $Li^-(NH_3)_n$ exhibit the clear magic behavior at n=4. Although the clusters are generated by laser vaporization and the formation process of these clusters would be quite complex, the stability of the cluster ions may reflect on its abundance in the mass spectrum. This argument seems to suggest that $Na^-(NH_3)_4$ and $Li^-(NH_3)_4$ are more stable than its neighbors, the first solvation shell of these alkali-atom anion may be closed at $n \approx 4$. The photoelectron spectra of the Na^-- and Li^--ammonia clusters for $n \geq 4$ exhibit the distinct

features. As for $Na^-(NH_3)_n$, the 3^2P-type transition shifts further to the lower VDE for n=4, and then shifts with much slower rate for $n \geq 5$ (the amount of shift of n=5 is more than 1.4 eV with respect to that of Na^-). The rapid change in the rate of shift between n=4 and 5 may be ascribed to the formation of solvation shell about Na^-. Moreover, the band width of the 3^2P-type transition increase systematically with increasing n up to 12 as seen in Figure III-9, though the shift in the band position almost saturates for $n \geq 5$. These results clearly indicate that the electronic structure of the Na atom is affected further with the addition of ammonia molecules even after the first solvation shell is closed. On the other hand, the 2^2P-type transition of $Li^-(NH_3)_n$ ($4 \leq n \leq 9$) shifts to the lower VDE as large as 1.4 eV and it almost become degenerate with the transition to the neutral ground state for $n \geq 10$ (see Figure III-6). The 3^2S—^1S transition at 2.21 eV for n=4 also gradually shifts further to the lower VDE up to n=11 and then it smears out for $n \geq 12$. Therefore, the above results on the PES for both $Li^-(NH_3)_n$ and $Na^-(NH_3)_n$ clearly indicate the dramatic decrease in the ^2P—^2S energy separation by the ligation of ammonia molecules being coincident with the rapid decrease of IP for the neutral clusters as seen in Figure III-2.

The other interesting feature of the photoelectron spectra of Li^- (Na^-)-ammonia system is that the ^2S-type band is also shifted slightly to the lower VDE with increasing cluster size as seen in Figures III-6 and III-9. In the case of $Li^-(NH_3)_n$, the shift in VDE is found to be about 0.06 and 0.19 eV for n=1 and 4 with respect to the $Li^-(^2S)$, respectively. On the other hand, the shift in VDE of $Na^-(NH_3)_n$ clusters is found to be much smaller for n=3 and 4 (0.04 eV). For larger clusters, VDE of the neutral ground state also stays at *ca.* 0.51 eV. As mentioned previously, the photoelectron bands of negatively charged ions solvated in clusters generally shift to the higher VDE [23,29-31], because of much larger solvation energy in the negative states. Thus these results are quite anomalous and indicate the larger binding energy of the

neutral clusters than that of the cluster anions as in the case for $n \leq 3$ even after the first shell is closed. These results as well as the above findings that the ^2P-type transition is still affected for $n \geq 5$ may indicate the direct interaction of the second-shell ammonia molecules with the valence electron of the metal atom. As mentioned previously, the calculations show the extensive delocalization of the SOMO electron density of metal atom for $Li(NH_3)_3$ and $Na(NH_3)_3$. HK also found the similar delocalization of SOMO for these clusters with $4 \leq n \leq 6$. If this is the case, the diffuse SOMO electron may interact with even the second-shell ammonia molecules. The observations, that the IPs of $M(NH_3)_n$ $n \geq 5$ (M=Li, Na, Cs) are independent of the kind of metal atoms, are also explainable by the diffuse SOMO, because the electron being removed in the ionization process is considered to come from the ammonia molecules rather that the metal atom.

As shown in Figure III-10, the ^2S-type transition of $Na^-(NH_3)_n$ ($n \geq 5$) slightly shifts back to the higher VDE. The similar shift is also observed for $Li^-(NH_3)_n$ ($n \geq 10$) as seen in Figure III-7. These tendencies may be consistent with the results on the VDEs of $(NH_3)_n^-$ reported by Bowen and coworkers [8], in which the estimated value of VDE(∞) is in agreement with the photoemission threshold of electrons from dilute metal-ammonia solution ranging from 1.42-1.45 eV. As mentioned previously, the ground-state $Na(NH_3)_n$ and $Li(NH_3)_n$ are the one-center (Rydberg-like) ion-pair state for smaller clusters, but it may tend to become a two-center alkali cation-surface electron state for sufficiently large clusters. If this occurs, the VDE of these clusters is expected to converge to the same limit as that for $(NH_3)_n^-$, because the interaction between the metal atom (and metal cation) and the electron in both the negatively charged and neutral states becomes negligibly small in infinite-sized clusters. The observed red-shift of the ^2S state as well as the near degeneracy of the ^2S and ^2P states for large n may indicate that the valence electron on the metal atom gradually move to the surrounding solvent

molecules. Therefore, the present experimental results as well as the theoretical predictions suggest that the alkali atom is spontaneously ionized in rather small ammonia clusters.

Metal-water clusters

Figure III-4 shows the IPs of $Li(H_2O)_n$ plotted versus $(n+1)^{-1/3}$ obtained by the photoionization threshold measurements. I also plot the results for $Na(H_2O)_n$ and $Cs(H_2O)_n$ reported previously [13,14]. As in the case of metal-ammonia systems, the IPs of these clusters are independent on the kind of alkali atoms for $n \geq 4$. The most surprising observation is that the IP becomes constant within the uncertainty of the photoionization threshold measurement (± 0.03 eV). Moreover, the limiting value ($n \rightarrow \infty$) coincides with the bulk photoelectric threshold of ice and the extrapolated value of the VDE of $(H_2O)_n^-$ as well [8]. Until now, three theoretical groups have made efforts to interpret these anomalous IP behaviors. Barnett and Landman [15] have calculated the geometrical and electronic structures of $Na(H_2O)_n$ ($n \leq 8$) using the local spin density functional method and shown that the structure of the neutral $Na(H_2O)_n$ clusters resembles that of $Na^+(H_2O)_n$. They have also predicted that the saturation of IP for $n>4$ is due to the formation of a molecular shell about the Na for $n \approx 4$, accompanied by exclusion of the valence electron of alkali atom from the hydration cavity; the electron is delocalized in a surface Rydberg-like state as discussed for the metal-ammonia systems. Hashimoto and Morokuma have also investigated extensively the geometrical and electronic structures for $Na(H_2O)_n$ and $Na^+(H_2O)_n$ ($n \leq 6$) using the *ab initio* MO method [18,19]. As for the neutral clusters, they found isomers with Na—O interactions; the most stable isomer has a surface structure, in which Na sits on the cyclic hydrogen-bonded water clusters as illustrated in the right column of

Figure III-18, while, in the second stable isomer, Na is surrounded by water molecules by Na—O bond (interior structure). The difference in total binding energy for these isomer is found to be rather small [2.0, 1.6, 4.2 and 5.1 kcal/mol for n=3-6, respectively, at MP2/6-31+G(d)//HF/6-31+G(d) level] and the isomer with the surface structure becomes increasingly favored for larger clusters. Moreover, the calculated IPs for the surface isomers agree reasonably well with the observed IPs. Based on these results as well as the result that the first solvation shell of the surface-type clusters is closed with four water molecules, they have ascribed the origin of the saturation behavior of IP to the structural feature of this isomer; in this case, the excess water molecules are bound to those in the first shell by hydrogen bond and, as a result, their effect on the local electronic structure of Na becomes much smaller for $n \geq 5$. These theoretical predictions are considered to be coherent with the observed IP behavior for $Na(H_2O)_n$. However, recently, HK have also made *ab initio* calculations on the Li-H_2O clusters and found that, in contrast to the case of Na, the most stable isomers have the interior structure similar to those of $Li^+(H_2O)_n$ for $n \leq 6$ [34]. If this is the case, the gradual decrease of IP is expected even for $n \geq 5$ as observed for the metal-ammonia systems. Since both Li- and Na-water clusters shows the constant IP behavior as shown in Figure III-4, the above prediction for the origin of the constant IP behavior is necessary for reconsideration.

In order to obtain further information on the electronic structure of metal-water systems, I also carry out the photoelectron spectroscopy of $Na^-(H_2O)_n$ ($n \leq 7$). Figure III-12 shows the spectra obtained at the detachment energy of 3.49 eV for n=1 and 2, and at 4.66 eV for $n \geq 3$, respectively. In contrast to the case of metal-ammonia systems, both the 3^2S- and 3^2P-type transitions shift to the higher VDE by a similar amount. The spectral shifts of the former transition from that of Na^- is 0.21, 0.44, and 0.58 eV for n=1-3, respectively. Similar blue shift in VDE has also been observed for $Cu^-(H_2O)_n$

[23], but the amount of shift is much larger than those for the Na system (0.35, 0.73, and 1.05 eV for n=1-3, respectively). Recently, Iwata and Zhan [29] have calculated the structures and VDEs of $Cu^-(H_2O)_n$ ($n \leq 2$) using *ab initio* method. These authors have found that the Cu^- anion is symmetrically hydrated by Cu^-—H interaction; Cu^-—H distance for n=1 is 0.272 nm with MP2 level. Their calculations (at MP4SDTQ level) reproduce the observed VDEs with reasonable accuracy. And also, the difference in the shift of VDE between Cu^-- and Na^--water clusters have been ascribed to that radius of these ions; the ion radius has been estimated to be 1.86 and 2.65 eV for Cu^- and Na^-, respectively. As for Na^--water clusters, HK have also calculated the structures, total binding energies, and VDEs for $n \leq 4$. The optimized structures are represented in the left column of Figure III-18. They have found two isomers with symmetrical Na^-—H (0.377 nm) and Na^-—O (0.233 nm) bonds, but the former one is more stable by 1 kcal/mol. For larger clusters, HK have also predicted various isomers with Na^-—H and Na^-—O interactions, however, the isomers, in which all water molecules is bound to Na^- by H atom, are more stable by 3-5 kcal/mol than the isomers with Na^-—O interaction as in the case of neutral clusters. These theoretical results suggest that the observed photoelectron bands are mainly due to the former isomers; the origin of the blue shift in VDE is ascribed to much larger electrostatic interaction in the anion state than that in the neutral state. Therefore, these theoretical results as well as the observed trends in the PES indicate that, in contrast to the case of $Na(NH_3)_n$, the potential energy minimum of $Na(H_2O)_n$ cannot be probed by the photoelectron spectroscopy of its anions because of the large difference in the geometrical structures of the anion and neutral states. Moreover, the fact, that the energy separation of the 3^2S and 3^2P states are almost the same for $n \leq 7$ as seen in Figure III-12, may suggest that the electronic structure of alkali atoms is not affected appreciably by hydration

when the metal—H interaction is dominant; the *ns* electron density is localized on the metal atom as expected from the theoretical calculations.

Although $Na(H_2O)_n^-$ is found to be not appropriate to clarify the origin of the anomalous IP behavior by the photoelectron spectroscopy, this seems to be not the case for $Li(H_2O)_n^-$. Recently, HK have also made the *ab initio* calculation for the latter clusters and found that the interior structure is the most stable in both the anion and neutral states as shown in Figure III-19. They have also found that, as in the case of $Na(NH_3)_n$, the SOMO electron of the $Li(H_2O)_n$ clusters with n=4-6 having the interior structure is delocalized in the surface state. These results encourage us to explore the solvation state of alkali atom in water clusters. The PES experiments of Li-water systems are now underway.

5. Conclusions

The photoionization and photoelectron spectroscopies of alkali-metals in polar solvent clusters have been investigated. For $Na(NH_3)_n$ and $Li(NH_3)_n$, the electronic structure of alkali atoms in ammonia clusters has found to be extensively changed with increasing the cluster size. Especially, in the case of $Li(NH_3)_n$, the 3^2S and 2^2P-type states of clusters are found to be dramatically stabilized and almost become degenerate with the ground state for $n \geq 10$. This trend in PES is consistent with the theoretical results that the SOMO election density of alkali atom is delocalized over and beyond the solvent molecules with increasing n. These results also suggest that the photoionization process of the larger clusters correspond to the ejection of an electron delocalized over the surface region of clusters. The observations, that the Li-, Na- and Cs-ammonia clusters have the same IP value for $n \geq 5$, support the above

conclusions. The present results on PES exhibit the early stage of the spontaneous ionization of alkali-metal atom in ammonia clusters.

As for the alkali atom-water clusters, IPs are found to be independent of the kind of metal atoms and become constant for $n \geq 5$. In order to clarify the origin of these anomalous IP behaviors, I have also examined the PES of $Na^-(H_2O)_n$, Because of the large difference in the geometrical structures of the anion and neutral states, I cannot obtain information on the electronic structure of the neutral clusters. The experimental results on IPs as well as theoretical calculations suggest that alkali atom is also dissolved in small water clusters, though the solvation state of the alkali atom in water cluster is different from that in ammonia cluster due to the strong hydrogen bond in the former systems. The present study suggest that further experimental and theoretical investigations are needed to fully understand the electronic structure of alkali atom embedded in water clusters.

References for Chapter III

[1] Dogonadze, R. R.; Kalman, E.; Kornyshev, A. A.; Ulstrup, J. Eds.; *The Chemical Physics of Solvation* Part C; Elsevier; Amsterdam 1988.

[2] Gauduel, Y.; In *Ultrafast Dynamics of Chemical Systems*; J. D. Simon, Ed.;Kluwer Academic Publishers.; Netherlands 1994; pp.81-136.

[3] Alfano, J. C.; Walhout, P. K.; Kimura, Y.; Barbara, P. F. *J. Chem. Phys.* **1993**, *98*, 5996.

[4] Tuttle, Jr., T. R.; Golden, S. *J. Phys. Chem.* **1991**, *95*, 5725.

[5] Haberland, H.; Schindler, H. -G.; Worksnop, D. R. *Ber. Bunsenges. Phys. Chem.* **1984**, *88*, 270.

[6] Haberland, H.; Ludewigt, C.; Schindler, H. -G.; Worksnop, D. R. *Surface Sci.* **1985**, *156*, 157.

[7] Coe, J. V.; Lee, G. H.; Eaton, J. G.; Sarkas, H. W.; Bowen, K. H.; Ludewigt, C.; Haberland, H.; Worsnop, D. R. *J. Chem. Phys.* **1990**, *92*, 3980.

[8] Lee, G. H.; Arnold, S. T.; Eaton, J. G.; Sarkas, H. W.; Bowen, K. H.; Ludewigt, C.; Haberland, H. *Z. Phys.* **1991**, *D 20*, 9.

[9] Barnett, R. N.; Landman, U.; Cleveland, C. L.; Jortner, J. *Chem. Phys. Lett.* **1988**, *145*, 382.

[10] Barnett, R. N.; Landman, U.; Cleveland, C. L.; Kestner, N. R.; Jortner, J. *Chem. Phys. Lett.* **1988**, *148*, 249.

[11] Campagnola, P. J.; Lanrich, D. J.; DeLuca, M. J.; Johnson, M. A. *J. Chem. Phys.* **1991**, 94, 5240.

[12] Hertel, I. V.; Hüglin, C.; Nitsch, C.; Schulz, C. P. *Phys. Rev. Lett.* **1991**, *67*, 1767.

[13] Misaizu, F.; Tsukamoto, K.; Sanekata, M.; Fuke, K. *Chem. Phys. Lett.* **1992**, *188*, 241.

[14] Martyna, G. J.; Klein, M. L. *J. Phys. Chem.* **1991**, *95*, 515.

[15] Barnett, R. N.; Landman, U. *Phys. Rev. Lett.* **1993**, *70*, 1775.

[16] Stampfli, P.; Bennemann, K. H. *Comput. Matter. Sci.* **1994**, *2*, 578.

[17] Hashimoto, K.; He, S.; Morokuma, K. *Chem. Phys. Lett.* **1993**, *206*, 297.

[18] Hashimoto, K.; Morokuma, K. *Chem. Phys. Lett.* **1994**, *223*, 423.

[19] Hashimoto, K.; Morokuma, K. *J. Am. Chem. Soc.* **1994**, *116* , 11436.

[20] Hashimoto, K.; Morokuma, K. *J. Am. Chem. Soc.* **1995**, *117*, 4151.

[21] Takasu, R.; Hashimoto, K.; Fuke, K. *Chem. Phys. Lett.* **1996**, *258*, 94.

[22] Misaizu, F.; Sanekata, M.; Tsukamoto, K.; Fuke, K.; Iwata, S. *J. Phys. Chem.* **1992**, *96*, 8259.

[23] Misaizu, F.; Tsukamoto, K.; Sanekata, M.; Fuke, K. *Laser Chem.* **1995**, *15*, 195.

[24] Schultz, C.P.; Haugstätter, R.; Tittes, H.-U.; Hertel, I. V. *Z. Phys.* **1988**, *D10*, 279.

[25] Bewig, L.; Buck, U.; Rakowsky, S.; Reymann, M.; Steinbach, C. In *Abstract of 8th International Symposium on Small Particles and Inorganic Clusters*; Kopenhagen, 1996.

[26] Sanekata, M.; Misaizu, F.; Fuke, K.; Iwata, S.; Hashimoto, K. *J. Am. Chem. Soc.* **1995**, *117*, 747.

[27] Hashimoto, K.; Kamimoto, T.; Fuke, K *Chem. Phys. Lett.* **1997**, *266*, 7.

[28] Hashimoto, K.; Kamimoto, T. to be submitted.

[29] Zhan, C. -G.; Iwata, S. *Chem. Phys. Lett.* **1995**, *232*, 72.

[30] Markovich, G.; Giniger, R.; Levin, M.; Cheshnovsky, O. *J. Chem. Phys.* **1991**, *95*, 9416.
[31] Arnold, D. W.; Bradforth, E. H.; Kim, E. H.; Neumark, D. M. *J. Chem. Phys.* **1995**, *102*, 3510.
[32] A weak tail obserbed in the higher VDE region of the 0.56-eV band (see Figure III-6b) may correspond to the 2^2S transition of the type-II isomer, however, I cannot conclude definitively with the present PES resolution.
[33] Nitsch, C.; Schultz, C. P.; Gerber, A.; Zimmermann-Edling, W.; Hertel, I.V. *Z. Phys.* **1992**, *D22*, 651.
[34] Kamimoto, T.; Hashimoto, K. In *Structures and Dynamics of Clusters*; Kondow, T.; Kaya, K.; Terasaki, A. Eds.; Universal Academy Press. Inc.; Tokyo 1996; pp.563-572.
[35] Hashimoto, K.; Kamimoto, T. In *Structures and Dynamics of Clusters*; Kondow, T.; Kaya, K.; Terasaki, A. Eds.; Universal Academy Press. Inc.; Tokyo 1996; pp.573-580.

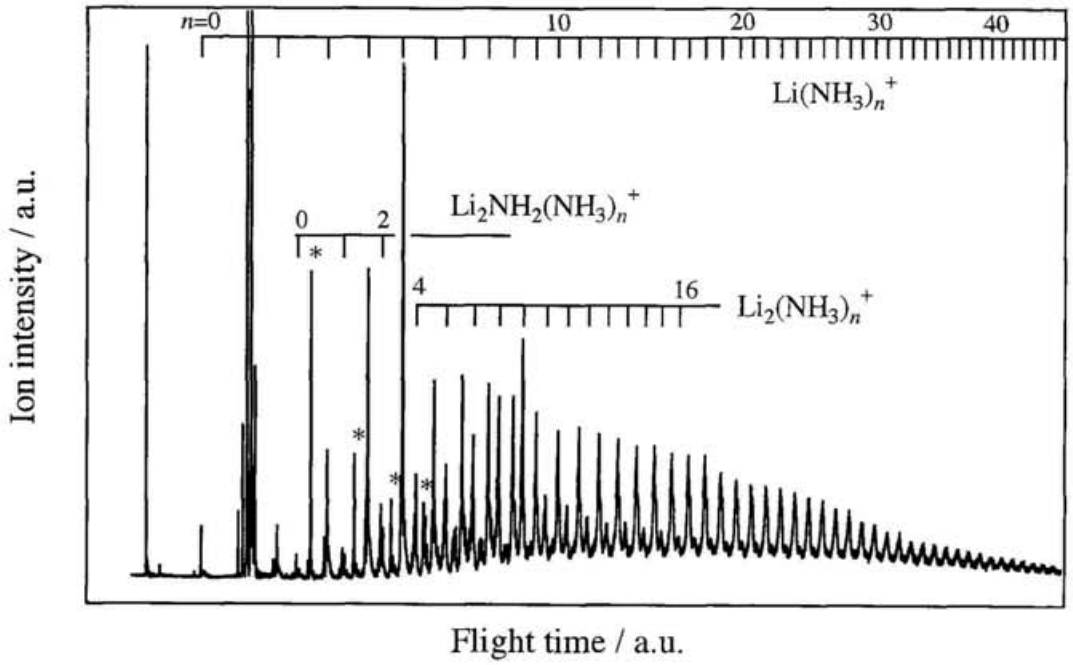

Figure III-1. Typical photoionization spectrum of ammonia clusters containing Li and Li_2 produced by irradiation at 193 nm. The outstanding peaks are observed at n=4 and 8 for $Li(NH_3)_n$ and $Li_2(NH_3)_n$, respectively. Peaks marked by asterisk correspond to the $NH_4(NH_3)_n^+$ cluster ions produced by the resonance-enhanced two-photon ionization of ammonia clusters, which coexist in the cluster beam.

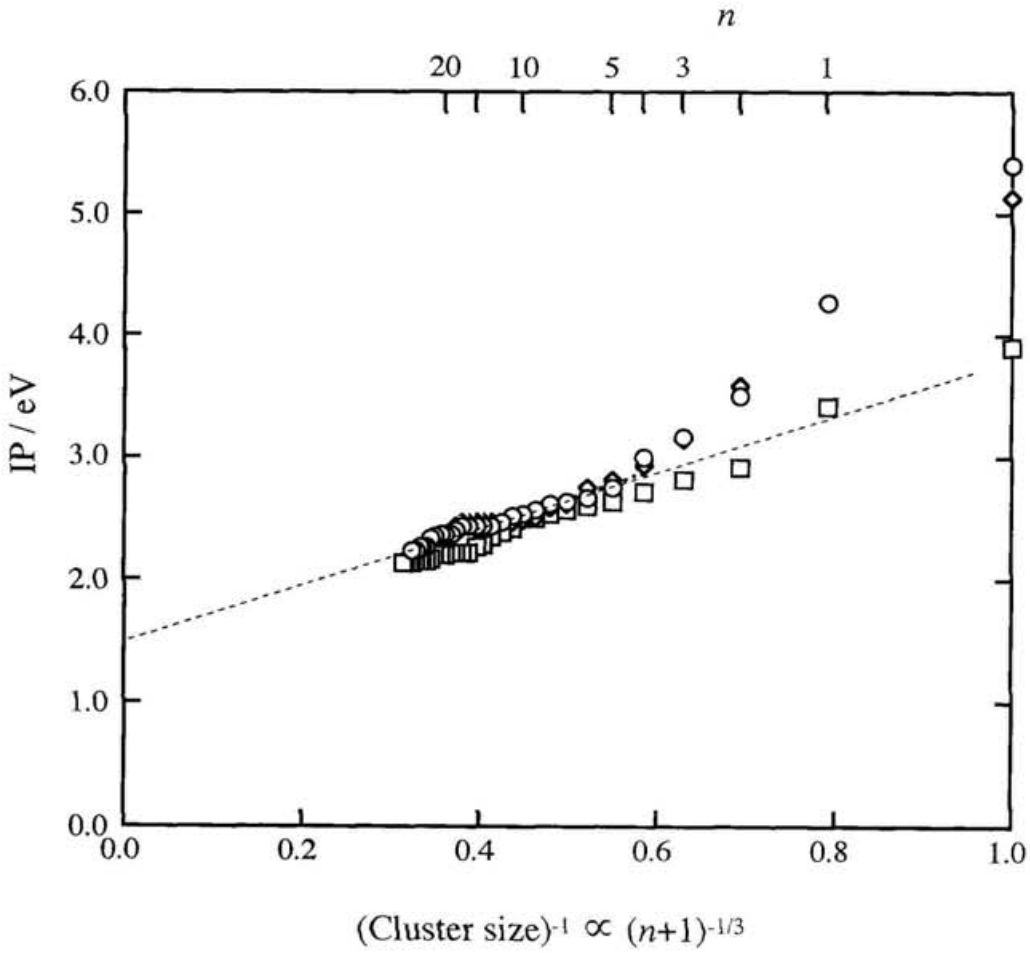

Figure III-2. Ionization potentials (IPs) of $M(NH_3)_n$ [M=Li (○), Na (◇), Cs (□)] plotted as a function of $(n+1)^{-1/3}$. IPs of the $Cs(NH_3)_n$ are cited from ref. 13. For comparison, IPs of Na-ammonia clusters cited from ref. 33 are also plotted. The result of the least-squares fitting $Li(NH_3)_n$ for $n \geq 5$ is also shown by the dotted line; the extrapolated value for $n \rightarrow \infty$ is 1.47 eV.

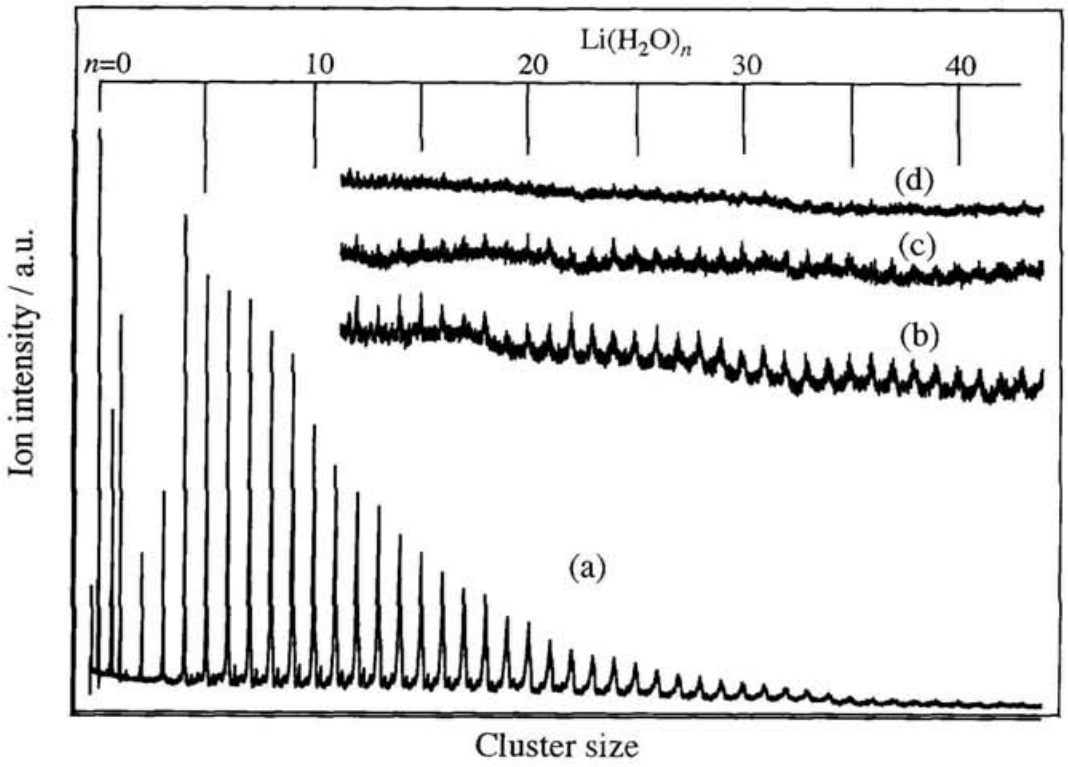

Figure III-3. Typical TOF mass spectra of $Li(H_2O)_n$ produced by the photoionization at: (a) 193 nm (6.42 eV), (b) 392 nm (3.16 eV), (c) 396 nm (3.13 eV), and (d) 398 nm (3.12eV). Traces b-d are magnified at a factors of *ca.* 40.

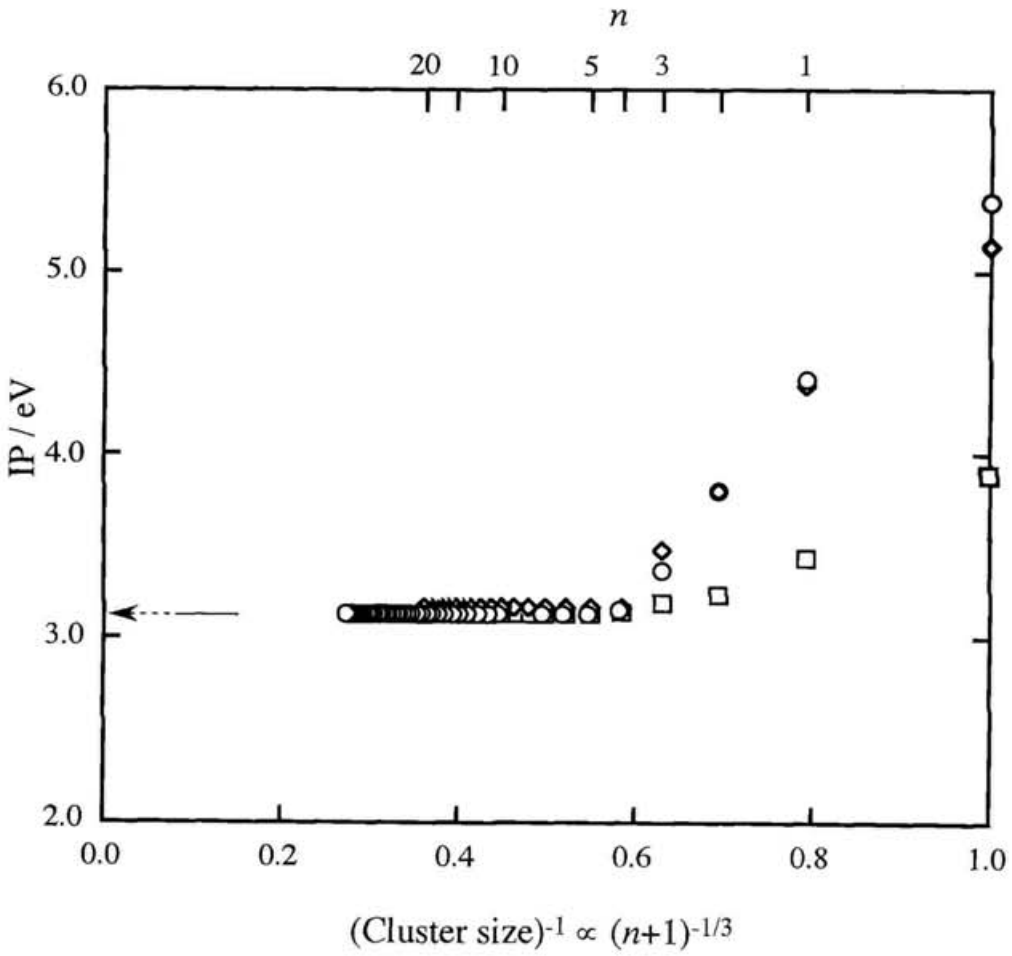

Figure III-4. Ionization potentials (IPs) of $Li(H_2O)_n$ (○) plotted as a function of (cluster radius)$^{-1}$ ∝ $(n+1)^{-1/3}$. IPs for $n \geq 5$ are 3.12±0.02 eV. For comparison, the IPs of $Na(H_2O)_n$ (◇) and $Cs(H_2O)_n$ (□) cited from refs. 12 and 13 are also plotted.

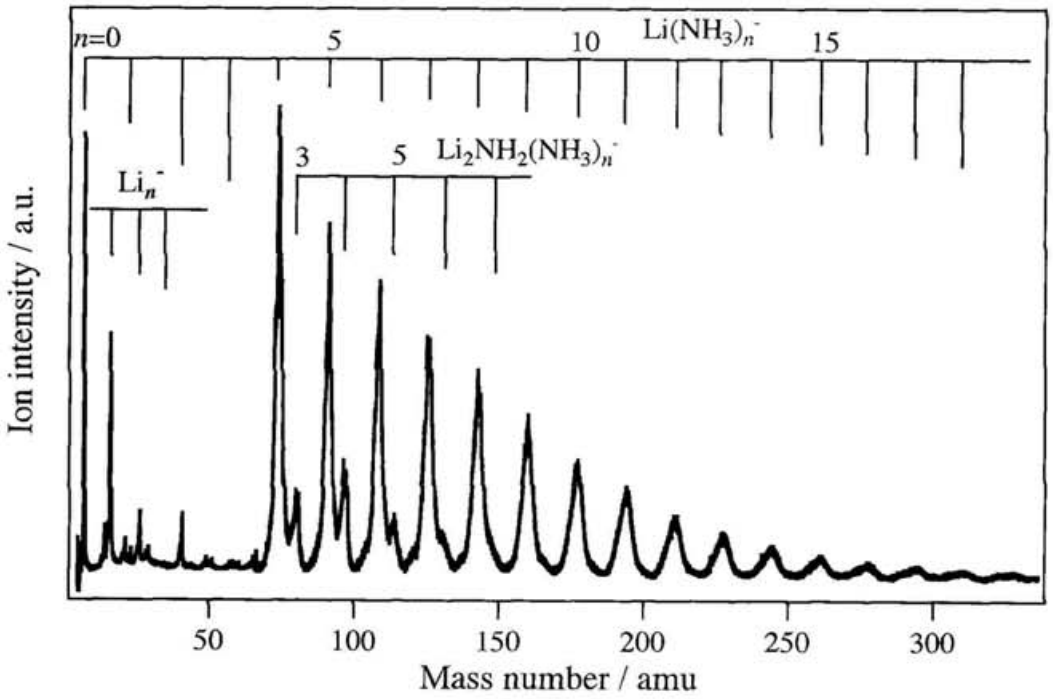

Figure III-5. Typical TOF mass spectrum of the Li_n^- -ammonia system.

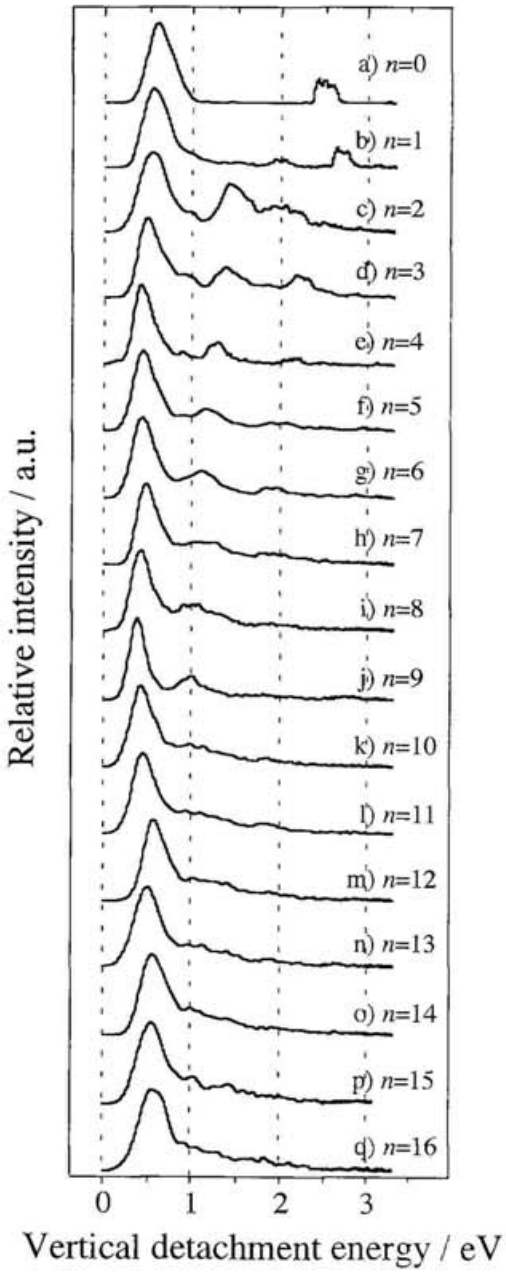

Figure III-6. Photoelectron spectra of $Li^-(NH_3)_n$ (n=0-16) collected using a phtodetachment energy of 3.49 eV (355 nm). The spectra are normalized at the peaks correspond to $2^2S—^1S$ transition of Li.

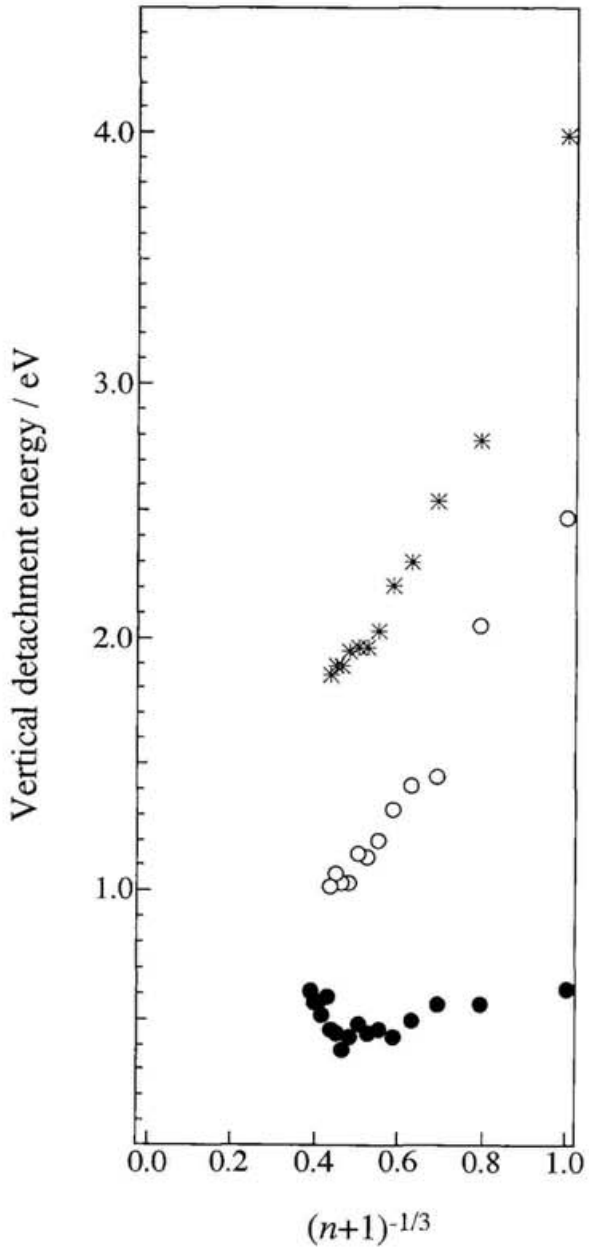

Figure III-7. VDEs of the observed transitions for $Li^-(NH_3)_n$ plotted as a function of $(n+1)^{-1/3}$; (a) $2^2S-{}^1S$(●), (b) $2^2P-{}^1S$(○) and (c) $3^2S-{}^1S$ (∗) type transitions.

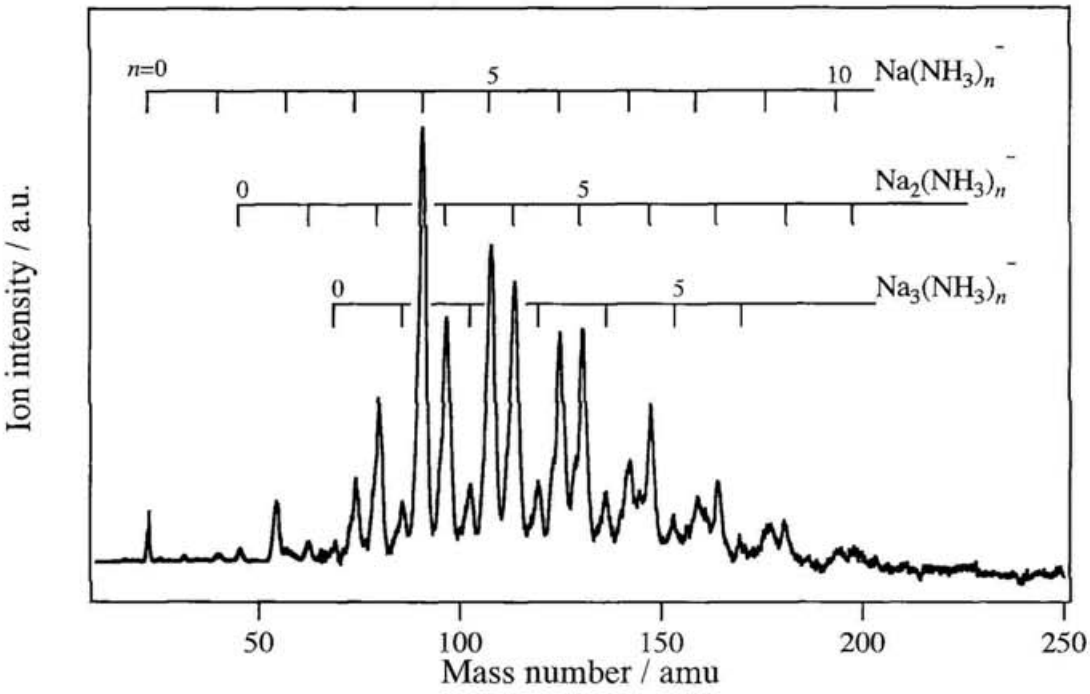

Figure III-8. Typical TOF mass spectrum of Na^--ammonia clusters.

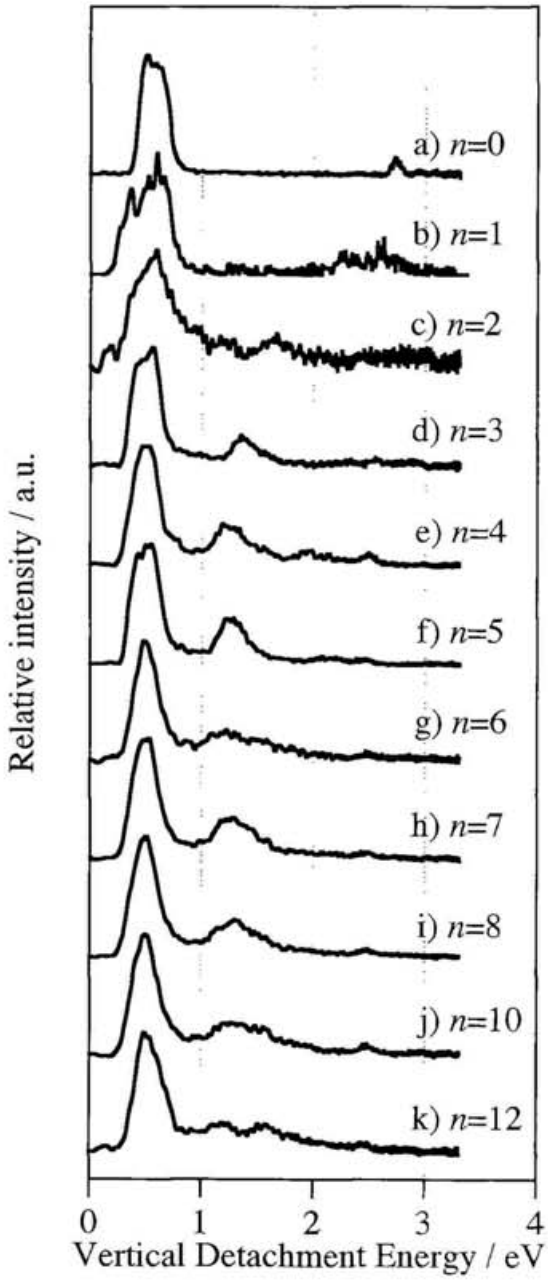

Figure III-9. Photoelectron spectra of $Na^-(NH_3)_n$ (n=0-12), collected using a phtodetachment energy of 3.49 eV (355 nm). The spectra are normalized at the peak of 3 ^2S—^1S type transition.

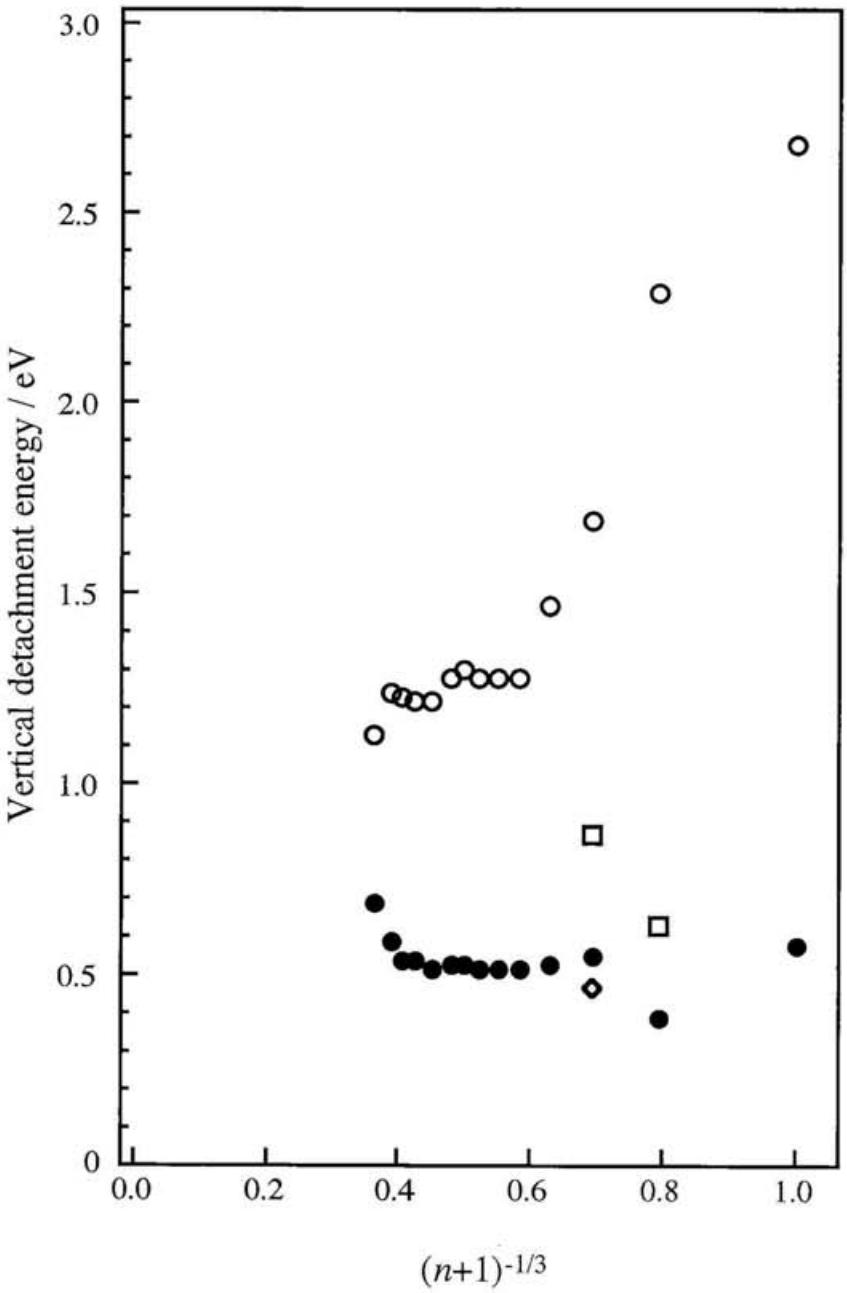

Figure III-10. VDEs of the observed transitions for Na $^-(NH_3)_n$ plotted as a function of n; (a) 3^2S—^1S [●] and (b) 3^2P—^{1}S [○] transitions. VDEs of the geometrical isomers are also plotted [□, ◇].

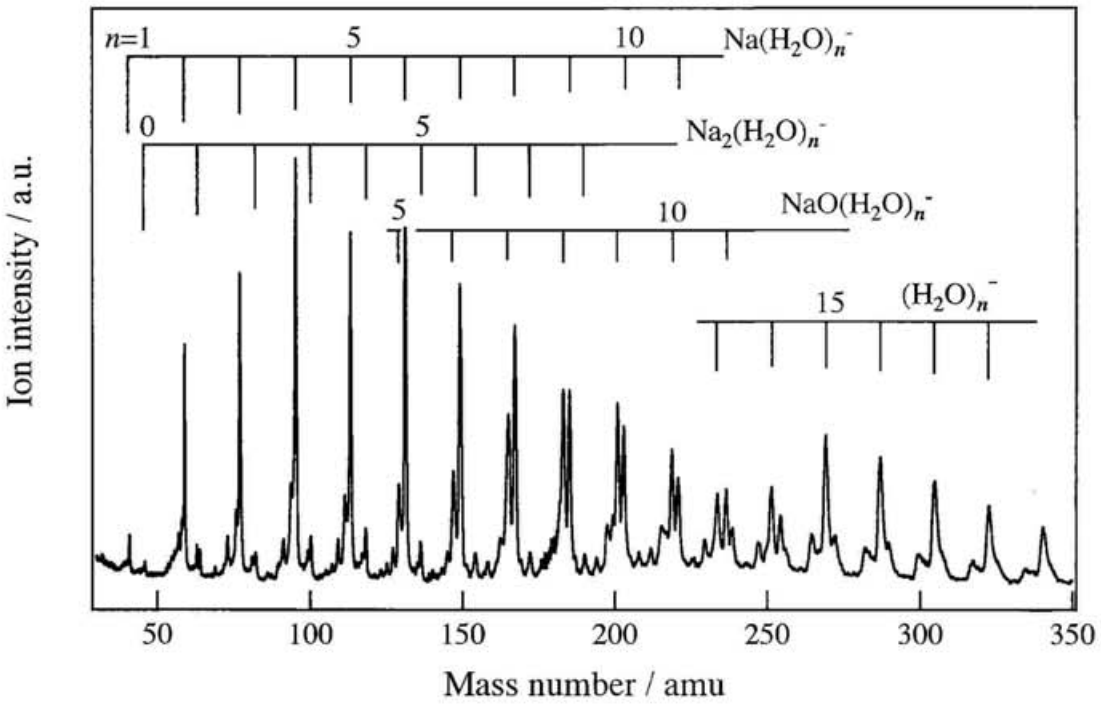

Figure III-11. Typical TOF mass spectrum of Na^--water clusters. NaO $(H_2O)_n^-$ and $(H_2O)_n^-$ are also observed in the higher mass region.

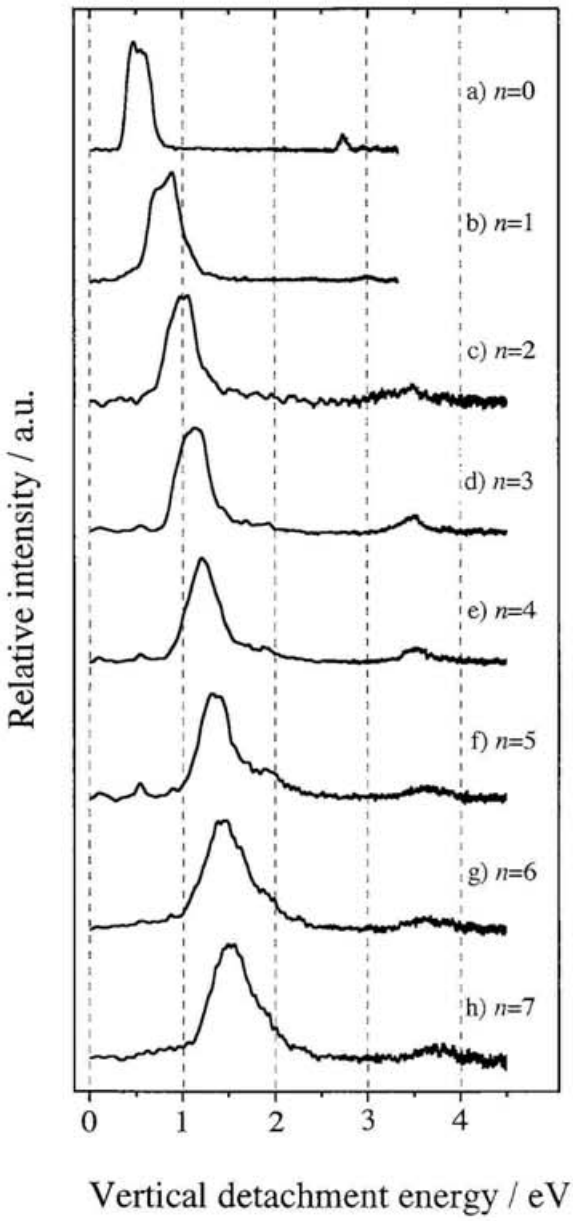

Figure III-12. Photoelectron spectra of $Na(H_2O)_n^-$ ($n \leq 7$), collected using the phtodetachment energies of 3.49 eV (355 nm) for $n \leq 1$ and 4.66 eV (266 nm for $n \geq 2$. The spectra are normalized at the peak of 3 $^2S—^1S$ transition.

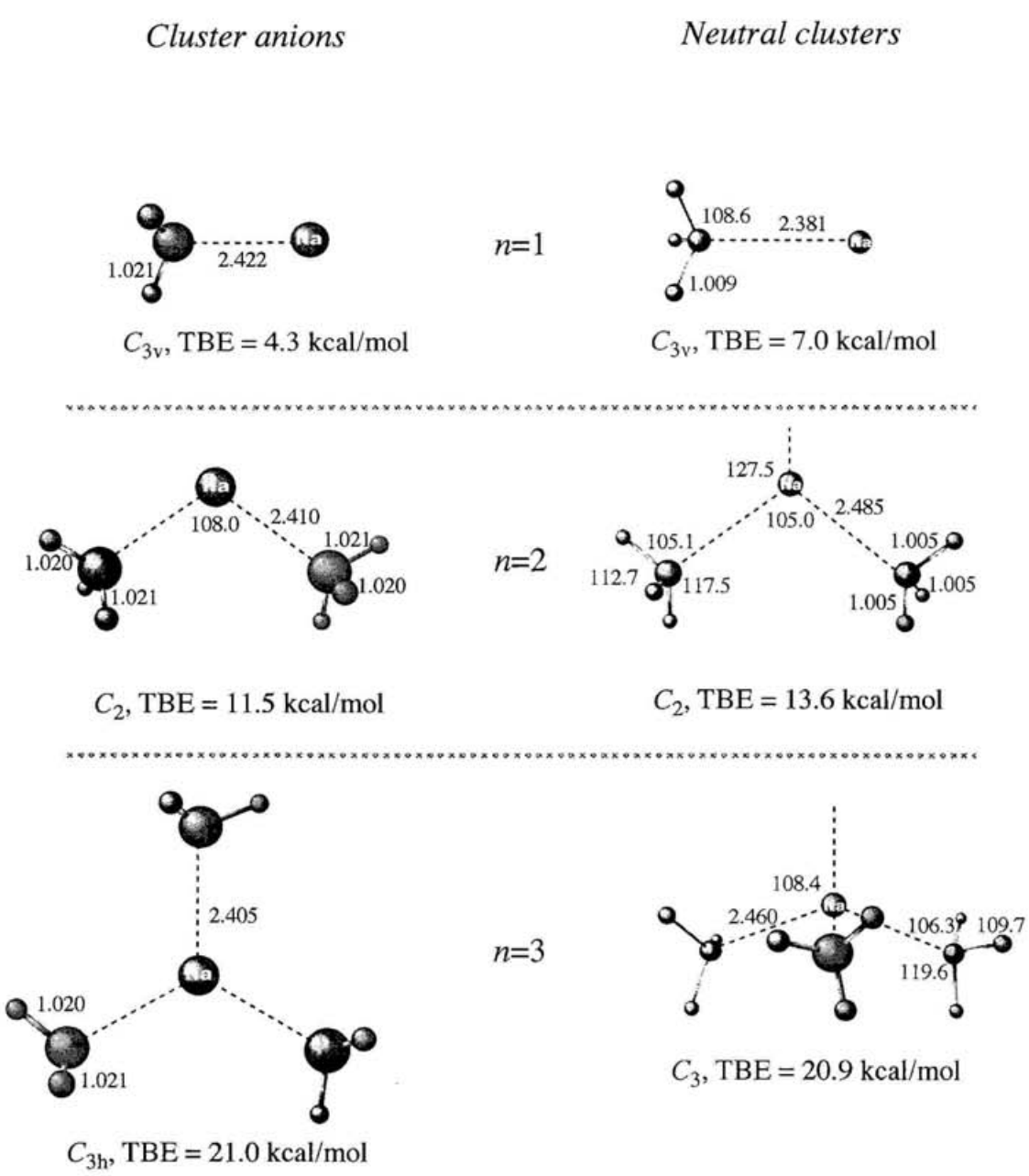

Figure III-13. The optimized geometries and total binding energies (TBEs) with ZPC of ammoniated sodium clusters. (*left column*) The geometries of anion clusters at MP2 level [27]. (*right column*) The geometries of neutral clusters at the HF/6-31+G(d) level [20]. Geometrical parameters are given in Å and degrees.

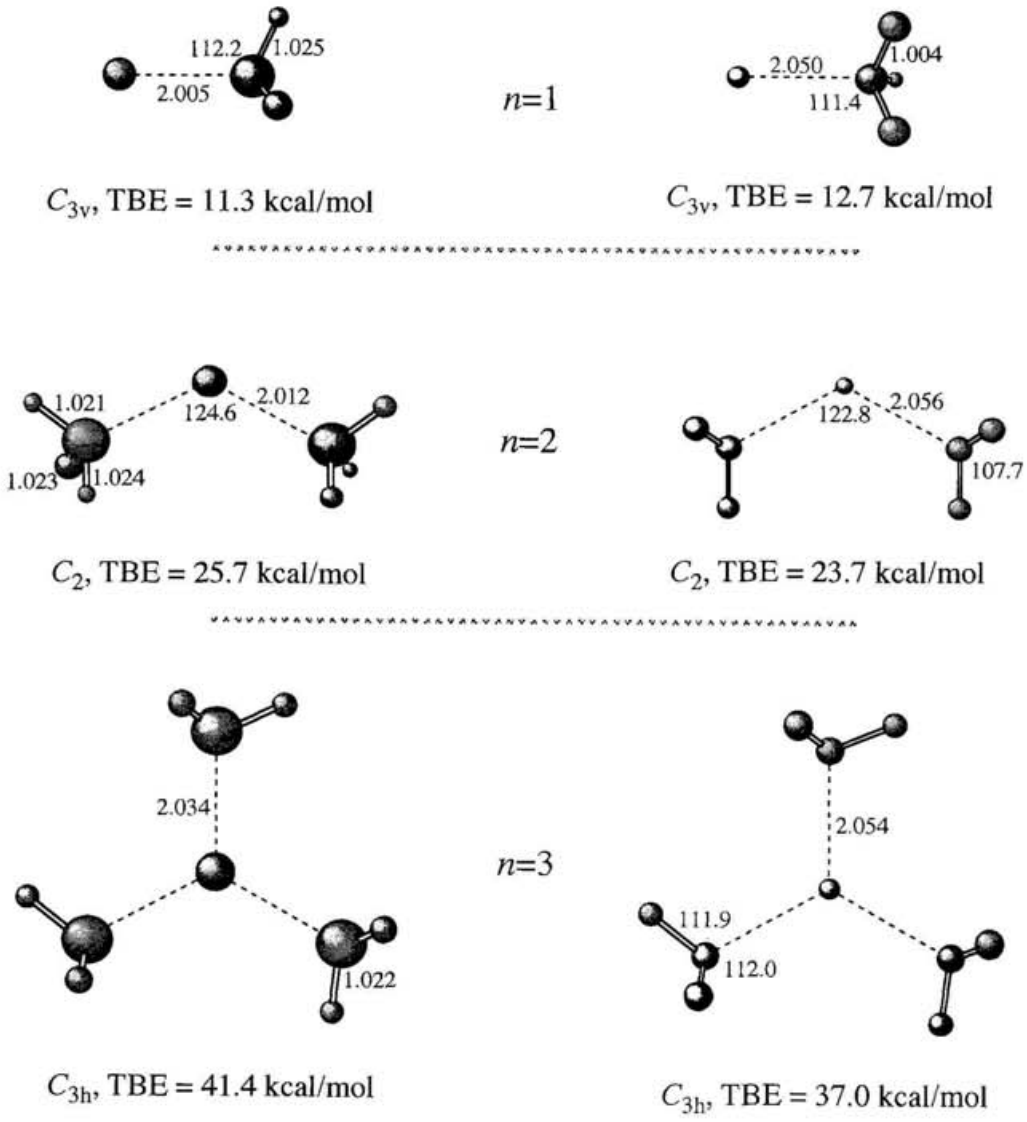

Figure III-14. The optimized geometries and total binding energies (TBEs) with ZPC of ammoniated lithium clusters. (*left column*) The geometries of anion clusters at MP2 level with the 6-311++G(d,p) basis set [27]. (*right column*) The geometries of neutral clusters at the HF/6-31++G(d,p) level [28]. Geometrical parameters are given in Å and degrees.

a)

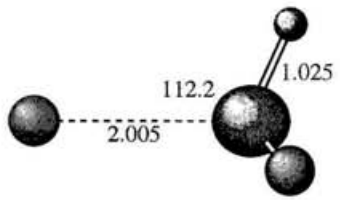

C_{3v}, TBE = 11.2 kcal/mol

b)

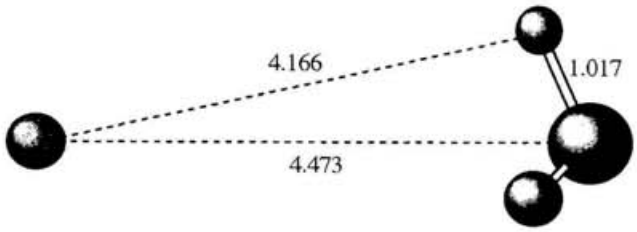

C_{3v}, TBE = 3.1 kcal/mol

Figure III-15. The optimized geometries and total binding energies (TBEs) with ZPC of a) type-I and b) type-II isomers of $Li(NH_3)_1^-$ at MP2 level [28]. Geometrical parameters are given in Å and degrees.

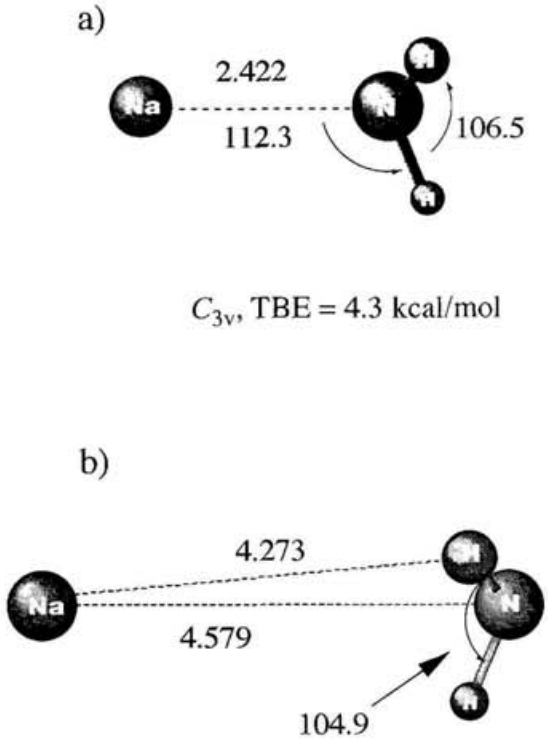

Figure III-16. The optimized geometries of a) type-I and b) type-II isomers of $Na(NH_3)_1^-$ at MP2 level [35]. Geometrical parameters are given in Å and degrees.

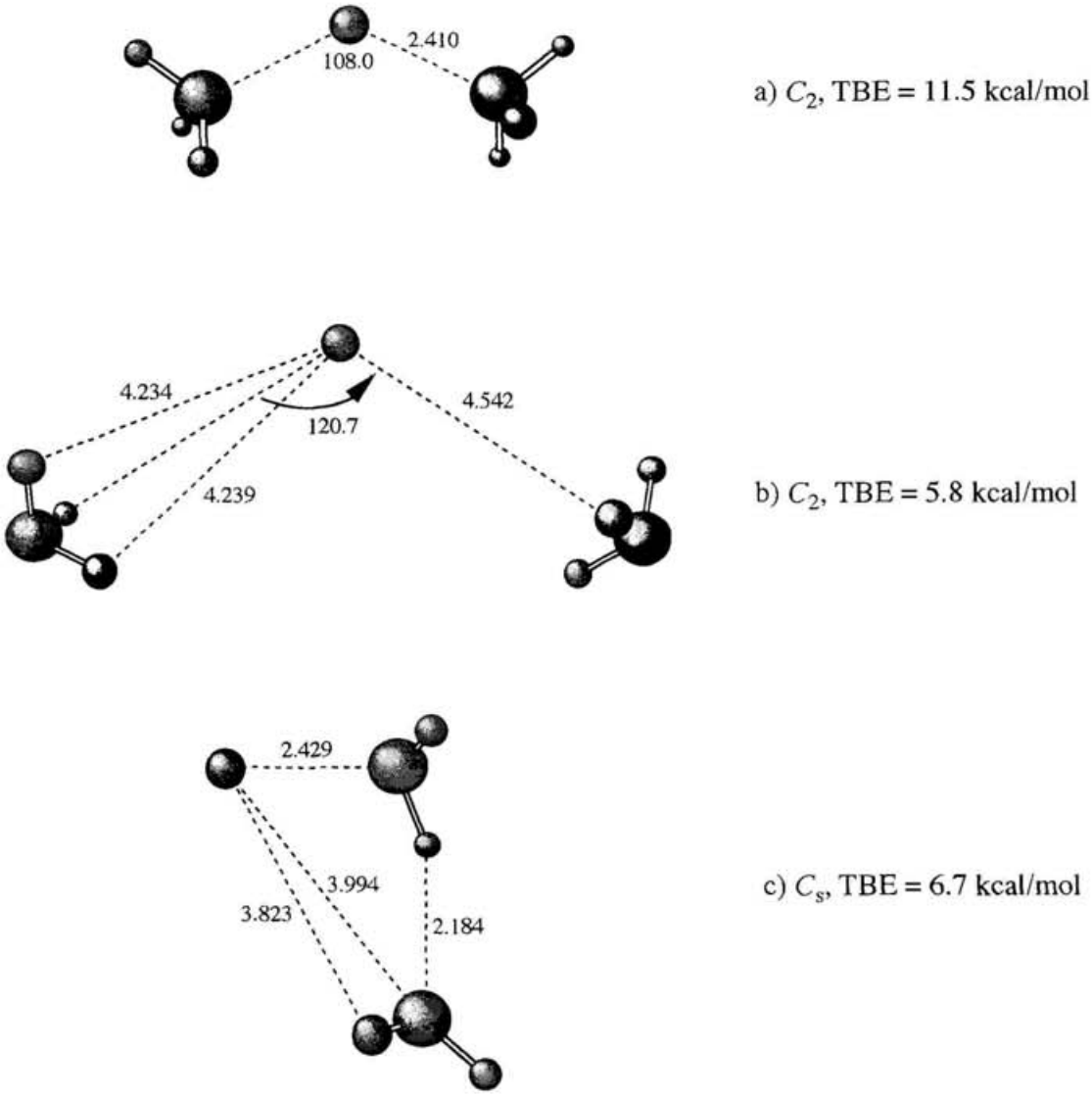

Figure III-17. The optimized geometries and the total binding energies (TBEs) of the a) type-I, b) type-II and c) type-III isomers of $Li(NH_3)_2^-$ at MP2 level [35]. Geometrical parameters are given in Å and degrees.

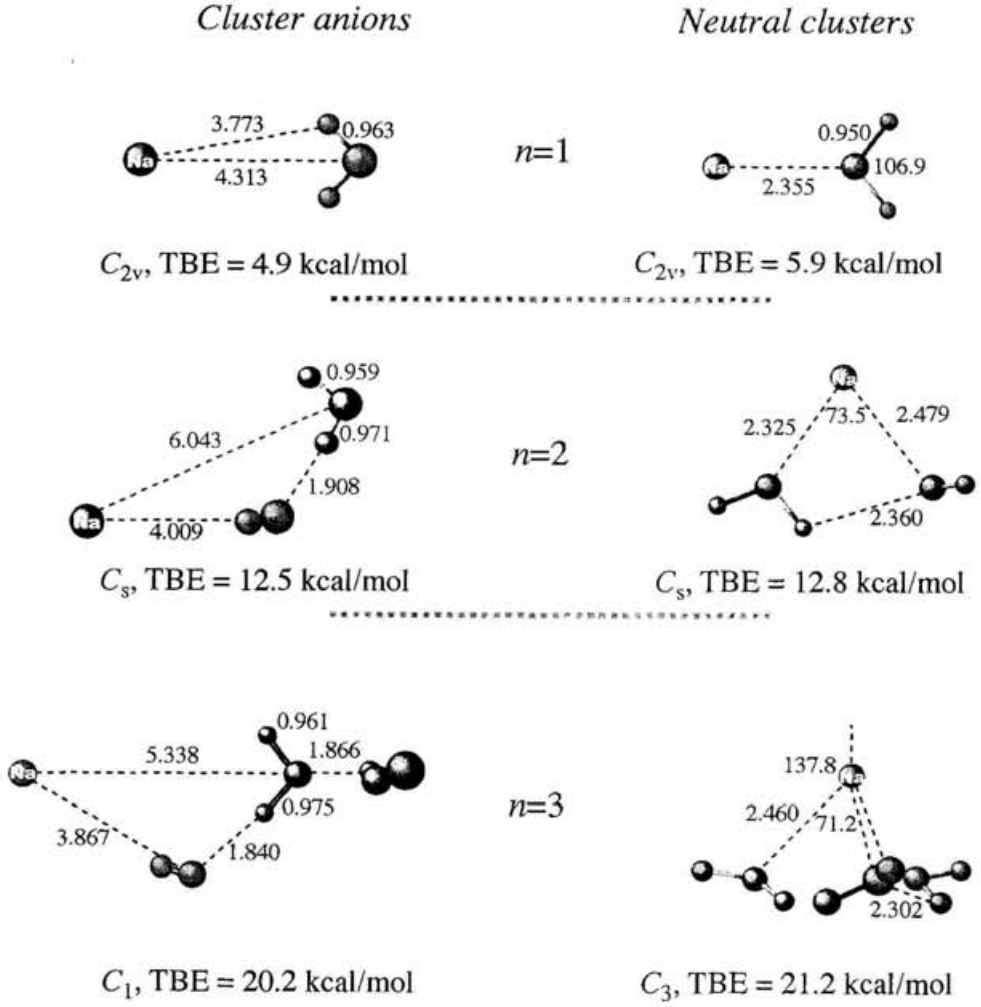

Figure III-18. The optimized geometries and total binding energies (TBEs) of hydrated sodium clusters. (*left column*) Geometries of $Na(H_2O)_n^-$ (n=1-3) at MP2 level [27]. (*right column*) Geometries of $Na(H_2O)_n$ (n=1-3) at the HF/6-31 +G(d) level [19]. Geometrical parameters are given in Å and degrees.

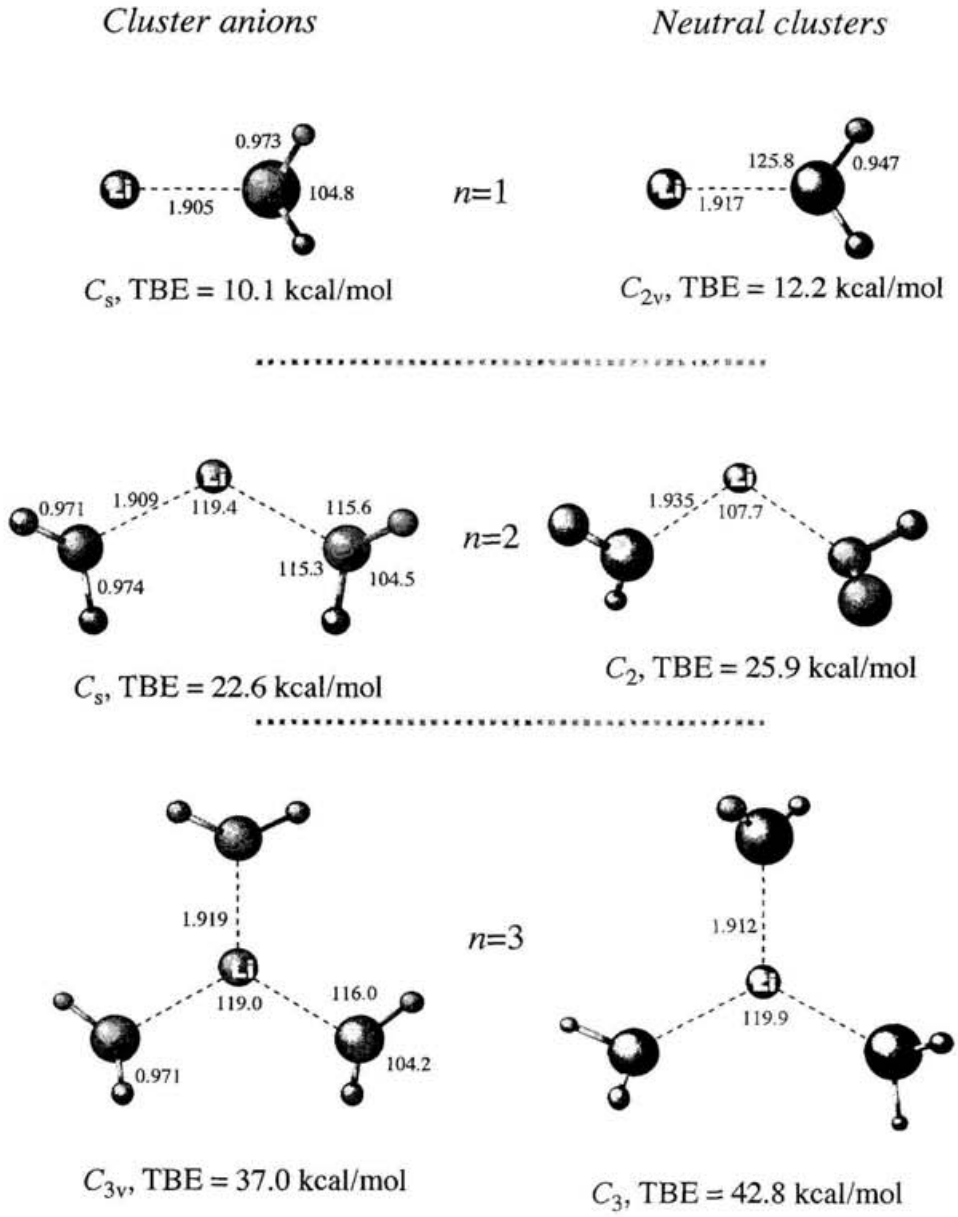

Figure III-19. The optimized geometries and the total binding energies (TBEs) of the $Li(H_2O)_n^-$ (left column, n=0-3 by MP2 method with all 1*s* orbitals frozen [27]) and $Li(H_2O)_n$ (right column, n=0-3 at MP2 level with 6-311++G(d, p) and 6-31++G(d,p) basis sets as well as HF/6-31++G(d,p) level [34]) with ZPC. Geometrical parameters are given in Å and degrees.

Chapter IV
Microscopic solvation process of sodium dimer in clusters; photoelectron spectroscopy of $Na_2(NH_3)_n^-$

1. Introduction

Solvated electrons have been studied for more than one century since the first observation by Weyl in 1886. Recent advance in ultrafast laser spectroscopy has renewed efforts to unveil the relaxation process of electrons in polar solvent. Although many efforts have been paid to clarify the structure and localization mode of solvated electron, its intrinsic properties are still the subject of intensive discussion. Besides these studies, a new approach such as the study of solvated electrons in finite clusters has been started recently to reveal the microscopic aspect of the solvation state of electrons. Negatively charged water and ammonia clusters, $(H_2O)^-_n$ and $(NH_3)^-_n$, have been prepared *via* capture of low-energy electrons by solvent clusters [4-7]. The photoelectron spectroscopy has been conducted for these clusters; n up to $\approx$70 for $(H_2O)^-_n$ and 1100 for $(NH_3)^-_n$, respectively [6,7]. The excess electron states have also been examined using quantum path integral molecular dynamics simulations [8,9]. On the other hand, the solvated electron has been studied in dilute alkali metal solution, and thus solvent clusters containing an alkali atom may serve as a good model for linking the macroscopic with microscopic properties of alkali metal-solvent systems. In small clusters, the interaction between the metal atom and solvent molecules may be a covalent-like, while

the valence electron of alkali metal atom may be transferred to a solvent cluster with sufficiently large n, and the ground state may have an ion-pair character as expected from the bulk solvated electron formation. The electron-photoejection threshold as a function of n is expected to include size-dependent information on the above transition, and also, on the excess electron state in clusters. From this point of view, recently, Hertel's group and Fuke's group have investigated the ionization potentials of ammonia and water clusters containing alkali metal atoms such as Na [10] and Cs [11]. In Chapter III, I demonstrate the results of ionization potential measurements of $Li(NH_3)_n$ and $Li(H_2O)_n$ as well as the photoelectron spectroscopy of $Li(NH_3)_n^-$, $Na(NH_3)_n^-$ and $Na(H_2O)_n^-$ produced by a laser vaporization technique coupled with a supersonic expansion method. These results clearly exhibit the early stage of the spontaneous ionization of alkali-metal atom in ammonia clusters to form the one-center (Rydberg-like) ion-pair-state, which is the counterpart of solvated electron in finite clusters.

In this chapter, I investigate the solvation process of sodium dimer in small ammonia clusters. In contrast to the Na atom, dimer may have much larger polarization effect, and thus, its interaction with the solvent molecules is expected to change substantially. And also, since the symmetry of solute decreases from spherical, it is interesting to know whether the solvation structure is symmetrical or not. To clarify the solvation state of Na_2 in $(NH_3)_n$, I carry out the photoelectron spectroscopy of $Na_2^-(NH_3)_n$ ($n \leq 8$). The spectra are found to exhibit a drastic decrease in the vertical detachment energy for the transitions to the neutral excited states, except for that of the first excited state derived from $Na_2(a^3\Sigma_u^+)$. In co-operation with the *ab initio* calculations, the experimental results will be discussed in relation with the localization mode of the valence electron on Na_2 in ammonia clusters.

2. Experimental

Details of the experimental apparatus for photoelectron spectroscopy used in this work have been described in Chapter II. The Na sample is purchased from Rare Metallic Co. Ltd. (99.9 % purity) and re-formed prior to use to fit with the nozzle beam source. The neat ammonia gas is used as a carrier gas. The ammonia (NH_3, minimum purity of 99.99 %, Nippon Sanso) is used without further purification.

3. Results and discussion

In the TOF mass spectrum of negative ions of sodium-ammonia system, cluster ions, $Na_2(NH_3)_n^-$ and $Na_3(NH_3)_n^-$, are observed up to n=10 and n=6, respectively, in addition to the cluster ions containing Na^-. The abundance of these ions varies with the fluence of vaporization laser and also the delay time between the pulsed-valve and vaporization laser. I carefully optimize the experimental parameters to enhance the abundance of cluster ions containing Na_2^- in the beam.

Figure IV-1 shows the photoelectron spectra of $Na_2^-(NH_3)_n$ (n=0-8). Na_2^- exhibits three bands at the vertical detachment energies of 0.48, 1.36, and 2.32 eV, respectively. This result is almost the same as that reported by Bowen and coworkers [31]. The spectrum has been analyzed theoretically by Bonacic-Koutecky and coworkers using an *ab initio* method [32,33]. According to their calculations, the above bands are assigned to the transitions from the ground state of anion ($X^{-2}\Sigma_u$) to the neutral ground ($X^1\Sigma_g^+$) and excited states ($a^3\Sigma_u^+$, $A^1\Sigma_u^+$, $b^3\Pi_u$), respectively. Since the anion has a excess electron in its antibonding orbital in addition to corresponding neutral state, the bond length of the Na_2^- is expected to be longer than Na_2. Recently, Hashimoto and

Kamimoto (HK) have carried out *ab initio* calculations for $Na_2(NH_3)_n^-$ (n=0-3) [34]. The optimized structures are represented in Figure IV-3. The calculations predict the bond length of Na_2^- as 0.362_9 nm, this value is 0.055_1 nm longer than measured for Na_2 (0.307_8 nm). This result supports the expectation above. In Figure IV-2, potential curves of Na_2 reported by Jeung [35] are shown. As shown in this figure, the $A^1\Sigma_u^+$ and $b^3\Pi_u$ states are nearly degenerate in the anion geometry. Thus, the band at 2.32 eV is supposed to be assignable to the transitions to these two states. The HK's calculations also predict the VDEs of the *X*, *a*, *A* and *b* states of Na_2 as 0.53, 1.25, 2.14 and 2.10 eV, respectively, and reproduce the photoelectron spectrum fairy well.

$Na_2^-(NH_3)$ exhibits four bands at the VDEs of 0.39, 1.29, 2.10, and 2.38 eV as shown in Figure IV-1b. The former two bands can be assigned to the transitions derived from the $X^1\Sigma_g^+ - X^{-2}\Sigma_u$ and $a^3\Sigma_u^+ - X^{-2}\Sigma_u$ transitions of Na_2^-. These bands are shifted by 0.09 and 0.07 eV to the lower VDE upon complex formation. On the other hand, the bands at 2.10 and 2.38 eV may be ascribed to the transitions such as $b^3\Pi_u - X^{-2}\Sigma_u$ and $A^1\Sigma_u - X^{-2}\Sigma_u$ respectively, which are nearly-degenerate for Na_2^- as mentioned above. As shown in Figure IV-3b, $Na_2(NH_3)^-$ has C_{3v} geometry, in which ammonia molecule is bound linearly to Na_2 *via* the N atom; the Na—N bond length is estimated to be 0.242_8 nm, while that of sodium dimer is 0.340_6 being shorter than the dimer itself by 0.022_3. With this configuration, a simple symmetry consideration leads to the prediction that the $A^1\Sigma_u^+$ state is destabilized significantly by the complex formation comparing with the $b^3\Pi_u$ state, because of the larger repulsive interaction in the $A^1\Sigma_u^+$ state between the σ_u orbital of Na_2 and the nonbonding orbital of NH_3. In accord with this expectation, the calculations gives the VDE separation between the $b^3\Pi_u$- and $A^1\Sigma_u^+$-type states as 0.35 eV in the anion geometry mentioned above. They have also located the higher excited states such as the $^3\Sigma_g^+$ and $B^1\Pi_u$ at 1.99 and 2.18 eV, respectively, above the $a^3\Sigma_u^+$-type state. As shown in Figure IV-1b, the PES band due to the transition to

the neutral ground state has much wider band width than sodium dimer itself. The broad-band feature may suggest the existence of geometrical isomer in the anion state. In fact, I observe two isomers for the $Na(NH_3)^-$ complex such as those with the Na—N and Na—H interactions. However, the theoretical results on the latter isomer are not available at present, and thus, it is difficult to discuss further on the broad feature of this transition.

Figure IV-1c shows the photoelectron spectrum of $Na(NH_3)_2^-$ exhibiting the four distinct bands at 0.46, 1.37, 1.89, and 2.16 eV. The VDEs of the former two bands, derived from the $X^1\Sigma_g^+ — X^{-2}\Sigma_u$ and $a^3\Sigma_u^+ — X^{-2}\Sigma_u$ transitions of Na_2^-, increase by *ca.* 0.07 and 0.08 eV respectively, with the addition of second ammonia molecule. On the other hand, the transitions to the $b^3\Pi_u$- and $A^1\Sigma_u^+$-type states are shifted by more than 0.2 eV to the lower VDE. HK have also calculated the structure and the energy levels of the excited states for $Na_2(NH_3)_2^-$. They have predicted that $Na_2(NH_3)_2^-$ has the structure, in which the second ammonia molecule is bound to the same Na atom as the first one with C_2 symmetry as shown in Figure IV-3c. In the C_2 configuration, the degeneracy of the $b^3\Pi_u$ state is also expected to be removed. However, the amount of splitting calculated by HK is *ca.* 0.05 eV being consistent with the relatively sharp band width of the corresponding transition at 1.89 eV.

As shown in Figure IV-3d, $Na_2(NH_3)_3^-$ has the C_3 structure, in which the third ammonia molecule is also bound to the same Na atom as in the case of n=2 through the N atom. This structure may enhance further the polarization of sodium dimer as discussed later. The PES of n=3 as shown in Figure IV-1d exhibits the further decrease in the VDEs of the $b^3\Pi_u$ and $A^1\Sigma_u$, and probably the higher excited state of Na_2 such as the $B^1\Pi_u$ and $c^3\Sigma_u^+$ as well. The other feature of PES is no appreciable change in the VDEs of the $X^1\Sigma_g^+$- and $a^3\Sigma_u^+$-type transitions. As seen in Figures IV-1g-i, the photoelectron bands for the higher excited states almost superimposed on that of the $a^3\Sigma_u^+$-type state. In addition to these features, the spectral intensity at the valley between the bands

corresponding to the neutral ground and first excited states increases with addition of ammonia molecules from n=4 to 8. On closer inspection of the spectrum of n=8, it turn out to be the another transition (*ca.* 1.0 eV), which may correspond to the higher excited states shifted by solvation. Thus, for the larger clusters, both the $b^3\Pi_u$- and $A^1\Sigma_u$-type states may become degenerate with the $a^3\Sigma_u^+$- and $X^1\Sigma_g^+$-type states independently. Interestingly, the $a^3\Sigma_u^+$-type transition start to shift to the higher VDE for $n\geq4$ and is shifted by more than 0.2 eV for n=8 with respect to that of Na_2. Although the theoretical results on the structures for $n\geq4$ are not available, the latter results may indicate that the additional ammonia molecules are bound to the second sodium atoms *via* the N atom for $n\geq5$.

In Chapter III, I have examined the photoelectron spectra of the Na^-- and Li^--ammonia clusters. As for $Na(NH_3)_n^-$, the 3^2P-type transition shifts further to the lower VDE for n=4, and then shifts with much slower rate for $n\geq5$ (the amount of shift of n=5 is more than 1.4 eV with respect to that of Na^-). The rapid change in the rate of shift between n=4 and 5 is ascribed to the formation of solvation shell about Na^-. For $Li(NH_3)_n^-$, the 2^2P-type transition also shifts to the lower VDE as large as 1.4 eV and are almost degenerate into the transition to the neutral ground state for $n\geq10$. In addition to these observations, I have also found the slight red-shift of the ^2S-type band in both systems indicating the larger binding energy of the neutral clusters than that of the cluster anions. These results have been analyzed by *ab initio* calculations by Hashimoto and explained in terms of the delocalization of the singly-occupied molecular orbital (SOMO) originated from the metal valence orbital. For $n\geq3$, the SOMO density of $Li(NH_3)_n^-$ and $Na(NH_3)_n^-$ is predicted to extend in space on and between the ammonia molecules rather than on the metal atom because of the strong metal atom—N interaction. In other words, the alkali-atom is spontaneously ionized in rather small ammonia clusters to form the

one-center (Rydberg-like) ion-pair state, which is the counterpart of solvated electron in finite clusters.

Based on the above results for the metal atom-ammonia clusters, the observed spectral features of $Na_2(NH_3)_n^-$ can be interpreted as follows. As mentioned previously, the *ab initio* calculations by HK suggest that ammonia molecules are bound selectively to one of the sodium atom *via* N atom in the most stable anion clusters up to $n\approx4$. These structure may induce the delocalization of SOMO on the solvated Na atom. And also, the second Na atom in dimer may enhance the ionic character of the relevant Na atom. The rapid decrease in VDEs of the higher exited states shown in Figures IV-1b-e, as well as no appreciable change in VDE of neutral ground state, seems to support these arguments and indicate the formation of ion-pair state as in the case of Na atom. Moreover, Figure IV-1 displays that the $a^3\Sigma_u^+$-type transition starts to shift to higher VDE for $n\geq4$, though the energy separation between the neutral ground and $a^3\Sigma_u^+$-type state is almost unchanged for $n\leq4$. Although the theoretical results on the structures for $n\geq5$ are not available, the latter results may indicate the ligation of additional ammonia molecules to the other sodium atom in dimer to form the second ion-pair site. Needless to say, the energy separation between the $X^1\Sigma_g^+$ and $a^3\Sigma_u^+$ state of Na_2 is determined by the exchange interaction between the two 3*s* electrons on sodium atoms within the first approximation. Thus the energy separations of clusters include information on the diffuse 3*s* orbitals of Na_2 being dissolved in small ammonia clusters. This information is very important to unveil the early stage of solvated electron formation in bulk metal-ammonia system, however, it is premature to discuss further on the trend in the above energy separation without the results of theoretical analysis.

In conclusion, I have demonstrated the usefulness of photoelectron spectroscopy of solvated alkali metal dimer anion in the investigation of the early stage of solvated-electron formation in clusters. Extension of these

experiments to higher cluster size for both the metal atom and solvent molecules is now in progress.

References for Chapter IV

[1] Dogonadze, R. R.; Kalman, E.; Kornyshev, A. A.; J. Ulstrup, J. eds., *The Chemical Physics of Solvation, Part C* (Elsevier, Amsterdam, 1988).

[2] Tuttle, Jr., T. R.; Golden, S. *J. Phys. Chem.* **1991**, *95*, 5725.

[3] Alfano, J.C.; Walhout, P. K.; Kimura, Y.; Barbara, P. F. *J. Chem. Phys.* **1993**, *98*, 5996.

[4] Haberland, H.; Schindler, H. -G.; Worksnop, D. R. *Ber. Bunsenges. Phys. Chem.* **1984**, *88*, 270.

[5] Haberland, H.; Ludewigt, C.; Schindler, H. -G.; Worksnop, D. R. *Surface Sci.* **1985**, *156*, 157.

[6] Coe, J. V.; Lee, G. H.; Eaton, J. G.; Sarkas, H. W.; Bowen, K. H.; C. Ludewigt, C.; Haberland, H.; Worsnop, D. R. *J. Chem. Phys.* **1990**, *92*, 3980.

[7] Lee, G. H.; Arnold, S. T.; Eaton, J. G.; Sarkas, H. W.; Bowen, K. H.; Ludewigt, C.; Haberland, H. *Z. Phys.* **1991**, *D20*, 9.

[8] Barnett, R. N.; Landman, U.; Cleveland, C. L.; Jortner, J. *Chem. Phys. Lett.* **1988**, *145*, 382.

[9] Barnett, R. N.; Landman, U.; Cleveland, C. L.; Kestner N. R.; Jortner, J. *Chem. Phys. Lett.* **1988**, *148*, 249.

[10] Hertel, I. V.; Hüglin, C.; Nitsch, C.; Schulz, C. P. *Phys. Rev. Lett.* **1991**, *67*, 1767.

[11] Misaizu, F.; Tsukamoto, K.; Sanekata, M.; Fuke, K. *Chem. Phys. Lett.* **1992**, *188*, 241.

[12] Martyna, G. J.; Klein, M. L.; *J. Phys. Chem.* **1991**, *95*, 515.

[13] Barnett, R. N.; Landman, U. *Phys. Rev. Lett.* **1993**, *70*, 1775.

[14] Stampfli, P.; Bennemann, K. H. *Comput. Matter. Sci.* **1994**, *2*, 578.

[15] Hashimoto, K.; He, S.; Morokuma, K. *Chem. Phys. Lett.* **1993**, *206*, 297.

[16] Hashimoto, K.; Morokuma, K. *Chem. Phys. Lett.* **1994**, *223*, 423.

[17] Hashimoto, K.; Morokuma, K. *J. Am. Chem. Soc.* **1994**, *116*, 11436.

[18] Hashimoto, K.; Morokuma, K. *J. Am. Chem. Soc.* **1995**, *117*, 4151.

[19] Misaizu, F.; Sanekata, M.; Tsukamoto, K.; Fuke, K.; Iwata, S. *J. Phys. Chem.* **1992**, *96*, 8259.

[20] Misaizu, F.; Tsukamoto, K.; Sanekata, M.; Fuke, K. *Laser Chem.* **1995**, *15*, 195.

[21] Schultz, C. P.; Haugstätter, R.; Tittes, H. -L.; Hertel, I. V. *Z. Phys.* **1988**, *D10*, 279.

[22] Lepoutre, G.; Jortner, J. *J. Phys. Chem.* **1972**, *76*, 683.

[23] Schindewolf, U. *J. Phys. Chem.* **1984**, *88*, 3820.

[24] Takasu, R.; Misaizu, F.; Hashimoto, K.; Fuke, K. *J. Phys.Chem.* **1997**, *A101*, 3078.

[25] Marchi, M.; Sprik, N.; Klein, M. L. *Faraday Discuss. Chem. Soc.* **1988**, *85*, 373.

[26] Hashimoto, K.; Kamimoto, T. to be submitted.

[27] Zhan, C. -G.; Iwata, S. *Chem. Phys. Lett.* **1995**, *232*, 72.

[28] Markovich, G.; Giniger, R.; Levin, M.; Cheshnovsky, O. *J. Chem. Phys.* **1991**, *95*, 9416.

[29] Arnold, D. W.; Bradforth, S. E.; Kim, E. H.; Neumark, D. M. *J. Chem. Phys.* **1995**, *102*, 3510.

[30] Takasu, R.; Hashimoto, K.; Fuke, K. *Chem. Phys. Lett.* **1996**, *258*, 94.

[31] McHugh, K. M.; Eaton, J. G.; Lee, G. H.; Sarkas, H.W.; Kidder, J. T.; Snodgrass, J. T.; Manaa, M. R.; Bowen, K. H. *J. Chem. Phys.* **1989**, *91*, 3892.

[32] Bonacic-Koutecky, V.; Fantucci, P.; Koutecky, J. *J. Chem. Phys.* **1989**, *91*, 3794.

[33] Bonacic-Koutecky, V.; Fantucci, P.; Koutecky, J. *J. Chem. Phys.* **1990**, *93*, 3802.
[34] Hasimoto, K.; Kamimoto, T. private communication.
[35] Jeung, G. *J. Phys.* **1983**, *B16*, 4289.

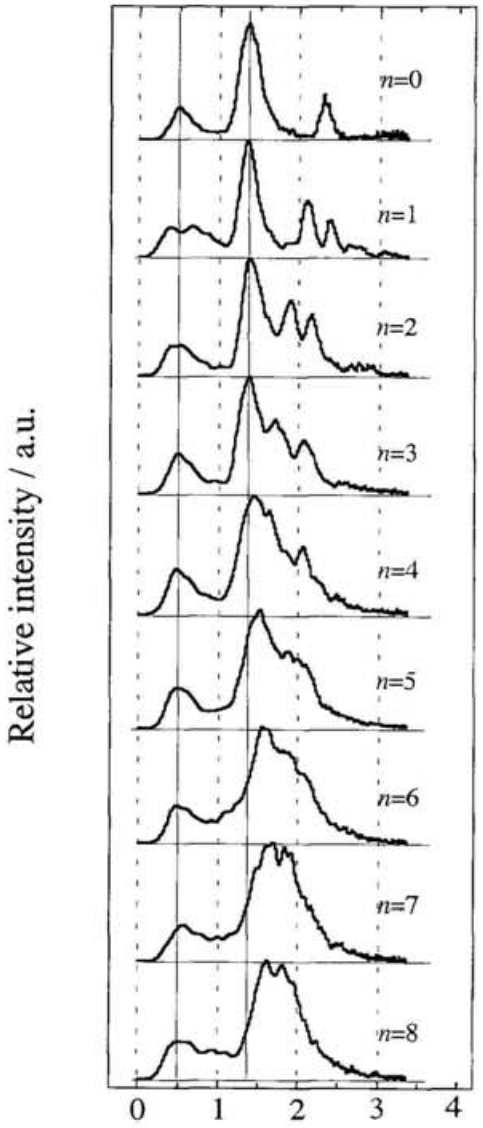

Figure IV-1. Photoelectron spectra of $Na_2(NH_3)_n^-$ ($n \leq 8$) collected using a photodetachment energy of 3.49eV (355 nm). The spectra are normalized at the peak corresponds to the transition from the $X^{-2}\Sigma_u$ state of anion to the $a^3\Sigma_u^+$ state of neutral Na_2.

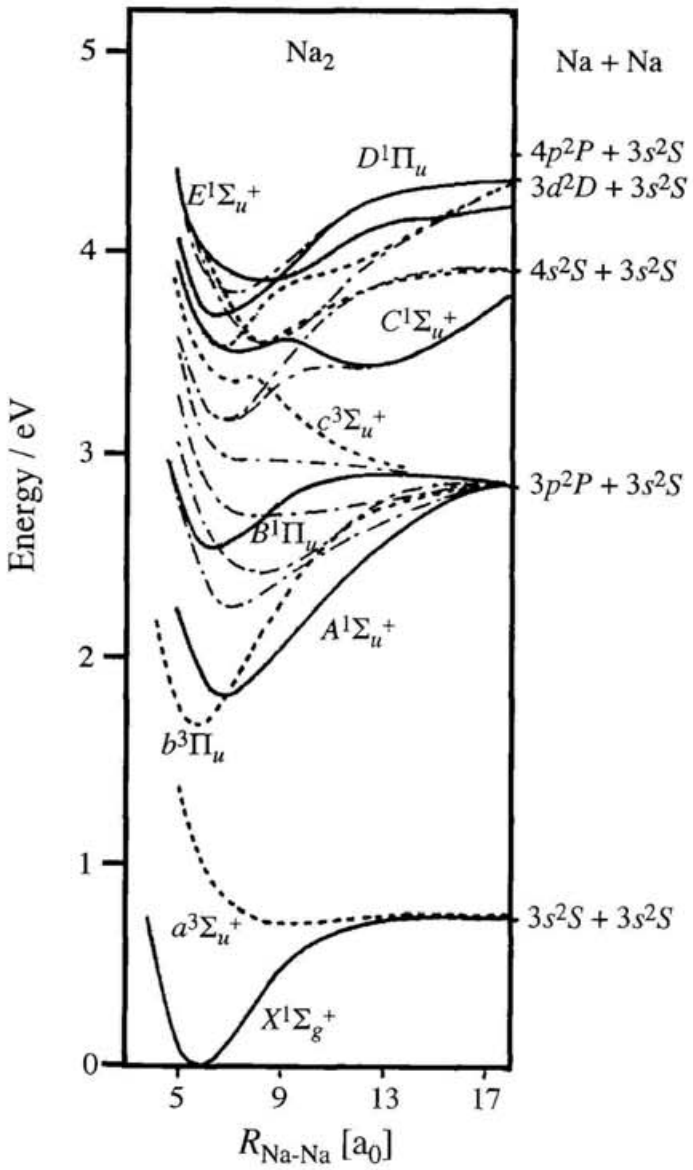

Figure IV-2. Potential energy curves of Na_2 obtained by theoretical calculation [35].

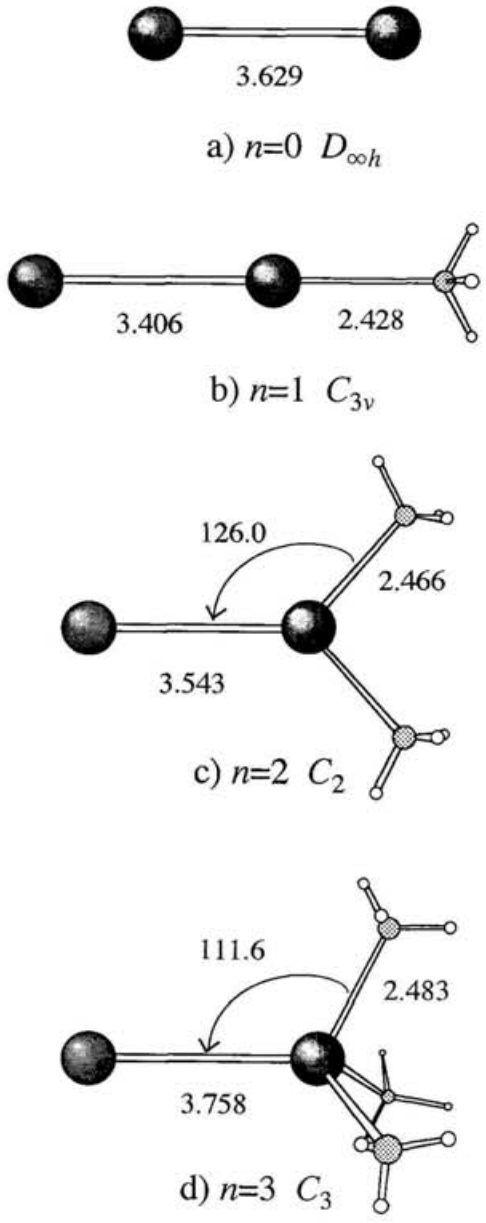

Figure IV-3. Optimized structures of $Na_2(NH_3)_n^-$ (n=0-3) at CASSCF level with the extended basis set [34].

Chapter V: Section 1
Formation process of NH_4 radical in ammonia cluters

1. Introduction

Photoionization process of ammonia clusters has been one of the central issues in cluster research for the last two decades [1]. The ionization mechanism has been studied extensively using various ionization techniques including electron impact [2,3], single-photon [4-6] and multiphoton ionization [7-10]. The protonated cluster ions, $(NH_3)_nH^+$, have been found to be produced dominantly by the former two processes. In these processes, the direct ionization of $(NH_3)_n$ generates $(NH_3)_n^+$, which are unstable, and are followed by the proton-transfer reaction to form $NH_4^+(NH_3)_{n-2}$ including a loss of NH_2. The latter reaction have also been studied in detail by *ab initio* calculations [11-13]. The resonance enhanced two-photon ionization (RE2PI) of clusters through the first singlet electronic state ($A\ ^1A_2''$) of ammonia molecule has also been examined. Kassab and coworkers have predicted theoretically the mechanism for the production of $NH_4^+(NH_3)_n$ through the ionization of $NH_4(NH_3)_n$ [1]. Since the A-state ammonia is predissociative ($NH_3 \rightarrow NH_2 + H$, lifetime < 200 fs) [14,15], $NH_4(NH_3)_n$ is expected to be formed efficiently through an intracluster reaction. This process may compete with the ionization of $(NH_3)_n^*$ by the second photon, which is followed by the reaction in the ionization state to produce the protonated cluster ions.

Recently, these two mechanisms to produce $NH_4^+(NH_3)_n$ have been confirmed experimentally using nanosecond [9,10] and femtosecond pump-probe techniques [16,17]. Although these studies have revealed the photoionization process of $(NH_3)_n$ *via* the *A* state, the understanding of the predissociation process seems to be still incomplete; only the process to produce $NH_4(NH_3)_m$ involving concomitant NH_2 loss is detected. These results raise an interesting question whether the cluster containing NH_2 radical is formed or not in the molecular beam after the photolysis. This issue seems to be quite important to fully understand the photochemistry of $(NH_3)_n$ on the *A*-state surface as well as the mechanism of RE2PI of $(NH_3)_n$.

As mentioned above, the clusters containing NH_4 radical is the key species in RE2PI of ammonia clusters. This radical has also been considered to be an important intermediate in solution chemistry. The possible existence of NH_4 radical in the reaction of the solvated electron and in electrochemistry has been speculated on for many years [18-21]. The spectroscopic properties of NH_4 have been studied extensively, since the first spectroscopic characterization by Herzberg [22,23]. According to these studies, NH_4 has a very shallow potential well in the ground state, and as a result, it has a short lifetime. Porter and coworkers have studied the stability of small $NH_4(NH_3)_n$ by a neutralized ion beam technique and found that the radical is stabilized extensively by the complex formation with ammonia [24-26]. Recently, the structure and stability of ammoniated NH_4 radical were also investigated theoretically by Kassab and coworkers [12,27]. As will be described in Chapter V-2, I also examine the ionization potentials of ammoniated NH_4 clusters in relation with an electron localization mode in the gas-phase clusters [28]. However, the experimental data on the physical and chemical properties of ammoniated NH_4 are still quite limited. The study on the stability of

these clusters as a function of the number of solvent molecules may provide us a clue to reveal the long standing problems in bulk solution.

In this work, I study the formation and decay processes of ammoniated NH_4 clusters produced by the photolysis of jet-cooled $(NH_3)_n$ using nano- and femtosecond pump-probe techniques. The pump-probe curves for $NH_4^+(NH_3)_n$, n=0-4, present multiple decay components corresponding to the predissociation of the A-state ammonia molecule and the solvation of NH_4 radical in clusters. As it has been reported previously, the unprotonated ammonia cluster ions, $(NH_3)_n^+$, are rarely observed except for n=1 and 2. The curve for $(NH_3)_2^+$ is found to exhibit a clear rising feature with a time constant of a few ps. This ion is formed by one-photon ionization of a new intermediate with an ionization threshold of 3.79 eV. From the comparison of these results and the theoretical predictions, I assign the intermediate as an excited-state NH_4^*-NH_2; a cage product of the intracluster reaction, and the final ionic state has a form of $NH_4^+NH_2$. I also examine the lifetime of $NH_4(NH_3)_n$, n=0-5. On the basis of these results, I will discuss on the predissociation process of ammonia clusters in the first excited state, and the formation and decomposition processes of the produced clusters containing NH_4 radical.

2. Experimental

The experimental apparatus used in this work consists of two groups; the reflectron-type TOF mass spectrometer and the femtosecond laser system. Details of the mass spectrometer have been described in Chapter II. The ammonia clusters are generated by supersonic expansion of pure ammonia (4 atm) from a pulsed nozzle. The ammonia (NH_3, minimum purity of 99.99 %, Nippon Sanso) is used without further

purification. Figure V-1 shows the setup for the femtosecond pump-probe experiment. Femtosecond laser pulses are generated by a Ti-sapphire laser (Spectra Physics/Tsunami). The output is amplified by a regenerative amplifier pumped by a 10 Hz Nd:YAG laser (Quanta-Ray/GCR-150). The output wavelength, pulse width, and energy are *ca.* 789 nm, 120 fs and 6 mJ/pulse, respectively. The pump pulses at near 197 nm are generated by phase-matched sequential conversion of the 789 nm pulse in three BBO crystals arranged in a nonlinear sum-frequency mixing scheme. The energy of the pump pulses is typically 2 μJ/pulse. The pulse duration of the pump pulses is measured by down-conversion with the pulse at the fundamental. As shown in Figure V-2, the cross-correlation trace at the signal wavelength of 263 nm gives a full width at half-maximum (FWHM) of about 360 fs. Assuming a sech^2 pulse, the deconvolution leads to a width of the pump pulse of 290 fs. The third harmonic at 263 nm (*ca.* 20 μJ/pulse) is used as the probe pulses. The pump and probe pulses are separated by a 45° reflecting mirror and the later pulses are sent through a delay stage. Thereafter, both pulses are recombined using another 45° high reflector. The laser beams are then introduced into the acceleration region of mass spectrometer without focusing, where they intersect the cluster beam. Cluster ions produced by two femtosecond pulses are accelerated and introduced to the field-free region of the reflectron TOF mass spectrometer. The mass spectra are measured at various delay times between the pump and probe pulses.

The lifetimes of $NH_4(NH_3)_n$ ($1 \leq n \leq 5$) are examined by pump-probe experiments with nanosecond lasers. An ArF excimer laser (Lambda Physik/COMPex) is used as the pump laser; the laser beam of *ca.* 100 μJ/pulse and 1-mm diameter is used without focusing. A far-field beam of a XeCl laser (Lambda Physik/LPX205) at 308 nm is used as the probe laser. In order to suppress the loss of the $NH_4(NH_3)_n$ clusters from the

ionization region, the probe beam with a large cross section (5 mm height and 15 mm width) and the ArF laser beam are introduced colinearly and counterpropagatedly to the acceleration region of the mass spectrometer. The lifetime is measured by detecting the ion signals as a function of delay time between the pump and probe pulses.

3. Results

Figure V-3 shows the typical TOF mass spectra of protonated, $NH_4^+(NH_3)_n$, and unprotonated, $(NH_3)_n^+$, ammonia cluster ions produced by two femtosecond laser photons with various delay times. The pump wavelength at 197 nm corresponds to the excitation of ammonia molecule to the ν_2'=5 bending vibrational level in the $A\ ^1A_2''$ state, while the probe pulse is at 263 nm. Since the ion signals are found to be easily saturated by the pump laser pulses (>10 μJ/pulse) alone, the laser intensity is attenuated to less than 5 μJ/pulse. Protonated ions are detected dominantly in the time region examined, while the unprotonated ions except for n=1 and 2, are weakly observed at the time when two pulses are temporally overlapped.

Figure V-4 shows the pump-probe curves for the small ammonia cluster ions through the A (ν'=5) state with a time step of 83 fs. These curves are obtained by averaging the results of several pump-prove experiments under the same conditions. The curve for NH_3^+ ion shown in Figure V-4a exhibits a sharp spike with a FWHM of 370 fs. The temporal profile is symmetrical with respect to the delay times between the pump and probe pulses; the base line is also at the same level for the both edges. The width of the spike is nearly the same as that for the cross correlation function of the pump and probe pulses; the NH_3^+ ion signals

give approximately a time-response function of the experimental system. Thus the zero of the time is defined at the peak of the NH_3^+ ion signals.

As seen in Figure V-4b, the peak of the NH_4^+ ion signals is delayed about 200 fs with respect to that for NH_3^+. The curve exhibits the fast and slow decay components; the features are much clearly seen in the pump-probe curve with a longer delay time as shown in Figure V-5b. The energy of the probe laser at 263 nm (4.71 eV) is well above the ionization energy of the excited-state ammonia clusters (*ca.* 3.9 eV [4]), and also it exceeds the ionization threshold of NH_4 radical (4.62 eV) [28]. Thus, these ions are considered to be formed through the photoionization of the excited-state ammonia clusters followed by the proton-transfer reaction [absorption-ionization-dissociation (AID) mechanism] as well as the photoionization of NH_4 produced by the intracluster reaction [absorption-dissociation-ionization (ADI) mechanism]. The pump-prove curve of $NH_4^+(NH_3)$ also shows the fast and slow decay components, however, the decay of the latter component is seen to be faster than that for NH_4^+. The pump-probe curves of $NH_4^+(NH_3)_n$ (n=2-4) also display two components as seen in Figure V-6. These results seem to indicate that the decay time for the slow component becomes longer with increasing n. Recently, the formation of $NH_4^+(NH_3)_n$ (n=1-4) through the A (v_2'=0-2) states was also examined by Castleman and coworkers [16,17] and the major features they reported are consistent with the present results. These observations suggest that the origin of the slow component of NH_4^+ is different from those for $n \geq 1$. According to the aforementioned spectroscopic studies [22,23], NH_4 decomposes with a lifetime of less than 100 ps [22,23]. Thus the slow decay component of NH_4^+ may be responsible for the decomposition process of NH_4. Assuming a single exponential decay, the lifetime of NH_4 is estimated to be 13±2 ps.

As seen in Figure V-3, unprotonated ions, $(NH_3)_n^+$, are also formed when the pump and probe pulses are temporally overlapped: the ion signals for $n>2$ decrease rapidly with increasing the delay time as in the case of NH_3^+. On the other hand, the unprotonated dimer ion shows an unique time response; the pump-probe curve of $(NH_3)_2^+$ consists of a rather weak spike and a rising curve as schematically shown by the dotted line in Figure V-5d. The former component may correspond to the ion signals due to the RE2PI process, while the latter component indicates the existence of an intermediate species which is one-photon-ionized by the 263 nm pulse to form $(NH_3)_2^+$. To get further information on the intermediate, I carry out the two-color photoionization experiments with nanosecond laser pulses. The fifth harmonic of a Nd:YAG laser at 212.8 nm, which corresponds to the *A* state ($v_2'=1$) of ammonia molecule, is used as the photolysis laser. On the other hand, the second harmonic of the excimer-pumped dye laser is used as the probe laser with zero delay time. Figure V-7 shows typical TOF mass spectra of small ammonia cluster ions produced at various probe laser wavelengths (329-314 nm, 3.77-3.95 eV). The ionization efficiency of $NH_4(NH_3)_n$ (n=2,3) dose not change appreciably in this wavelength range, while that of $NH_4^+(NH_3)$ exhibits a threshold behavior. These results are consistent with the study of Fuke and co-workers; the ionization thresholds of $NH_4(NH_3)_n$ (n=1-3) were determined to be 3.88, 3.31, and 2.97 eV, respectively [28]. On the other hand, the ionization efficiency of $(NH_3)_2^+$ decreases rapidly from 321 to 329 nm (3.86-3.77 eV) and gives the threshold energy of the intermediate as 3.79 eV.

In order to get further insight into the mechanism of stabilization of NH_4 in clusters, I also measure the lifetime of $NH_4(NH_3)_n$ using the pump-probe technique with nanosecond lasers. Since a long-lived photolysis products is drifted downstream with time in a molecular beam, it is

difficult to probe its concentration quantitatively using the probe beam with a small beam diameter. To suppress the loss of clusters in the ionization region, a top-flat laser beam with a large cross section is required. For this purpose, I use a far-field beam of XeCl excimer laser at 308 nm as the probe pulses; the width and height of the beam are *ca.* 15 and 5 mm, respectively. The uniformity of the laser fluence was examined by moving a power meter with a 0.5-mm-width slit across the cross section of the probe laser. The averaged fluctuation of the probe laser was estimated to be less than ±5 % as shown in Figure V-8. To correlate the width of the probe beam with time, I also measure a flight time of the photolysis product. The figures inserted in Figure V-8 show an experimental configuration and the velocity distribution of $NH_4(NH_3)_6$, which is expected to have a dissociation lifetime of >20 μs. In the velocity distribution measurements, the probe beam with a cross section of 1×5 mm is sent to the center of the acceleration region of the mass spectrometer, while the pump laser beam with a 1 mm diameter is introduced colinearly at 5 mm upstream with regard to the probe beam. The distribution is measured by detecting the ion signals as a function of the delay time between the pump and probe lasers. The average velocity of $NH_4(NH_3)_6$ in the molecular beam was estimated to be 1130 m/s: Thus the effective width of the probe beam (13 mm) corresponds to that of the time window of *ca.* 12 μs. Figure V-9 shows the pump-probe curves for $NH_4^+(NH_3)_n$ (n=1-3,5). With increasing the delay time, the clusters are ionized at the lower reaches of the stream in the acceleration region, and as a result, the resolution of mass spectrum changes significantly in the present time window. Therefore, the integrated intensity for each mass peak is plotted in Figure V-9 (open circles) as a function of delay time. As for n=1 and 2, the observed data are fitted reasonably in a single exponential function, from which the decomposition lifetimes are

determined to be 3±1 and 7±2 μs, respectively. On the other hand, the larger clusters have the lifetimes of longer than 10 μs and drift out from the present time window of the probe beam as shown in Figure V-9. These results as well as those for the femtosecond experiments clearly indicate that the lifetime of NH_4 is elongated more than 10^6 times in clusters.

4. Discussion

The photoionization of ammonia clusters has been known to produce the protonated cluster ions predominantly both in the one-photon ionization and RE2PI process *via* the first excited state [4-10]. As for the formation of these ions in the latter process, two mechanisms such as the AID,

$$(NH_3)_n + h\nu_1 \rightarrow (NH_3)_n^* + h\nu_2 \rightarrow (NH_3)_n^+ \rightarrow NH_4^+(NH_3)_{n-2} + NH_2 \qquad (1)$$

and ADI processes were proposed on the basis of the theoretical calculations [12,13]. The latter mechanism is considered to include the following dynamical processes.

$$(NH_3)_n + h\nu_1 \rightarrow (NH_3)_n^*(A) \qquad (2)$$

$$(NH_3)_n^*(A) \rightarrow (NH_3)_{n-2}\cdot NH_4^* \cdots NH_2 \qquad (3)$$

$$(NH_3)_{n-2}\cdot NH_4^* \cdots NH_2 \rightarrow (NH_3)_{n-2}\cdot NH_4 + NH_2 \qquad (4)$$

$$NH_4(NH_3)_{n-2} + h\nu_2 \rightarrow NH_4^+(NH_3)_{n-2} \qquad (5)$$

Here, $NH_4^*\cdots NH_2$ is an excited-state NH_4-NH_2 as discussed later. Process 3 corresponds to the predissociation of ammonia molecule to form the clusters containing $NH_4^*\cdots NH_2$, while the process 4 corresponds to the formation of NH_4 in clusters. The competing process between the AID and ADI mechanisms to form protonated ions in RE2PI are supported by the recent studies with nanosecond lasers [9,10]. More recently, Castleman and coworkers carried out femtosecond RE2PI experiments to reconfirm these two mechanisms [16,17]. The latter authors examined the formation process of $NH_4^+(NH_3)_n$ (n=1-4) *via* the v_2'=0-2 levels in the first excited state. In the present study, I reexamine the RE2PI process *via* the $A(v_2'=5)$ state to gain further insight into the photochemistry of ammonia clusters on the excited-state surface as well as the cluster-size dependence for the formation and decomposition processes of $NH_4(NH_3)_n$.

Predissociation of $(NH_3)_n$ (A) and formation of ammoniated NH_4

The mechanism of the photodissociation of ammonia following excitation to its first excited state has been studied extensively [14,15,30-32]. Before discussing the results on clusters, it is worth to summarize briefly the features for the photodissociation dynamics of ammonia molecule in the *A* state. In a free molecule, an energy barrier of *ca.* 0.4 eV along the predissociation coordinate was predicted theoretically [30]. Dissociation of NH_3 in the lower bending vibrational levels is considered to take place through a quantum mechanical tunneling of this barrier. The topology along this dissociation coordinate is complicated at larger H—NH_2 distance by the presence of a conical intersection between the *X* and *A*-state surfaces of NH_3. The product state distribution has been examined extensively by Ashfold and coworkers using a H-atom

photofragment translational spectroscopy [31,32]. According to their results, the dissociation yields primarily the ground-state NH_2 fragments, but with high levels of rotational excitation about the *a*-inertia axis. For the lower v_2' excitation, dissociation from the levels with even quanta yields a much greater proportion of fragments in low rotational quantum states, while those with odd quanta yield $NH_2(X)$ fragments with substantially higher levels of *a*-axis rotational excitation. They also estimated the partition of available energy in $NH_3(A) \rightarrow NH_2(X) + H$ (E_{avl}=1.08 - 1.64 eV for v_2'=0-5). The results indicate a rather small v_2' dependence of energy disposal for the H-atom fragment kinetic energy (0.55 eV and 0.35 eV for v_2'=0 and 5, respectively [32]). These features for the dissociation dynamics of NH_3 may to some extent reflect on those for the clusters. In the following paragraphs, first, I will discuss on the formation process of the protonated cluster ions, and then discuss about that for the unprotonated cluster ions.

As shown in Figure V-4a, the pump-probe curve of NH_3^+ exhibits a nearly symmetric peak with the zero base line. These features indicate that the NH_3^+ ions is mainly produced by the ionization of free NH_3 molecules and the contribution of the fragment ions from larger clusters is negligible within an experimental error. The pump pulses at 197 nm excite NH_3 to the first excited state, while the probe pulses ionize the electronically excited ammonia. The FWHM of the peak (*ca.* 370 fs) is close to that for the cross correlation function of the pump and probe pulses. This result is consistent with an ultrafast predissociation rate of the $A(v_2'=5)$-state ammonia (>1/100 fs [14]). Needless to say, it is indispensable to define the zero of the time of the experimental system to examining the cluster-size dependence of the time evolution of the ions; the time when the overlap between the pump and probe pulses is maximal. However, it is rather difficult to determine the zero of the time because of

the lack of a suitable internal reference. Since the NH_3^+ ions exhibit the ultrafast response as mentioned above, the zero of the time is approximated to the peak of the NH_3^+ ion signals; the present t=0 is quite close to the true one, but not the exact one. As shown in Figure V-4c, the pump-prove curve of $NH_4^+(NH_3)$ shows two decay components such as a large increase in intensity and thereafter a rapid intensity drop, followed by the second slower decay to a non zero value of intensity. The peak of $NH_4^+(NH_3)$ shifts to the longer delay time with respect to t=0. This feature as well as the rapid decay (<0.5 ps) of the first component suggests that the spike is attributable to the signals formed by the AID mechanism. The rapid decay indicates an occurrence of the fast predissociation process in the A (v_2'=5) state. With increasing n, the time to reach the maximum is further delayed as seen in Figures V-4 and 6. And also, the decay time of the fast component is seen to be elongated for larger clusters. These results may suggest the slowing of the predissociation rate with increasing n. The similar trends were also observed in the pump-probe curves for the excitation at lower v_2' by Castleman and coworkers [16,17]. However, they defined the zero of the time not properly, and thus, I cannot compare the present results with theirs directly.

As seen in Figure V-5c, the slower decay component of $NH_4^+NH_3$ levels off to a non zero value of intensity in the delay time longer than *ca.* 5 ps. Since $NH_4(NH_3)_n$ (n≥1) have long lifetimes (≥3 μs) as shown in the next section and have the ionization threshold energies lower than the probe-laser energy (263 nm) [28], the signals of the protonated ions in Δt >5 ps are ascribed to those formed by the one-photon ionization of $NH_4(NH_3)_n$; the solvation of NH_4 (process 5) is expected to be nearly completed in this time region. On the other hand, the slow decaying component in 1 ps<Δt<5 ps may correspond to the process 4. According

to the theoretical calculations by Kassab *et al.* [12], the predissociation of $(NH_3)_2^*$ to produce NH_4 (processes 3 and 4) releases an excess energy of *ca.* 0.9 eV. Most of this energy may be removed by NH_2 fragments in dimer as in the case of free molecule mentioned above. For larger clusters, the amount of excess energy released may be greater than that of dimer, because an excess energy is also generated upon solvation of NH_4; thus the nascent clusters containing NH_4 may be substantially hot. Since the barrier height of the H-atom migration in ammonia clusters is substantially low as mentioned later, the nascent H-atom trapped may migrate inside of the clusters. Some of them loose its kinetic energy through an intracluster vibrational relaxation process to form a stable ammoniated NH_4, but most of them may leave from the clusters. These processes are considered to reflect on the slow decaying signals in 1 ps$<\Delta t<$5 ps. These processes may also include an evaporation of ammonia molecules, which makes a quantitative analysis of the observed curves difficult; the observed decay curve may consist of multiple exponential functions. Because of this reason, I do not make an attempt to convolute the curve to reduce the time constant, however, the ratio between the height of the first peak and the non-zero value in $\Delta t>5$ ps may gives a measure of the quantum efficiency of $NH_4(NH_3)_n$ production.

As for NH_4^+, the rapid decay component is also followed by the slow decaying signals, which decay with much slower rate than those for the slow component of its clusters. These results indicate that NH_4 seems to be formed within <0.6 ps; NH_4 is expected to be formed mainly from ammonia dimer and the excess energy generated in the predissociation process may be removed by NH_2 fragments with much faster rate than those for the clusters. On the other hand, NH_4 has known to be decomposed into NH_3 + H and has an estimated lifetime of <100 ps [23]. Thus, the slow decaying component of the NH_4^+ ion signals is reasonably

ascribed to the decomposition of NH_4. Assuming a single exponential decay, the lifetime of NH_4 is determined to be 13±2 ps. In the next section, I will discuss on this result in more detail.

Except for n=2, the unprotonated ions are not observed in RE2PI with nanosecond lasers as shown in Figure V-7. On the contrary, $(NH_3)_n^+$ are weakly observed in the pump-probe experiments with femtosecond laser pulses. However, these ions are observed only when the pump and probe pulses are temporally overlapped (except for n=2 as seen in Figure V-3). The unique features for the formation of $(NH_3)_2^+$ were also pointed out without a definitive interpretation by Misaizu *et al.* [10] and Castleman *et al.* [17] in the nanosecond and femtosecond photoionization studies, respectively. In order to clarify the mechanism of the formation of this ion, I measure the pump-probe curves as shown in Figures V-4d and V-5d. The temporal profile exhibits an weak spike superimposed on rising signals. In analogy with the above discussions, the spike may correspond to the ion signals through the AID process. On the other hand, the latter signals increase up to the delay time of *ca.* 5 ps and thereafter decrease with much slower decay time; a preliminary pump-probe experiments with nanosecond lasers gives the decay time of <1 ns. This feature indicates that a new intermediate, which is one-photon ionized at 263 nm to produce $(NH_3)_2^+$, is formed by the pump laser at 197 nm. This ion is also found to be detected in the nanosecond pump-probe experiments with the pump wavelength at 212.8 nm and has the appearance energy of 3.79 eV as shown in Figure V-7. The appearance energy obtained by using the ArF excimer laser at 193 nm as the pump laser agrees with the above value. Misaizu and coworkers also estimated crudely the upper limit of ionization energy as 3.99 eV and assigned the intermediate to the excited-state ammonia dimer $[(NH_3)_2^*$ in process 2 [10]]. However, their assignment is inconsistent with the present results.

As mentioned above, the predissociation of the A-state dimer (and also for the A-state clusters) takes place within <1 ps, and as a result, no such efficient enhancement of $(NH_3)_2^+$ is expected by the probe laser in the nanosecond experiments as seen in the case for $(NH_3)_n^+$ ($n \geq 3$) (see Figure V-7). Moreover, if the intermediate is $(NH_3)_2^*$, I could see no rising feature as seen in Figure V-4d. These arguments rule out their assignment and suggest us to consider an alternate candidate. Fortunately, Kassab and coworkers [12], and recently Iwata and coworkers [13] have carried out calculations for the proton- (hydrogen-) transfer surfaces in $(NH_3)_2^+$ and $(NH_3)_2^*$. They predicted that both $(NH_3)_2^+$ and $(NH_3)_2^*$ have no local minimum, and rearrange without proton- (hydrogen-) transfer-barrier to give NH_4^+-NH_2 and NH_4^*-NH_2. Here, the latter species is an excited-state NH_4-NH_2 on the reaction pathway of $(NH_3)_n^*$ to NH_4 + $NH_2(^2B_1)$, which is an A'' pathway in C_s symmetry . According to their results, the complexation energies for NH_4^+-NH_2 and NH_4^*-NH_2 are 1.07 and 0.32 eV, respectively, while the adiabatic ionization potential (IP) of NH_4 is 4.66 eV. From these values, the adiabatic IP of NH_4^*-NH_2 is calculated to be 3.91 eV, which is close to the observed appearance energy of $(NH_3)_2^+$ (3.79 eV). As for NH_4-NH_2, recently, Iwata and coworkers also investigated the potential energy surfaces of the neutral and ionic states of $(NH_3)_2$ in detail using an *ab initio* calculation method with a large basis set [34]. Their calculations show that the ground-state NH_4-NH_2 has no local minimum and dissociates into two ammonia molecules without an energy barrier. Hence, these results as well as the observation, that the intermediate has the lifetime of less than 1 ns, seems to support the assignment of the intermediate as the excited-state NH_4-NH_2 (hereafter abbreviate as NH_4^*-NH_2). They also pointed out that there are at least four low-lying excited states, which give $NH_4(3p)$ + $NH_2(^2B_1)$ and $NH_4(3s)$ + $NH_2(^2A_1)$ at the asymptote, and these states and the

aforementioned excited state are to some extent mixed each other. Therefore, an elaborated theoretical calculation is indispensable to assign the observed intermediate definitively. It is worth to note that the ionization efficiency of $(NH_3)_2^+$ increase rapidly above the threshold as seen in Figure V-7; this result indicates that the geometry of the initial state is similar to that of the ionization state. The observed adiabatic ionization is also compatible with the theoretical expectations; NH_4^*-NH_2 has the electronic structure of the Rydberg nature and its geometrical structure may be close to that of NH_4^+-NH_2.

The above assignment seems to provide us a new insight into the photodissociation mechanism of ammonia clusters in the *A* state. The predissociation of ammonia molecules generates both the H atom and NH_2 radical in the clusters. The H atom is trapped rather efficiently in ammonia clusters. The high trapping efficiency of H atom is due to the fact that NH_4 formed in the intracluster reaction is semi-ionic and it binds to NH_3 with fairly large binding energy (0.34 eV) as mentioned in the next section [28]. On the other hand, the neutral clusters containing NH_2 and the ion clusters such as $NH_2(NH_3)_m^+$ are rarely detected (see Figures V-3 and V-7), because the IPs of NH_2 and $(NH_3)_n$ is much higher than the energy of the probe laser at 263 nm [4,35]. The other possible reason for the hard detection of the neutral clusters may be due to the low trapping efficiency of NH_2 in ammonia clusters. The nascent NH_2 fragments is expected to have a high internal energy as in the case of free molecule mentioned previously. And also, the bonding between NH_2 and NH_3 may be much weaker than that for NH_4-NH_3 [12]. These factors may cause NH_2 difficult to remain in $(NH_3)_m$ after the photolysis. In contrast to these arguments, the above assignment for NH_4^*-NH_2 suggests that both H atom and NH_2 radical are confined in clusters at a certain circumstance. As for larger clusters, an electric deflection study supports a cyclic structure in

the ground state [2]. If this structure is retained in the *A* state (vertical transition), even one of the ammonia molecules takes place the predissociation, the other molecules may attract the fragments (H and NH_2) each other and prevent them from fragmentation; the other molecules may play the role of a cage. The slow rise time of $(NH_3)_2^+$ seems to indicate that it is generated through the photolysis of substantially large clusters.

As mentioned previously, only $(NH_3)_2^+$ is detected in nanosecond experiments. Moreover, in the femtosecond experiments, $(NH_3)_2^+$, $n>2$, are detected only when the pump and probe pulses are nearly overlapped in time. These observations are consistent with each other and may indicate that the precursor such as $(NH_3)_{n-2}NH_4^*$-NH_2, $n>2$, has a lifetime as short as <1 ps. The possible reason for the fast decomposition of these clusters may be due to the nature of the ground- and excited-state surfaces of NH_4-NH_2. As it is expected from the predissociation of NH_3 to NH_2 + H, the reaction pathway of $(NH_3)_n^*$ to NH_4 + $NH_2(^2B_1)$ mentioned previously show a strong avoided crossing originated from a conical intersection known in the ground-state surface of NH_3 to NH_2 + H. Therefore, nonadiavatic transition to the unstable ground state may be strongly enhanced upon complex formation due to these features for the potential energy surfaces as well as the ionic character of NH_4^*-NH_2.

The above arguments suggest that, though the excited-state $(NH_3)_{n-2}NH_4^*$-NH_2 may be formed in the photolysis as in the case of NH_4^*-NH_2, it rapidly rearranges to ammonia clusters *via* the internal conversion (IC) process. If this is the case, in RE2PI with femtosecond lasers, the IC process may compete with the ionization of $(NH_3)_{n-2}NH_4^*$-NH_2 by the probe pulses to form $(NH_3)_2^+$. Hence, it is necessary to consider that $(NH_3)_n^+$ [*i.e.* $(NH_3)_{n-2}NH_4^+$-NH_2] is formed through both the ADI and AID mechanisms as shown in Figure V-10. The formation ratio of

unprotonated ions *via* these two mechanisms depends on the IC rate of $(NH_3)_{n-2}NH_4^*$-NH_2 and the rate of ionization (*i.e.* the fluence of the probe laser). In fact, the ADI mechanism operates dominantly for the production of $(NH_3)_2^+$ as seen in Figure V-3. For $(NH_3)_n^+$ (n>2), both the ADI and AID mechanisms may take part in the formation of these ions.

Stability of $NH_4(NH_3)_n$

The potential energy surface of the ground-state NH_4 has been examined theoretically by several authors [33,34,36]. These studies predicted that the radical has a very shallow potential well in the ground state, which arises from an avoided crossing between the potential curves of the 3*s* state of NH_4 and the valence-shell repulsive state of NH_3 + H. Porter and coworkers examined the stability of NH_4 by neutralized ion-beam technique and estimated the lifetime as less than 150 ns [24]. The present result (13±2 ps) is much shorter than their estimation and is consistent with the observed diffuse feature of the NH_4 Schüler band [23]. The latter authors also determined the heat of reaction ($NH_4 \rightarrow NH_3 + H$) as 0.103 eV from measurements of the kinetic energy released in the H-atom fragments. They also estimated the barrier height along the dissociation coordinate as 0.41±0.7 eV. On the other hand, Kaspar and coworkers calculated the potential energy surface with the barrier height of 0.64-0.75 eV, which agrees rather well with the above experimental result. These authors also predicted that there exists only one quasibound vibrational level (v"=1) with a lifetime of 2 ps for NH_4; dissociation from v"=0 is endothermic and may not take place. However, the result on the lifetime as well as that for the heat of reaction mentioned above indicate

the metastability of NH_4 and seem to be inconsistent with their predictions.

As for n=1 and 2, the lifetimes are determined to be 3±1 and 7±2 μs as shown in Figure V-9. Gellene and coworkers also estimated the lifetime of $NH_4(NH_3)$ as >0.96 μs [25,26], which is compatible with the present results. Thus the lifetime is elongated more than 10^6 times by the complex formation. In the next section of this chapter, I determine the ionization potentials of $NH_4(NH_3)_n$ from the measurements of the ionization efficiency curves [28]. Using these IP results and the successive binding energies ($\Delta H_{n-1,n}$) for $NH_4^+(NH_3)_n$ determined by equilibrium mass spectrometry measurements [37,38], I estimated the binding energies ($D_{n-1,n}$) of the ammoniated radicals. As for n=1, Kebarle and coworkers [37] determined $\Delta H_{0,1}$ as 1.08 eV, while Futrell's group [38] reported a value of 0.93 eV. From these values and the IP of n=1 (3.88 eV [28]), $D_{0,1}$ is estimated to be 0.34 and 0.19 eV, respectively. These values are much larger than the dissociation energy of ammonia dimer [<0.12 eV [39]] and indicate that the bonding between NH_4 and NH_3 is semi-ionic as predicted theoretically by Kassab and Evleth [27]. Since the reaction $NH_4 \rightarrow NH_3 + H$ is nearly isoergic [ΔH=0.103 eV [24]], the significantly larger binding energy of NH_4 with NH_3 comparing with NH_3 itself may cause a decrease in heat of reaction and, as a result, the reaction is suppressed as schematically shown in Figure V-11. From these arguments, the reaction of NH_4NH_3 is expected to be almost endothermic; the heat of reaction is estimated to be -0.12-0.03 eV. However, the result on the lifetime for n=1 (3 μs) seems to suggest that the reaction is still exothermic. For n=2-6, the successive binding energies ($D_{n-1,n}$) were estimated as 0.12, 0.26, 0.30, 0.24, and 0.14 eV, respectively [28]. The reason why $D_{1,2}$ is so small comparing with its neighbor is not clear at present, however, the small binding energy is consistent with the relatively short lifetime of

n=2; the lifetime is elongated only by a factor of two upon complexation with the second ammonia molecule. Since $D_{1,2}$ is close to that for ammonia dimer, the exothermicity of n=2 and the rate of decomposition as well are expected to be close to those for n=1. According to the calculations [27], the optimal structure of $NH_4(NH_3)_4$ is C_{3v}; four NH_3 molecules ligate to H atoms in NH_4 and form the first solvent shell as in the case of $NH_4^+(NH_3)_4$. The rather rapid decrease in $D_{n-1,n}$ from n=4 to 6 seems to support these theoretical predictions. In the calculations, they implicitly assumed that the excess H atom is localized on one ammonia molecule surrounded by the other NH_3 molecules. If this is the case, the clusters with $n\geq4$ may be stable. Contrary to this expectation, $NH_4^+(NH_3)_5$ has a finite lifetime as seen in Figure V-9. This fact may imply that the excess H atom in clusters is partially delocalized in clusters, because the clusters are substantially hot due to its large binding energy. To confirm this possibility, an accurate measurement of the lifetime for larger clusters is underway.

5. Conclusions

In this chapter, I describe the results of investigations on the formation and decay processes of the clusters containing the NH_4 radical produced in the predissociation of the $A(\nu_2'=5)$-state ammonia clusters. The clusters produced by photolysis are detected by the pump-probe technique with nanosecond and femtosecond lasers. The predissociation rate in the A-state ammonia clusters is reduced with increasing n, yet it is completed within 1 ps even for $n\geq4$. The unique time profile of $(NH_3)_2^+$ is ascribed to the formation of a new intermediate, which forms the ammonia dimer ion through one-photon ionization with the probe laser.

On the basis of the result of the IP measurement as well as those of the theoretical calculations, the intermediate is identified as the excited-state NH_4^*-NH_2. The rise time of this species indicates that it is formed through the cage dynamics of the predissociation of large ammonia clusters. These findings give new insight into the photochemical reaction dynamics of ammonia clusters in the *A* state. And also, the results suggest us the new mechanism for the production of unprotonated ions such as the ADI mechanism. This mechanism seems to play an important role in the resonance enhanced MPI with ultrafast laser photons.

The decomposition lifetime of NH_4 is determined to be 13 ps, while that for NH_4NH_3 is found to be 3 μs. The lifetime of larger clusters are longer than 10 μs, yet that for n=5 is finite. Thus the lifetime of NH_3 is elongated more than 10^6 times in clusters. The huge stabilization is ascribed to the semi-ionic character of the NH_4 radical. Since $NH_4(NH_3)_n$ is expected to be rather hot and the energy barrier of H-atom migration in clusters is substantially low, the excess H atom may be to some extent delocalized over the cluster. The fact, that the lifetime of $n \geq 4$ is finite, may support this possibility.

References for Chapter V-1

[1] Levine, R. D.; Berstein, R. B. *Molecular Reaction Dynamics and Chemical Reactivity* ; Oxford University: Oxford, 1987.

[2] Odutola, J. A.; Dyke, T. R.; Howard, B. J.; Muenter, J. S. *J. Chem. Phys.* **1979**, *70*, 4884.

[3] Stephan, K.; Futrell, J. H.; Peterson, K. I.; Castleman, Jr., A. W.; Wagner, H. E.; Djuric, N.; Mark, T. D. *Int. J. Mass Spectrom. Ion Phys.* **1982**, *44*, 167.

[4] Ceyer, S. T.; Tiedemann, P. W.; Mahan, B. H.; Lee, Y. T. *J. Chem. Phys.* **1979**, *70*, 14.

[5] Shinohara, H.; Nishi, N.; Washida, N. *J. Chem. Phys.* **1985**, *83*, 1939.

[6] Kaiser, E.; de Vries, J.; Steger, H.; Menzel, C.; Kamke, W.; Hertel, I.V.*Z.Phys.* **1991**, *D20*, 193.

[7] H. Shinohara and N. Nishi, *Chem. Phys. Lett.*, **87**, 561 (1982).

[8] Echt, O.; Dao, P. D.; Morgan, S.; Castleman, Jr., A. W. *J. Chem. Phys.* **1985**, *82*, 4076.

[9] Misaizu, F.; Houston, P. L.; Nishi, N.; Shinohara, H.; Kondow, T.; Kinoshita, M. *J. Chem. Phys.* **1989**, *93*, 7041.

[10] Misaizu, F.; Houston, P. L.; Nishi, N.; Shinohara, H.; Kondow, T.; Kinoshita, M. *J. Chem. Phys.* **1993**, *98*, 336.

[11] Tomoda, S. *Chem. Phys.* **1986**, *110*, 431.

[12] Cao, H. Z.; Evleth, E. M.; Kassab, E. *J. Chem. Phys.* **1984**, *81*, 1512.

[13] Park, J. K.; Ten-no, S.; Iwata, S. private communication.

[14] Ziegler, L. D. *J. Chem. Phys.* **1986**, *84*, 6013.

[15] Fuke, K.; Yamada, H.; Yoshida, Y.; Kaya, K. *J. Chem. Phys.* **1988**, *88*, 5238.

[16] Wei, S.; Purnell, J.; Buzza, S. A.; Castleman, Jr., A. W. *J. Chem. Phys.* **1993**, *99*, 755.

[17] Purnell, J.; Wei, S.; Buzza, S. A.; Castleman, Jr., A. W. *J. Phys, Chem.* **1993**, *97*, 12530.

[18] Wan, J. K. S. *J. Chem. Educ.* **1968**, *45*, 40.

[19] Brooks, J. M.; Dewald, R. R. *J. Phys. Chem.* **1971**, *75*, 986.

[20] Kariv-Miller, E.; Nanjundiah, C.; Eaton, J.; Swenson, K. E. *J. Elctroanal. Chem.* **1984**, *167*, 141.

[21] Evleth, E. M.; Kassab, E. *Pure App. Chem.* **1988**, *60*, 209.

[22] Herzberg, G. *Faraday Discuss. Chem. Soc.* **1981**, *71*, 165.

[23] Herzberg, G. *J. Astrophys. Astr.* **1984**, *5*, 131.

[24] Gellene, G. I.; Cleary, D. A.; Porter, R. F. *J. Chem. Phys.*, **1982**, *77*, 3471.

[25] Gellene, G. I.; Porter, R. F. *J. Phys. Chem.* **1984**, *88*, 6680.

[26] Jeon, S.; Raksit, A. B.; Gellene, G. I.; Porter, R. F. *J. Am. Chem. Soc.* **1985**, *107*, 4129.

[27] Kassab, E.; Evleth, E. M. *J. Am. Chem. Soc.* **1987**, *109*, 1653.

[28] Fuke, K.; Takasu, R.; Misaizu, F. *Chem. Phys. Lett.* **1994**, *229*, 597.

[29] Misaizu, F.; Sanekata, M.; Fuke, K. *J. Chem. Phys.* **1994**, *100*, 1161.

[30] McCarthy, M.I.; Rosmus, P.; Werner, H.-J.; Botschwina, P.; Vaida, V. *J. Chem. Phys.* **1987**,*86*, 6693.

[31] Biesner, J.; Schnieder, L.; Schmeer, J.; Ahlers, G.; Xie, Xiaoxiang; Welge, K. H.; Ashfold, M. N. R.; Dixon, R. N. *J. Chem. Phys.* **1988**, *88*, 3607.

[32] Biesner, J.; Schnieder, L.; Ahlers, G.; Xie, Xiaoxiang; Welge, K. H.; Ashfold, M. N. R.; Dixon, R. N. *J. Chem. Phys.* **1989**, *91*, 2901.

[33] Kaspar, J.; Smith, Jr., V. H.; MeMaster, B. N. *Chem. Phys.* **1985**, *96*, 81.
[34] Park, J. K. Ten-no, S.; Iwata, S. to be published.
[35] Gibson, S. T.; Greene, J. P.; J. Berkowitz, J. *J. Chem. Phys.* **1985**, *83*, 4319.
[36] Cardy, H.; Liotard, D.; Dargelos, A.; Poquet, E. *Chem. Phys.* **1983**, *77*, 287.
[37] Payzant, J. D.; Cunnungham, A. J.; Kebarle, P. *Can. J. Chem.* **1973**, *51*, 3242.
[38] Arshadi, M. R.; Futrell, J. H. *J. Phys. Chem.* **1974**, *78*, 1482.
[39] Nelson, D. D.; Fraser, G. T.; Klemperer, W. *J. Chem. Phys.* **1985**, ***83***, 6201.

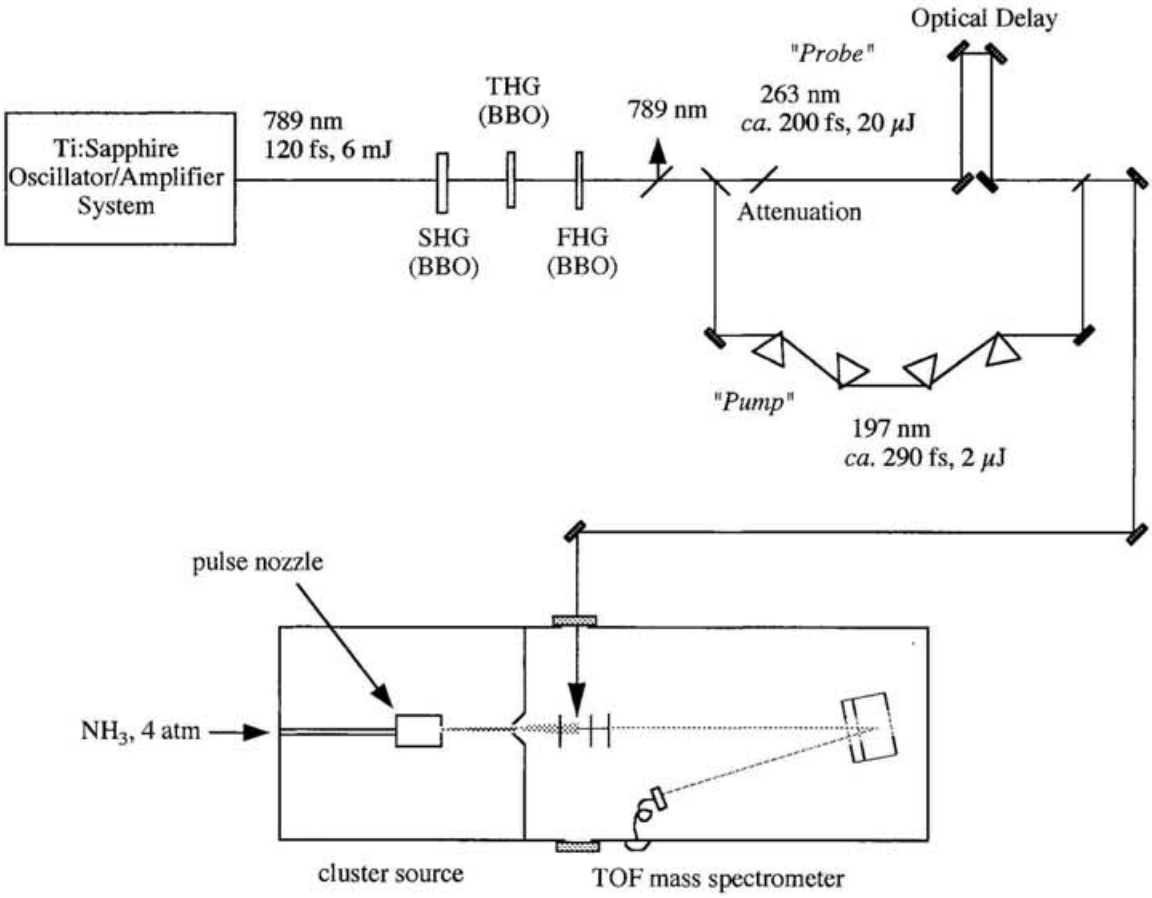

Figure V-1. Setup for femtosecond pump-probe experiments of ammonia clusters.

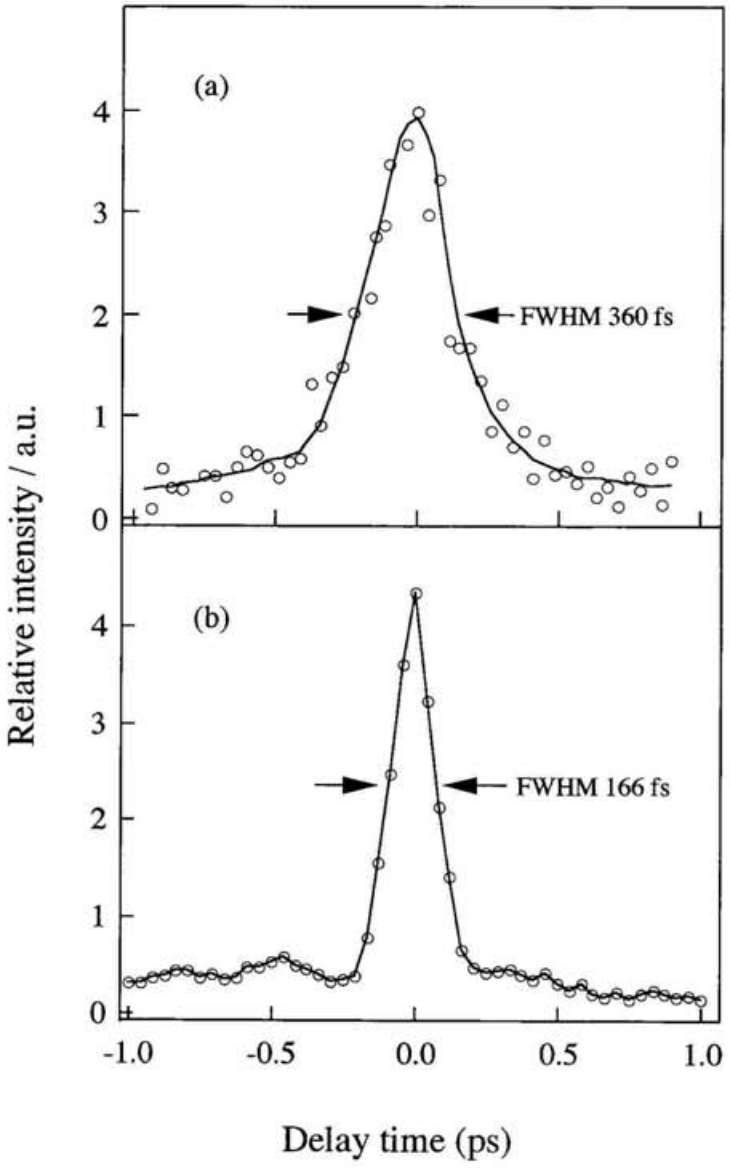

Figure V-2. The time profile of laser pulse. (a) Cross correlation of 789 nm and 197nm. FWHM is 360 fs. (b) Autocorrelation of 789 nm. FWHM is 166 fs.

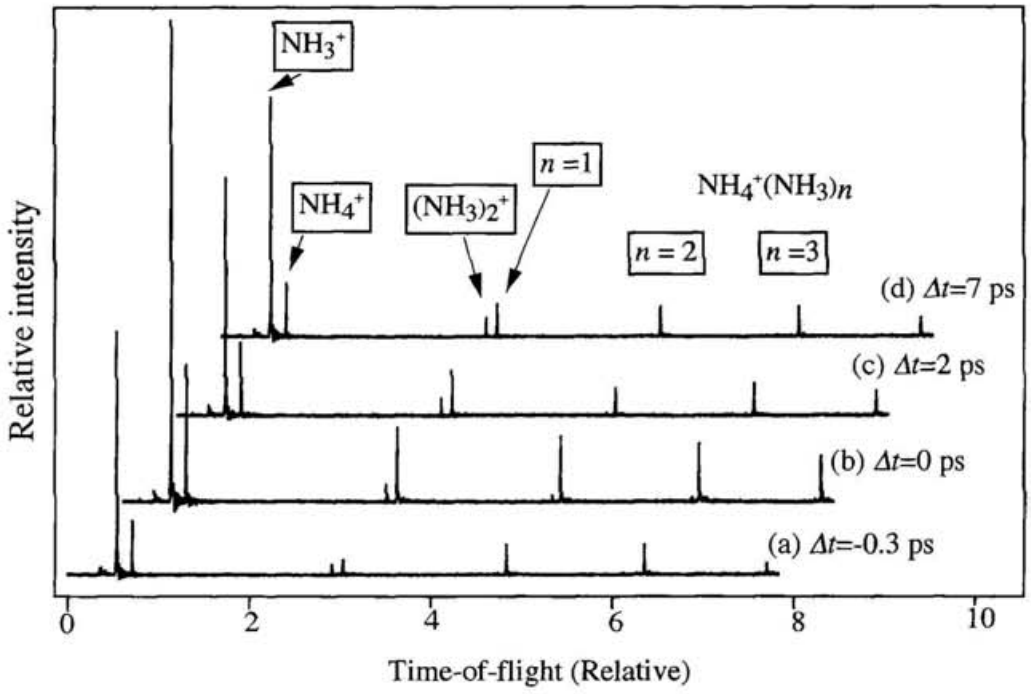

Figure V-3. Typical time-of-flight mass spectra of small ammonia cluster ions generated by femtosecond laser pulses with various delay times; pump pulses at 197 nm, $A(v_2'=5)$, and probe pulses at 263 nm.

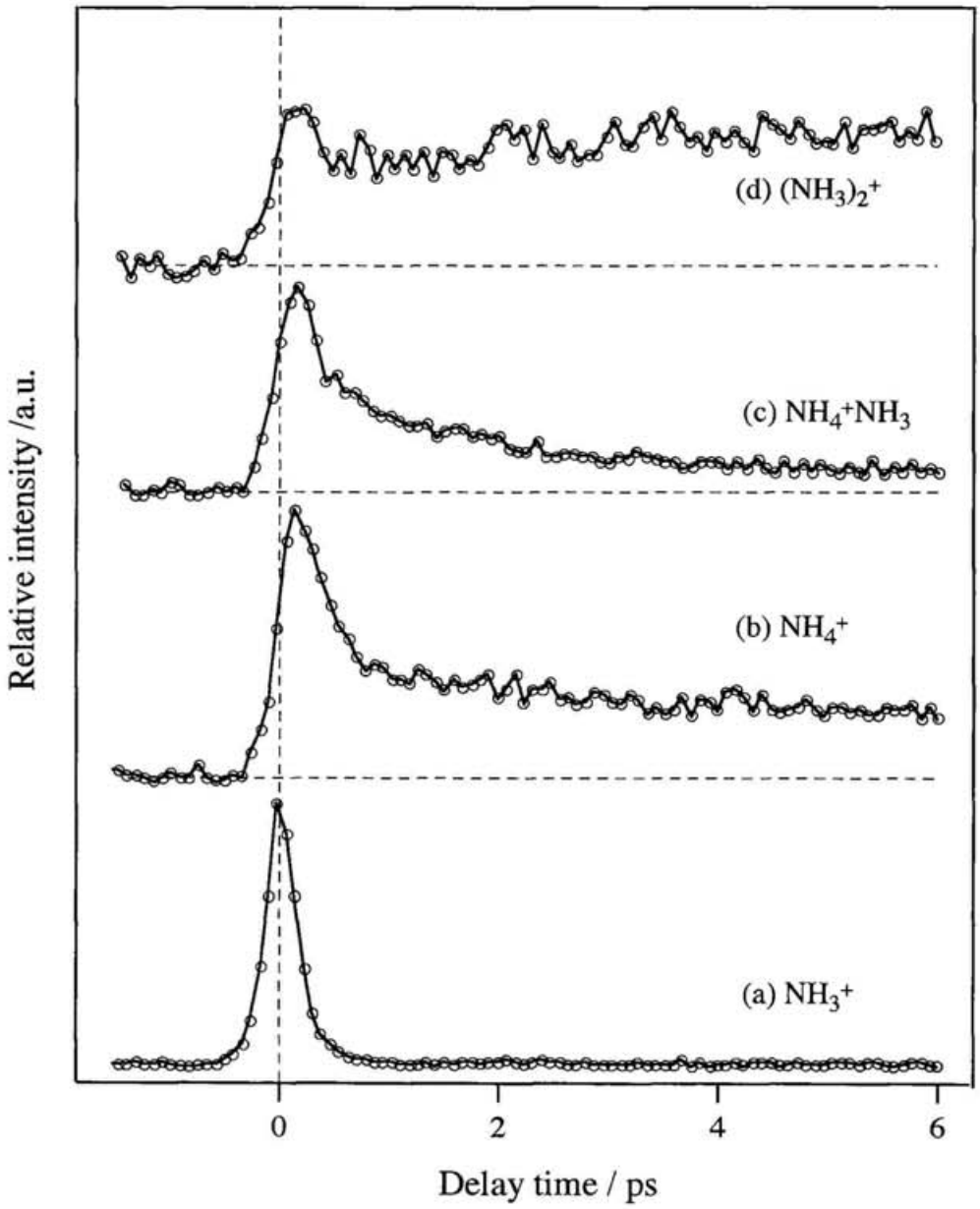

Figure IV-4. Pump-probe curves of (a) NH_3^+, (b) NH_4^+, (c) $NH_4(NH_3)^+$, (d) $(NH_3)_2^+$ with a scan step of 83 fs; pump pulses at 197 nm [$A(\nu_2'=5)$], and probe pulses at 263 nm. The signals, at the time when the probe is ahead of the pump, are the background ion signals from one color ionization by the pump laser alone.

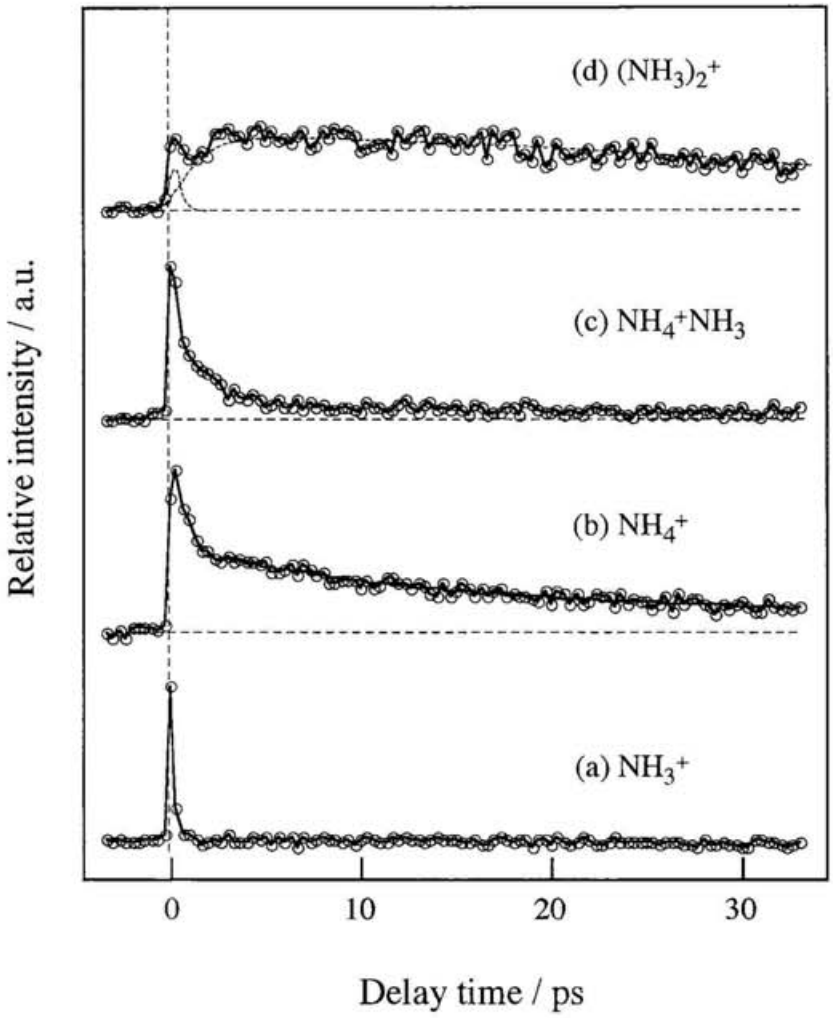

Figure V-5. Pump-probe curves of (a) NH_3^+, (b) NH_4^+, (c) $NH_4(NH_3)^+$ and (d) $(NH_3)_2^+$ with a scan step of 330 fs; pump pulses at 197 nm [$A(v_2'=5)$] and probe pulses at 263 nm. All signals except for NH_3^+ do not fall back to the background level. The intracluster reactions, which form the long-lived clusters containing NH_4, are responsible for these signals.

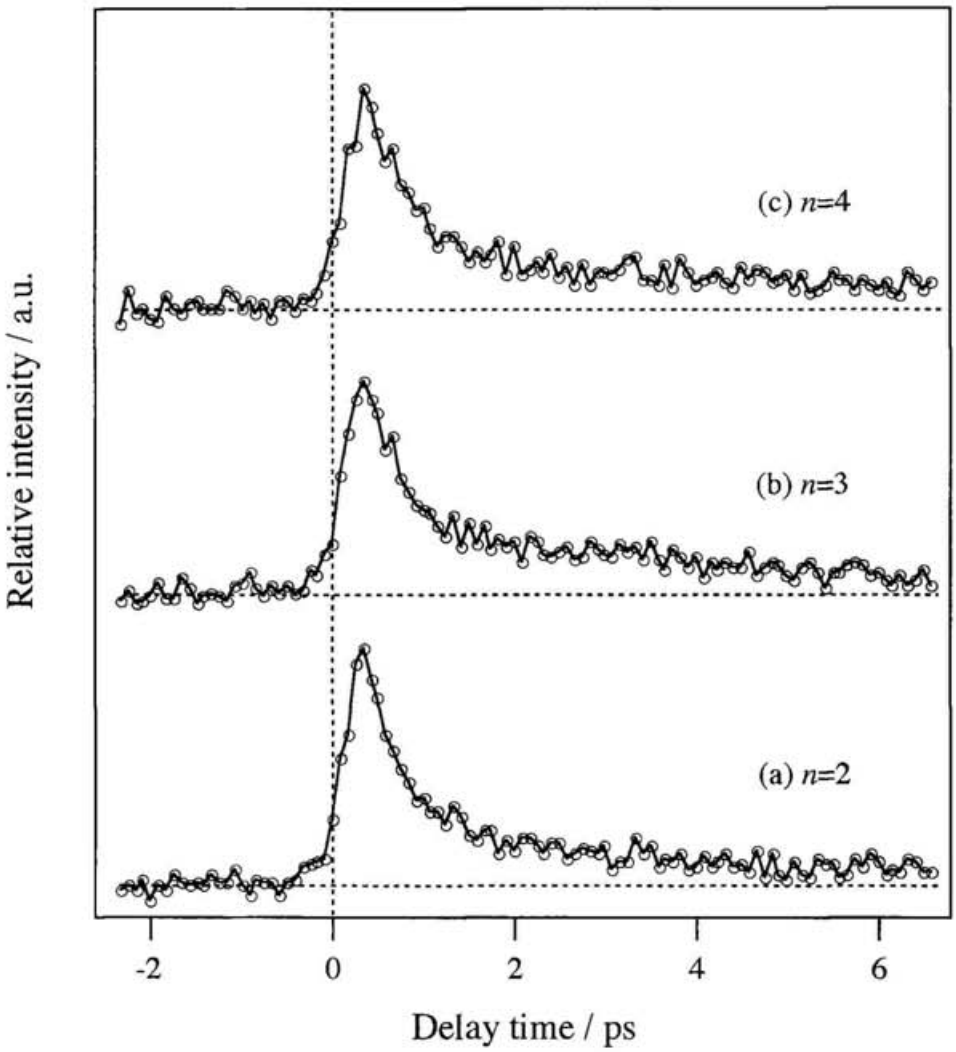

Figure V-6. Pump-probe curves of $NH_4(NH_3)_n^+$, n=2-4, with a scan step of 83 fs; pump pulses at 197 nm [$A(\nu_2'=5)$], and probe pulses at 263 nm.

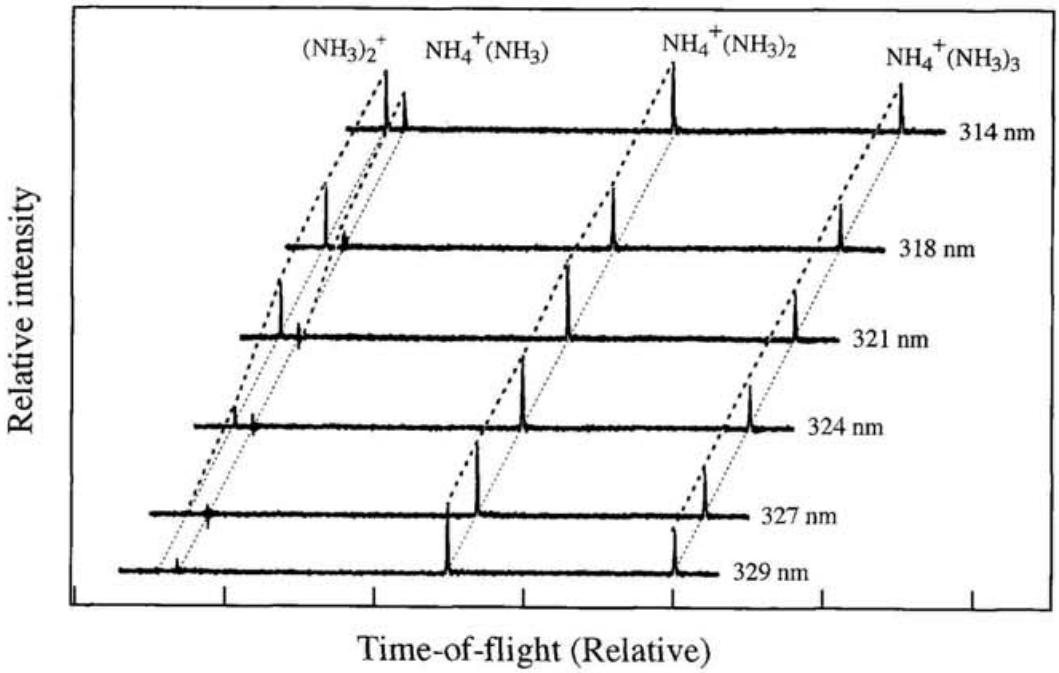

Figure V-7. Typical time-of-flight mass spectra of small ammonia cluster ions generated by two nanosecond laser pulses with zero delay time; pump pulses at 212.8nm, $A(\nu_2'=1)$, and probe laser in the wavelength region of 329-314 nm. $(NH_3)_2^+$ and $NH_4(NH_3)^+$ exhibit threshold behaviors with appearance energies of 3.79 and 3.88 eV, respectively.

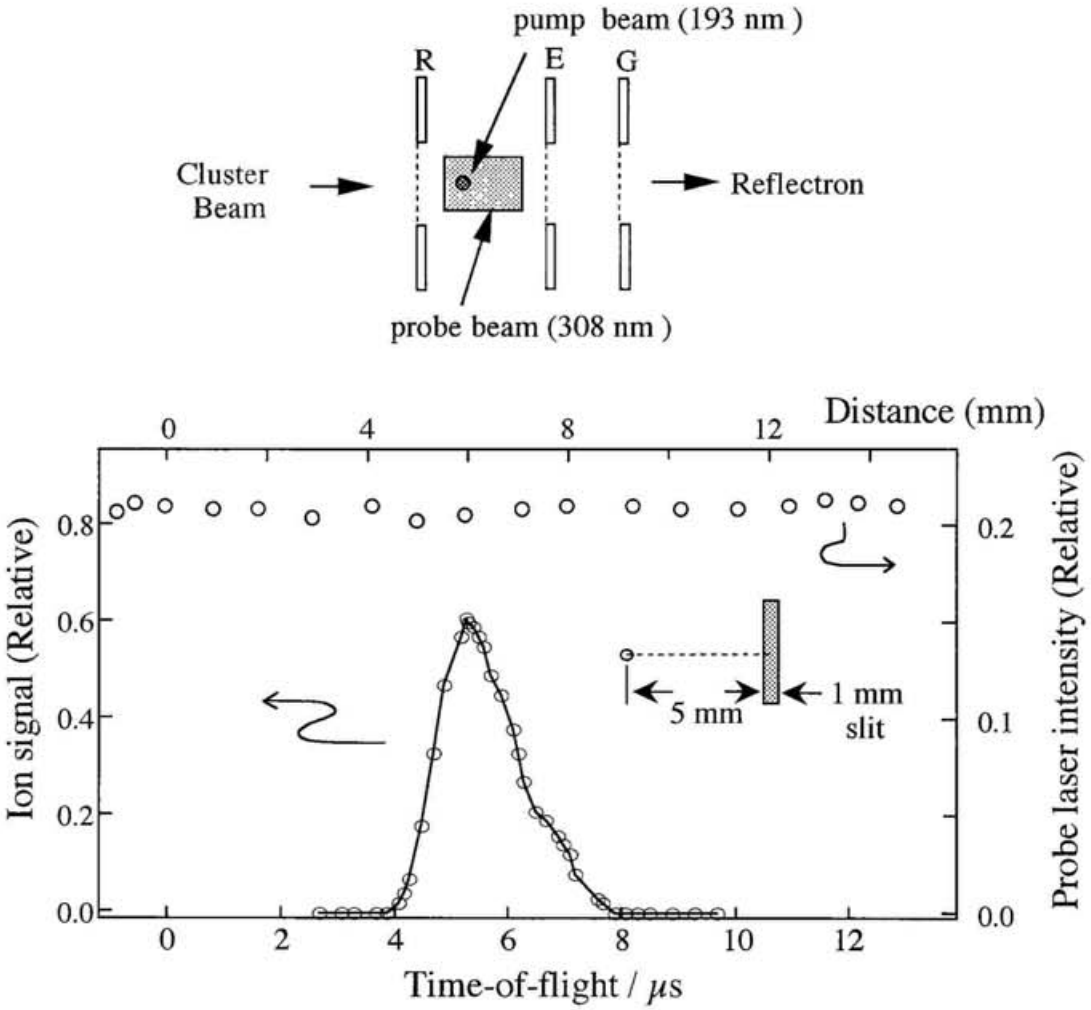

Figure V-8. Schematic configuration of pump-probe experiments for $NH_4(NH_3)_n$ (upper case). Time-of flight of $NH_4(NH_3)_6$ and laser intensity at different portion of probe beam (lower case, see text).

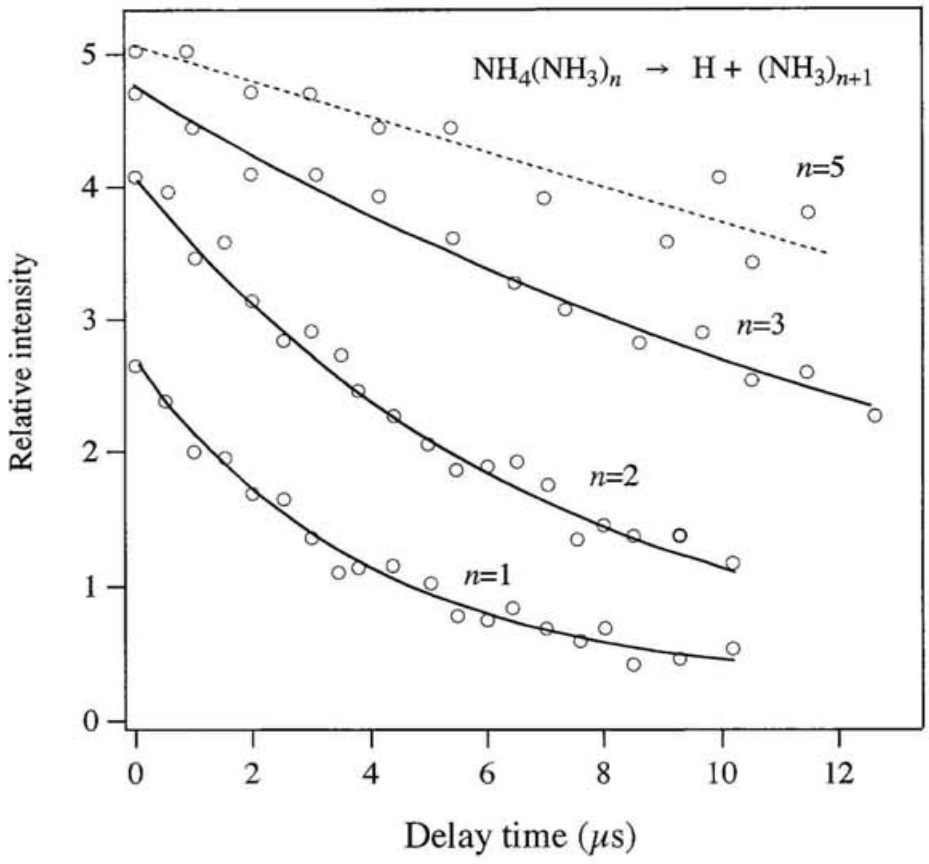

Figure V-9. Pump-probe curves of $NH_4(NH_3)_n$, n=1-3 and 5; pump pulses at 193 nm and probe pulses at 308 nm. Clusters with $n \geq 3$ have a lifetime of longer than 10μs and drift out from the time window.

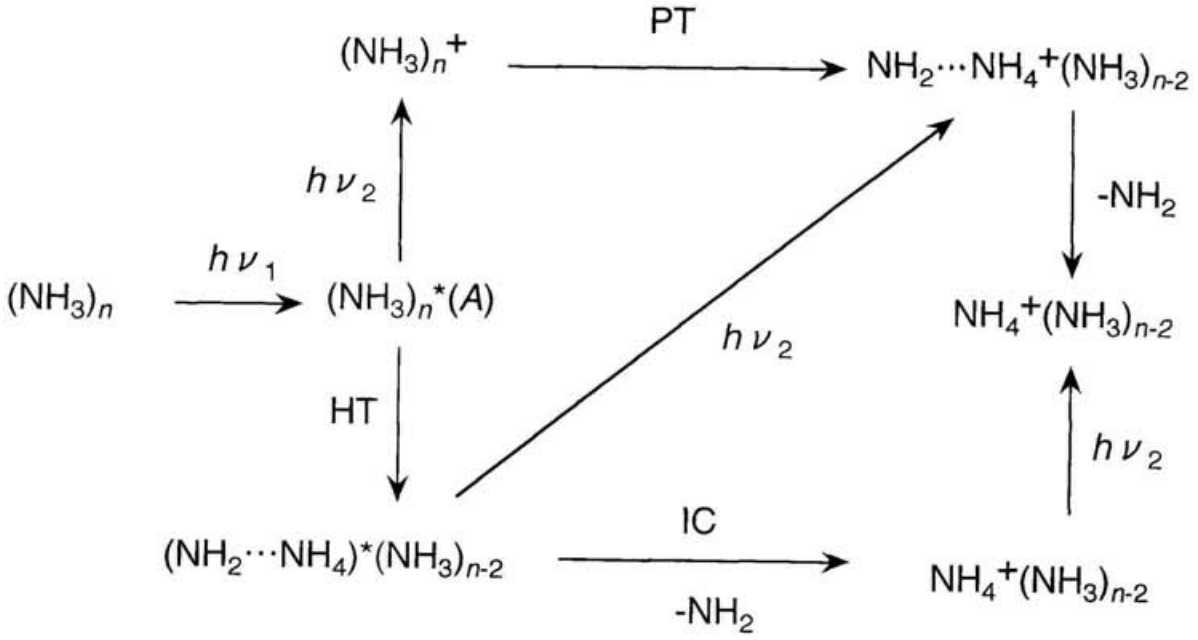

Figure V-10. Possible schemes for the production of unprotonated and protonated cluster ions in the resonance enhanced two-photon ionization through the *A*-state of ammonia clusters. PT; proton transfer reaction without an energy barrier, HT; hydrogen transfer reaction, IC; internal conversion followed by the dissociation of NH_2.

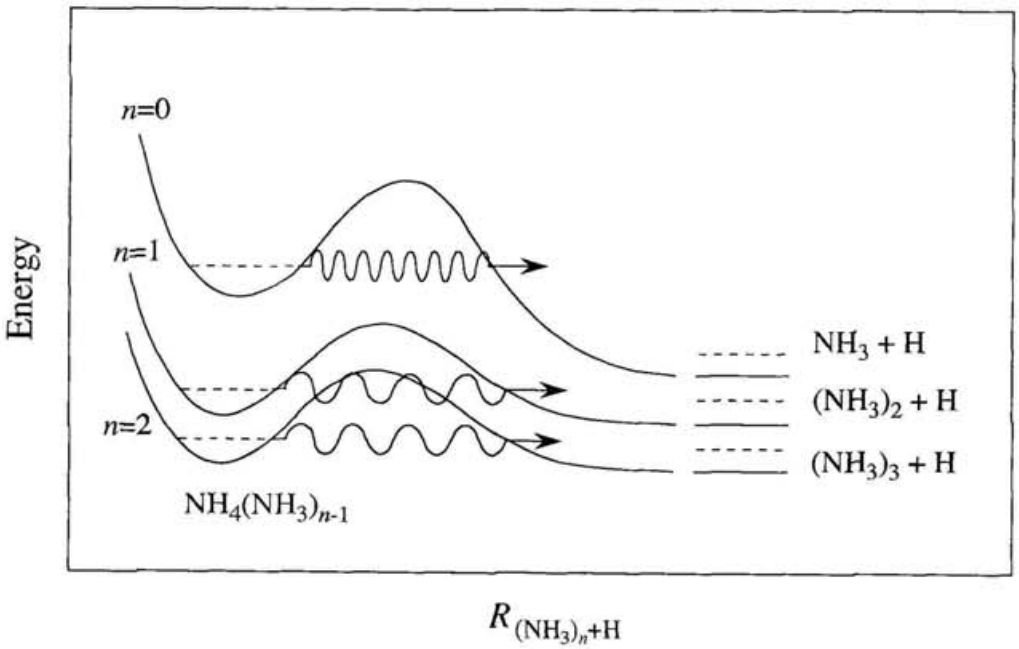

Figure V-11. Schematic illustration for the stabilization mechanism of NH_4 in ammonia clusters.

Chapter V: Section 2
Microscopic solvation process of NH_4 radical

1. Introduction

NH_4 is a typical hypervalent Rydberg radical and isoelectronic with an alkali atom. Its spectroscopic properties have been extensively studied since the first spectroscopic characterization by Herzberg [1,2]. Because NH_4 has a very shallow potential well in the ground state and has a short lifetime, most of the spectroscopic studies have been limited to ND_4 [2-5]. Porter and coworkers have studied the stability of small $NH_4(NH_3)_n$ by neutralized ion beam spectroscopy and found that the radical is stabilized extensively by complex formation with ammonia [6-8]. Recently, the structure and stability of ammoniated NH_4 radical have also been investigated theoretically by Kassab and coworkers [9,10]. These authors have predicted that the ammonia clusters containing this radical are formed as an intermediate in the two-photon ionization process of ammonia clusters through the *A* state. The latter process have been investigated extensively using a nanosecond [11,12] and femtosecond laser spectroscopies [13,14]. However, the experimental data on the electronic structure and stability of ammoniated NH_4 are still quite limited.

Although NH_4 have been first well characterized with spectroscopy in the gas phase, the existence of mercury amalgam has long been

anticipated. The possible existence of NH_4 radical in the reaction of the solvated electron and in electrochemistry has also been speculated on for many years [19-22]. If NH_4 exists as solvated species in the condensed phase, an interesting question is raised how the Rydberg orbital is affected by the presence of large number of other molecules; the radical is expected to have a diffuse electronic structure. Intimately related to this issue, the spectroscopic studies on the clusters composed of metal atoms or its ions solvated with polar molecules have been developed rapidly in recent years. Hertel's and Fuke's groups have examined the photoionization process of the solvent clusters containing neutral alkali atoms such as Na [15] and Cs [16]. Ionization potentials (IPs) of the alkali atom-solvent (H_2O, NH_3) clusters have been determined as a function of the number of solvent molecules, and it is found that the IPs of both $Na(H_2O)_n$ and $Cs(H_2O)_n$ rapidly converge to the photoelectric threshold of ice at n=4. In contrast, the metal-ammonia clusters show a monotonic decrease in the IPs for n as large as 40 and its limiting values ($n\rightarrow\infty$) coincide with the estimated IP of an excess electron solvated in liquid ammonia. Landman and coworkers have examined the IPs for $Na(H_2O)_n$ theoretically to understand these anomalous observations and ascribed these behaviors to an evolution of a Rydberg-like ion-pair state with increasing cluster size [17]. Hashimoto *et al.* have also calculated the same system using an *ab initio* method and proposed an alternate mechanism for the IP saturation [18]. Since NH_4 is isoelectronic with alkali atoms as mentioned above, the ammoniated NH_4 clusters may serve as a new testing material to get further insight into the electron localization modes in the gas-phase clusters. Moreover, the study on the stability of these clusters as a function of the number of solvent molecules may provide us some clues to reveal the aforementioned long standing problems in bulk solution.

In this work, I study the photoionization process of NH_4 in ammonia clusters and ammonia-water binary clusters produced by an ArF laser photolysis of $(NH_3)_n$ and $(NH_3)_m(H_2O)_n$ clusters in a jet. I determine the IPs of these clusters for n up to 35 for ammoniated clusters and $0 \leq m,n \leq 4$ for binary clusters by recording the photoionization efficiency curves as a function of photon energy. From these results and the literature values of the successive binding energies for $NH_4^+(NH_3)_{n-1}—NH_3$, the binding energies of neutral clusters for $n \leq 6$ are determined. On the basis of these results, I will discuss on the electronic structure and stability of these clusters in relation to the electron localization modes in clusters.

2. Experimental

Details of the experimental apparatus used in this work have been described in Chapter II. Ammoniated NH_4 radicals are formed by the photodissociation of ammonia clusters at 193 nm using an ArF excimer laser (Lambda Physik/LPX110i). The ammonia clusters are produced by supersonic expansion of pure ammonia (6 atm) or ammonia seeded in 7 atm Ar gas (20 %) from a pulsed nozzle. $NH_4(NH_3)_m(H_2O)_n$ clusters are produced by photolyzing the water-ammonia binary clusters by ArF excimer laser (193 nm). The binary clusters are produced by charging the ammonia-water (Kanto Kagaku, 28%) in the reservoir, and Ar gas is used as a carrier gas. In the photoionization threshold measurements, the ArF laser and the dye laser beams are introduced colinearly and counterpropagatedly to the acceleration region of the mass spectrometer. Both laser beams are collimated to ≈3 mm spot and irradiated to the cluster beam at right angles without focusing. The second harmonic of the dye laser output (Quanta-Ray/GCR3/PDL-3) and the sum-frequency

output of a Nd:YAG fundamental (1064 nm) and dye laser are also used for photoionization in the wavelength regions of 280-350 nm and 260-280 nm, respectively, by utilizing KDP crystals mounted on a wavelength extension system (Quanta-Ray/WEX). The laser fluence is attenuated to less than 1 mJ/cm^2 in order to avoid multiphoton ionization. The delay time between two lasers is typically 200-700 ns.

Photoionization mass spectra are obtained by scanning the photon energy with an interval of 0.02 eV in the region 2.07-4.77 eV (260-600 nm). The ionization thresholds are determined within ±0.03 eV by analyzing the mass spectra. The error caused by field ionization is estimated to be about 0.01 eV in the present experimental conditions.

The ammonia (NH_3, minimum purity of 99.99 %, Nippon Sanso) and deuterated ammonia (ND_3, minimum purity 99.4 atom % D, Matheson) are used without further purification.

3. Results

Photoionization of $NH_4(NH_3)_n$

Figure V-12a shows a typical TOF mass spectrum of protonated ammonia clusters, $NH_4^+(NH_3)_n$ produced by two photons of the ArF excimer laser at 193 nm. It has been known that protonated ammonia clusters are exclusively produced with multiphoton ionization conditions [24,25]; two mechanisms such as an absorption-ionization-dissociation and an absorption-dissociation-ionization are found to contribute to the formation of these cluster ions [11-14]. Since the mass spectrum in Figure V-12a is obtained with comparatively high laser fluence (≈10 mJ/cm^2), both mechanisms may take part in the production of these

cluster ions. On the other hand, Figure V-12b shows the mass spectrum obtained by two-step photoionization process, in which ammonia clusters are photolyzed by the pump laser (ArF, 0.2 mJ/cm^2) as follows,

$$(NH_3)_n \rightarrow NH_4(NH_3)_m + NH_2 + (n\text{-}m\text{-}2)NH_3 \qquad (1)$$

and the produced ammoniated NH_4 radicals are ionized by the probe laser at 350 nm ($\approx$1 mJ/cm^2) with a delay time of 400 ns. As seen in this figure, all mass peaks for $n\geq2$ exhibit doublet features. The peaks with shorter TOFs (left-hand-side of the double peaks) correspond to the protonated cluster ion signals produced by the pump laser alone, while those with longer TOFs (right-hand-side) are ascribed to the ions from one-photon ionization of the ammoniated NH_4 radicals generated by the pump laser. As for the free radical and the n=1 complex, no enhanced signal is observed, because they have higher ionization potentials (IPs) than the energy of the probe laser photon (3.54 eV) as shown later. Interestingly, these mass spectra exhibit the similar feature; a magic behavior appears at n=4. The first solvation shell around the NH_4^+ ion has been known to be closed with four NH_3 molecules; as a result, a magic behavior is expected at n=4 [26]. In the case of the two-photon ionization at 193 nm, large excess energy may be fed into the product ions causing fragmentation. Thus the enhanced peak at n=4 in Figure V-12a may reflect the enhanced stability of the cluster ion. On the other hand, the mass spectrum in Figure V-12b still shows the similar magic behavior at n=4. Since the energy of the probe laser is close to the photoionization threshold, the fragmentation due to the excess energy at ionization seems to be negligible. Therefore, the magic behavior seen in Figure V-12b may be ascribed to the enhanced stability of neutral clusters as discussed later.

Figure V-13 shows the photoionization efficiency curve near the threshold for ND_4 normalized with the laser fluence at each wavelength. Since the lifetime of NH_4 is too short to determine the photoionization threshold energy, therefore, I measure the efficiency curve for ND_4 instead of NH_4. Near the threshold, the ion signals decrease almost linearly with decreasing photon energy, and the linear extrapolation gives the threshold energy as 4.60 eV. As for n=1, I measure the ionization efficiency curves for both undeuterated and deuterated complexes in order to estimate the shift in the zero-point energy with deuterium substitution. The threshold energies are obtained as 3.875 eV for $NH_4(NH_3)$ and 3.851 eV for $ND_4(ND_3)$, respectively; the threshold energy is shifted to the lower energy by *ca.* 0.02 eV upon deuteration. The observed red-shift is consistent with a deeper well depth in the ionization state compared with that in the neutral ground state. Since the vibrational frequencies of the extra NH_3 (or ND_3) for n=1 and those of the intermolecular vibrational modes in the ionization state may not change significantly from those in the neutral ground state, the amount of the red-shifting for the free radical is expected to be nearly the same as that for n=1; thus the ionization threshold energy for NH_4 is estimated to be 4.62 eV. I also measure the photoionization efficiency curves for $NH_4(NH_3)_n$ ($2 \le n \le 35$) and determine the IPs. In Figure V-14, the IPs for $n \le 35$ are plotted as a function of $(n+1)^{-1/3}$. The intercept of the fitted line at $(n+1)^{-1/3} = 0$ ($n \rightarrow \infty$) is 1.33 eV. This value is in agreement with the results of the photoionization experiment for $Cs(NH_3)_n$ (1.4 eV) [16], and also coincides with the limiting value of the vertical detachment energy for $(NH_3)_n^-$ determined by photoelectron spectroscopy [27]. Figure V-15 shows the schematic energy levels of the neutral and cation clusters for $n \le 6$; where the successive binding energies of $NH_4^+(NH_3)_n$ (n=1-6) are

cited from the references [28,29]. From these values, I estimate the binding energies for the neutral clusters as shown in Figure V-15.

Photoionization of $NH_4(NH_3)_m(H_2O)_n$

Figure V-16a shows the photoionization mass spectrum of $NH_4(NH_3)_m(H_2O)_n$ produced by the ArF laser photolysis of ammonia-water binary clusters. Solvated radicals are generated and photoionized by the sequential absorption of two photons of 193 nm laser pulse. On the other hand, Figure V-16b shows the mass spectrum obtained with the 280-nm photon as the ionization light source. The delay time between the photolysis and ionization lasers is 500 ns. As seen in this figure, NH_4 radical is also stabilized even in ammonia-water binary clusters. I determined the IPs for these clusters by measuring the photoionization efficiency curves as a function of photon energy. The results are represented in Figure V-17. With the present method, it is rather difficult to prepare the water clusters containing NH_4 except for n=1. Clusters which do not contain NH_4, such as $(H_2O)_n^+$ or $H(H_2O)_n^+$ are not observed.

4. Discussion

The electronic structure and stability of NH_4 have been examined theoretically by numerous authors using *ab initio* method [30,31]. These studies predicted that the radical has a very shallow potential well in the ground state, which arises from an avoided crossing between the potential curves of the 3*s* state of NH_4 and the valence-shell

repulsive state of NH_3 + H; the latter state rises rapidly in energy as the N-H distance is decreased. Porter and coworkers examined the stability of NH_4 by neutralized ion-beam spectroscopy and estimated the lifetime as less than 150 ns [6]. These results are consistent with the observed diffuse feature of the NH_4 Schüler band [2]. The latter authors also determined the heat of reaction ($NH_4 \rightarrow NH_3$ + H) as 0.103 eV from measurements of the kinetic energy released in the fragmentation products [6]. Using this value as well as the literature values for the proton affinity of NH_3 and the IP of H-atom, they estimated the IP of NH_4 as 4.73±0.06 eV. This value is close to the present result for NH_4 (4.62 eV). The photoionization threshold measurement usually gives a vertical IP, however, the above agreement in IPs indicates that this is not the case for NH_4. This result seems to be due to the fact that NH_4 has to some extent ionic character in the neutral ground state as discussed below. As for the ammoniated NH_4, they also estimated IPs as 4.0, 3.0-3.3, and 2.4-2.6 for n=1-3, respectively, adopting with the theoretically expected binding energy, $D(NH_4(NH_3)_{n-1}—NH_3)$ [7,8]. These values are slightly higher than the present results as summarized in Figure V-15. Misaizu and coworkers also measured the IPs as 3.25, 2.94, and 2.74 eV for n=2-4, respectively, by the photoionization experiments [12]: their values for n=2 and 3 are slightly lower than the present results.

Using the present IP results and the successive binding energies ($\Delta H_{n-1,n}$) for $NH_4^+(NH_3)_n$ determined by equilibrium mass spectrometry measurements [27,28], I estimate the binding energies ($D_{n-1,n}$) of the ammoniated radicals as shown in Figure V-15. There is some discrepancy in the values of $\Delta H_{0,1}$ reported by the different groups. Kebarle and coworkers [28] determined $\Delta H_{0,1}$ as 24.8 kcal/mol (1.08 eV), while Futrell's group [29] reported a value of 21.5 kcal/mol (0.93 eV). From these values, $D_{0,1}$ is estimated to be 0.34 and 0.19 eV, respectively.

These values are much larger than the dissociation energy of ammonia dimer (<0.12 eV [32]) and indicate that the bonding between NH_4 and NH_3 is semi-ionic as pointed out by Kassab and Evleth [10]. As shown in Figure V-15, $D_{1,2}$ is small, but $D_{2,3}$ and $D_{3,4}$ are substantially large. The reason why $D_{1,2}$ is so small comparing with its neighbors is not clear at present. According to the calculations [10], the optimal structure of $NH_4(NH_3)_4$ is C_{3v}; four NH_3 molecules ligate to H atoms in NH_4 and form the first solvent shell as in the case of $NH_4^+(NH_3)_4$. The rather rapid decrease in $D_{n-1,n}$ from n=4 to 6 as seen in Figure V-15 seems to be consistent with these theoretical predictions. These results on the binding energies also provide us insights on the metastability of the radical clusters. Since the reaction $NH_4 \rightarrow NH_3 + H$ is nearly isoergic (ΔH=0.103 eV [6]), the significantly larger binding energy of NH_4 with NH_3 comparing with NH_3 itself may cause the suppression of the reaction. As for NH_4NH_3, the binding energy is obtained as 0.19-0.34 eV, while that for NH_3 dimer is <0.12 eV [32]. From these values as well as the above ΔH value, the reaction of NH_4NH_3 is expected to be almost endothermic; the heat of reaction is estimated to be -0.12-0.03 eV. However, the result of the lifetime measurement in previous section for n=1 (3±1 μs) seems to suggest that the reaction is still exothermic. To estimate the stability for the larger clusters, an accurate measurement of the lifetime is underway.

The IPs determined for n up to 35 are plotted in Figure V-14 as a function of $(n+1)^{-1/3}$. Since the IP value of NH_4 determined in this work is close to the adiabatic IP estimated with neutralized ion beam method [6], we can reasonably assume that the observed threshold energies for larger clusters are also close to the adiabatic IPs. The IPs decrease rapidly from n=3 to 4 and then decrease further gradually with increasing cluster size. The rapid decrease in IPs from n=3 to 7 may be due to the large stabilization of the ionic state with respect to the neutral ground state by

clustering. Interestingly, the trend in IPs changes at $n\approx17$ as seen in Figure V-14 and the IPs for larger clusters decrease almost linearly with decreasing $(n+1)^{-1/3}$. As for $NH_4^+(NH_3)_n$, the second solvent shell is known to be closed with *ca.* 20 ammonia molecules [33]. Since the binding of NH_4 with NH_3 is partially ionic in character, the similar shell structure may be expected for the radical clusters. If this is the case, the size region showing the linear decrease in IP may correspond to the filling of the second solvent shell. Because of the weak signals, I cannot determine the threshold energies for $n>35$, however, the IPs for these clusters are found to decrease further with increasing cluster size. It is worth noting that the limiting value of the IPs versus $(n+1)^{-1/3}$ plots agrees with that for the photoemission thresholds of negatively charged ammonia clusters [27]. Although the feature of IPs for the small $NH_4(NH_3)_n$ clusters is a little bit different from that for the Cs-ammonia system [16], the trends in IPs for the large clusters are quite similar; these systems give the same limiting value as *ca.* 1.4 eV.

In relation to these observations, it is interesting to consider how the distribution of the 3*s* Rydberg electron on NH_4 is affected by complexation. Kassab and Evleth calculated the nitrogen spin densities for $NH_4(NH_3)_n$ ($n\leq6$) and argued the location of the Rydberg electron in the radical clusters. According to their calculations, the nitrogen atom of the NH_4 unit dominates the spin density for n=0-2, while the spin densities are transferred to the external N atoms of the clustering NH_3 groups for n=3 and 4. For n=5 and 6, in which the NH_3 molecules in the first solvent shell are further ligated by other NH_3 groups, the spin densities are forced off these NH_3 units to increase the density on the uncomplexed NH_3 units. On the basis of these results as well as those for the clusters of H_2 and He containing an excited-state NH_3 molecule, they proposed a bubble-state structure for the Rydberg electron embedded in clusters [10]; in this

model, the Rydberg electron will avoid the valence electron space of ligated NH_3 and create or seek empty electron space. They also extended this argument to the liquid phase to estimate the stability of the NH_4 radical in liquid NH_3; they proposed a bubble structure of this radical in liquid including $NH_4(NH_3)_4$ as a preferred structural unit. If this is the case, the extra NH_3 molecules bind to this unit with much weaker binding energy. The rapid decrease in $D_{n-1,n}$ from n=3 to 6 as shown in Figure V-15 seems to be consistent with the above expectation. They also suggested that the stepwise NH_4 binding energies tend to zero and perhaps become destabilizing as the cluster size increases. However, the present results clearly show that the clusters with more than 35 NH_3 molecules are also stable and are able to detect with a reasonable intensity. Moreover, as in the case of $Cs(NH_3)_n$, the IP of these clusters is found to converge to the photoemission thresholds of liquid NH_3. As for $Cs(NH_3)_n$, Martyna and Klein examined the electronic structure using pseudopotential calculation and predicted that the valence electron of the metal is driven into a Rydberg-like state as the number of ammonia molecules increases [34]. Thus, on the contrary to the theoretical expectation, these results suggest that the Rydberg electron may be further squeezed out over the second-shell ammonia molecules when the second shell is closing.

In Figure V-17, IPs for $NH_4(NH_3)_m(H_2O)_n$ are plotted. As for $NH_4(H_2O)$, the IP is estimated to be 4.07 eV and is higher than that for $NH_4(NH_3)$ (3.88 eV). From the binding energy of NH_4^+—H_2O determined by high pressure mass spectrometry (0.89 eV [32]) as well as the IP of NH_4, the binding energy of NH_4—H_2O is estimated to be 0.34 eV. This value is a little bit larger than the binding energy with NH_3. The difference in IPs for the water and ammonia complexes is due to the large solvation energy of the latter molecules in the ionization state. As shown in Figure V-17, the IPs of $NH_4(NH_3)_m(H_2O)_n$ show a clear trend. In

comparing the IPs the clusters with the same solvation number k (k=m+n), IP decreases monotonically with the increase of the NH_3 molecule. This trend is ascribed to the much larger binding energy of NH_4^+—NH_3 comparing with that for NH_4^+—H_2O as mentioned above. Since there is no experimental and theoretical studies for the binding energy of NH_4^+ with ammonia-water clusters, I cannot determine the binding energies of these clusters in the neutral ground state. However, the above trend in IPs within the same k seems to indicate that NH_3 binds directly with NH_4. It is interesting to consider whether the clusters containing H_3O as the core is possible to exist in the binary clusters. As for $H(NH_3)_m(H_2O)_n^+$, NH_4^+ is the core of the clusters because the proton affinity of NH_3 (8.89 eV) is much larger than that of H_2O (7.50 eV) [26]. But, in the case of neutral clusters, the situation seems to be different. NH_4 is dissociative and the hydrogen atom affinity (HA) of NH_3 is negative. Gellene and Porter examined the stability of these clusters in the neutralized ion beam [36]. These results indicate that though H_3O is unstable, it is stabilized in the water clusters and possibly in the water-ammonia binary clusters. However, the theoretical calculations predict that the relative energy of H_3O with respect to H_2O + H is almost 1 eV larger than that of NH_4 with respect to NH_3 + H [37]. Therefore, NH_4 is the core in the small-sized water-ammonia binary clusters.

In order to get further insight into the electron delocalization in these clusters, I am performing the IP measurements for larger $NH_4(NH_3)_n$ clusters as well as for a larger mixed cluster with water molecules. An elaborated quantum calculation on the larger clusters would be welcome.

References for Chapter V-2

[1] Hertzberg, G. *Faraday Disc. Chem. Soc.* **1981**, *71*, 165.
[2] Hertzberg, G. *J. Astrophys. Astr.* **1981**, *5*, 131.
[3] Whittaker, E. A.; Sullivan, B. J.; Bjorklund, G. C.; Wendt, H. R.; Hunziker, H. E. *J. Chem. Phys.* **1984**, *80*, 961.
[4] Watson, J. K. G. *J. Mol. Spectrosc.* **1984**, *107*, 124.
[5] Alberti, F.; Huber, K. P.; Watson, J. K. G. *J. Mol. Phys.* **1984**, *107*, 133.
[6] Gellene, G. I.; Cleary, D. A.; Porter, R. F. *J. Chem. Phys.* **1982**, *77*, 3471.
[7] Gellene, G. I.; Porter, R. F. *J. Phys. Chem.* **1984**, *88*, 6680.
[8] Jeon, S.; Raksit, A. B.; Gellene, G. I.; Porter, R. F. *J. Am. Chem. Soc.* **1985**, *107*, 4129.
[9] Cao, H. Z.; Kassab, E.; Evleth, E. M. *J. Chem. Phys.* **1984**, *81*, 1512.
[10] Kassab, E.; Evleth, E. M. *J. Am. Chem. Soc.* **1987**, *109*, 1653.
[11] Misaizu, F.; Houston, P. L.; Nishi, N.; Shinohara, H.; Kondow, T.; Kinoshita, M. *J. Phys. Chem.* **1989**, *93*, 7041.
[12] Misaizu, F.; Houston, P. L.; Nishi, N.; Shinohara, H.; Kondow, T.; Kinoshita, M. *J. Chem. Phys.* **1993**, *98*, 336.
[13] Wei, S.; Purnell, J.; Buzza, S. A.; Castleman, Jr., A. W. *J. Chem. Phys.* **1993**, *99*, 755.
[14] Purnell, J.; Wei, S.; Buzza, S. A.; Castleman, Jr., A. W. *J. Phys. Chem.* **1993**, *97*, 12530.
[15] Hertel, I. V.; Hüglin, C.; Nitsch, C.; Schultz, C. P. *Phys. Rev. Lett.* **1991**, *67*, 1767.
[16] Misaizu, F.; Tsukamoto, K.; Sanekata, M.; Fuke, K, *Chem. Phys. Lett.* **1992**, *188*, 241.
[17] Barnett, R. N.; Landman, U. *Phys. Rev. Lett.* **1993**, *70*, 1775.
[18] Hashimoto, K.; He, S.; Morokuma, K. *Chem. Phys. Lett.* **1993**, *206*, 297.
[19] Wan, J. K. S. *J. Chem. Educ.* **1968**, *45*, 40.
[20] Brooks, J. M.; Dewald, R. R. *J. Phys. Chem.* **1971**, *75* , 986.
[21] Kariv-Miller, E.; Nanjundiah, C.; Eaton, J.; Swenson, K. E. *J. Elctroanal. Chem.* **1984**, *167*, 141.
[22] Evleth, E. M.; Kassab, E. *Pure App. Chem.* **1988**, *60*, 209.
[23] Misaizu, F.; Sanekata, M.; Fuke, K. *J. Phys. Chem.* **1994**, *100*, 1161.
[24] Shinohara, H.; Nishi, N. *Chem. Phys. Lett.* **1982**, *87*, 561.
[25] Echt, O.; Morgan, S.; Dao, P. D.; Stanley, R. J.; Castleman, Jr., A. W. *J. Chem. Phys.* **1985**, *82*, 4076.
[26] Wei, S.; Tzeng, W. B.; Castleman, Jr., A. W. *J. Chem. Phys.* **1990**, *93*, 2506.
[27] Lee, G. H.; Arnold, S. T.; Eaton, J. G.; Sarkas, H. W.; Bowen, K. H.; Ludewigt, C.; Haberland, H. *Z. Phys.* **1991**, *D20*, 9.
[28] Payzant, J. D.; Cunnungham, A. J.; Kebarle, P. *Can. J. Chem.* **1973**, *51*, 3242.
[29] Arshadi, M. R.; Futrell, J. H. *J. Phys. Chem.* **1974**, *78*, 1482.
[30] Cardy, H.; Liotard, D.; Dargelos, A.; Poquet, E. *Chem. Phys.* **1983**, *77*, 287.
[31] Kaspar, J.; Smith, Jr., V. H.; MeMaster, B. N. *Chem. Phys.* **1985**, *96*, 81.
[32] Nelson, D. D.; Fraser, G. T.; Klemperer, W. *J. Chem. Phys.* **1985**, *83*, 6201.
[33] Shinohara, H.; Nishi, N.; Washida, N. *J. Chem. Phys.* **1985**, *83*, 1939.
[34] Martyna, G. J.; Klein, M. L. *J. Phys. Chem.* **1991**, *95*, 515.
[35] Meot-Ner (Mautner), M; Speller, C. V. *J. Phys. Chem.* **1986**, *90*, 6616.

[36] Aue, D. H.; Bowers, M. T. in *Gas Phase Ion Chemistry* , edited by Bowers, M. T. (Academic Press, New York, 1979)
[37] Tennou, S. personal communication.

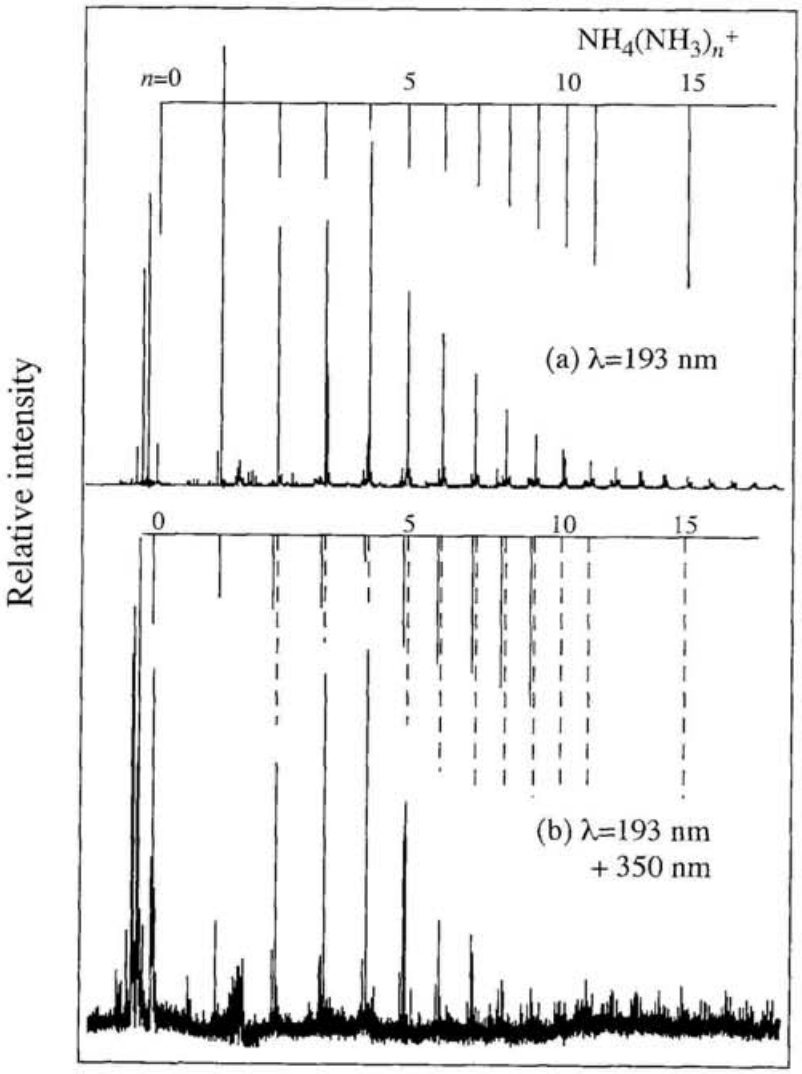

Figure V-12. (a) Typical time-of-flight mass spectrum of protonated ammonia clusters produced by two photons of 193 nm (≈10 mJ/cm^2). (b) Time-of-flight mass spectrum at delay time of 400 ns between the pump (193 nm, ≈0.2 mJ/cm^2) and probe (350 nm, ≈1 mJ/cm^2) lasers.

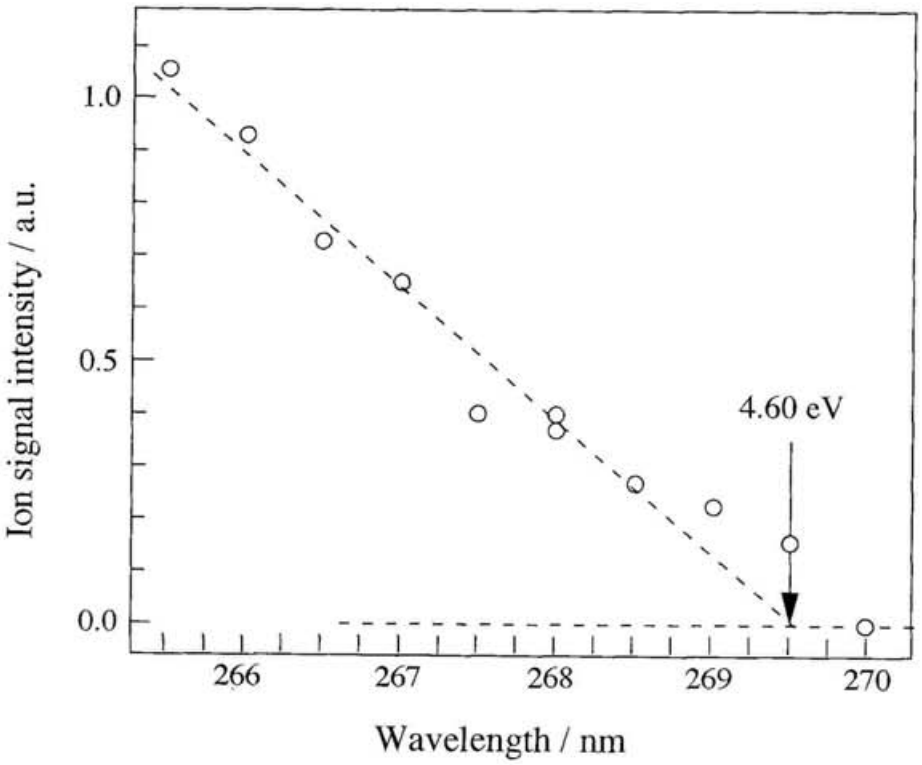

Figure V-13. Photoionization efficiency curve near the threshold for the production of ND_4^+. The pump laser wavelength was fixed at 193 nm, while the photon energy of the probe laser was scanned with a delay time of 700 ns. The photoionization threshold is shown by arrow.

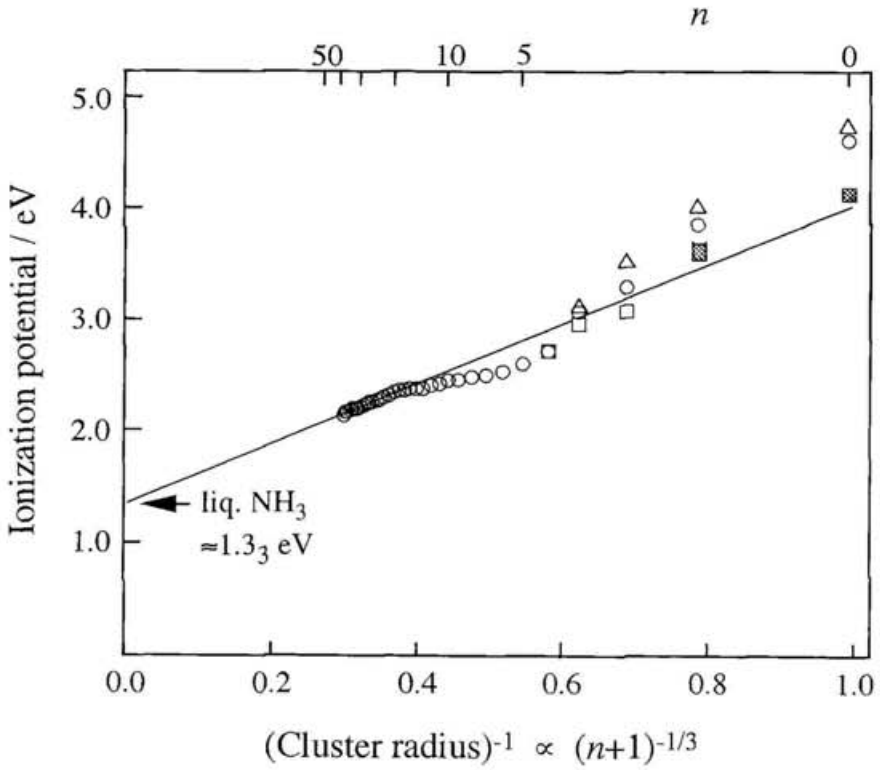

Figure V-14. Ionization potentials of $NH_4(NH_3)_n$ (n=0-35) plotted versus $(n+1)^{-1/3}$. The present results are indicated by open circles, while triangles and squares are the results referred from refs. [7,12] respectively. The estimated errors for the present IPs are ±0.03 eV. The result of least-squares fitting for n= 15-35 is also shown. The extrapolated value to $(n+1)^{-1/3}$ =0 ($n\rightarrow\infty$) is 1.33 eV. The correlation coefficient of the fitted line, r=0.987.

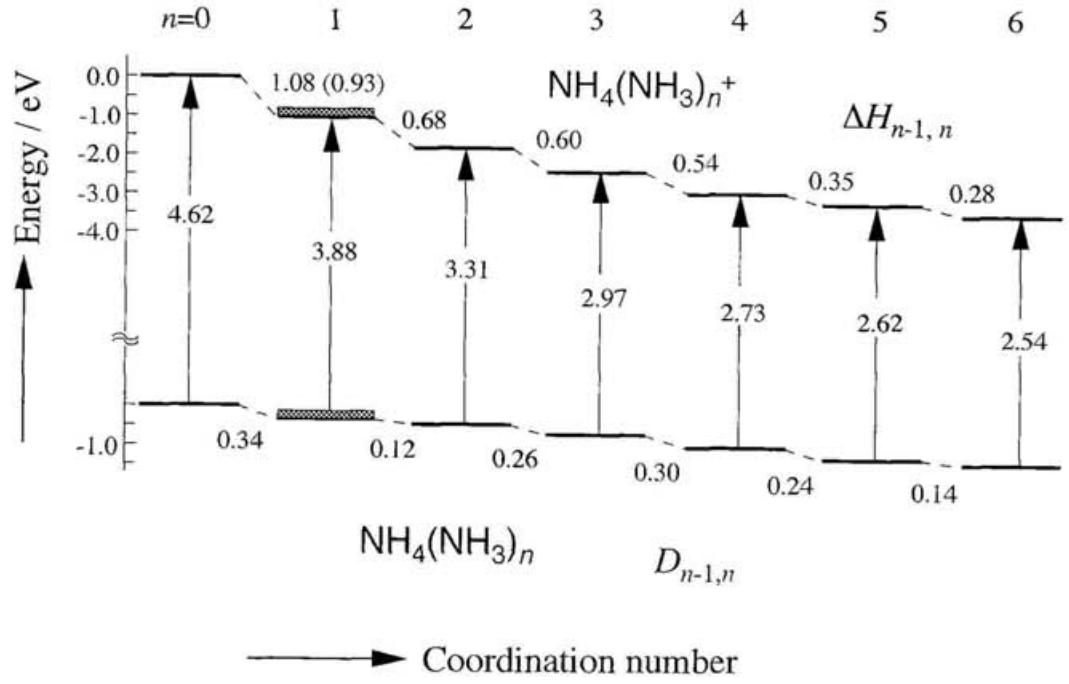

Figure V-15. The level structures for $NH_4(NH_3)_n$ (n=0-6). The binding energies of ammoniated NH_4^+ are cited from refs. [27,28]

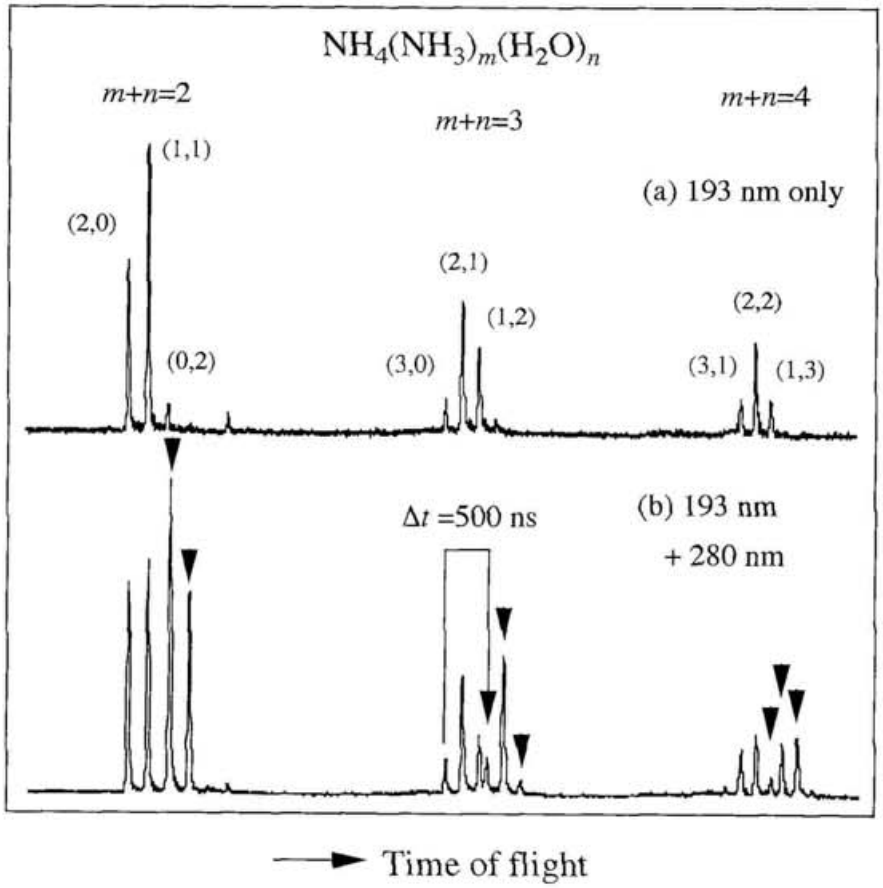

Figure V-16. Typical time-of-flight mass spectra of ammonia-water binary clusters. (a) The spectrum recorded by irradiation of 193 nm pulse alone. (b) Both 193 nm and 280 nm laser pulses are irradiated with a delay time of 500 ns. The peaks newly appeared by irradiation of 280 nm pulse are indicated by arrow.

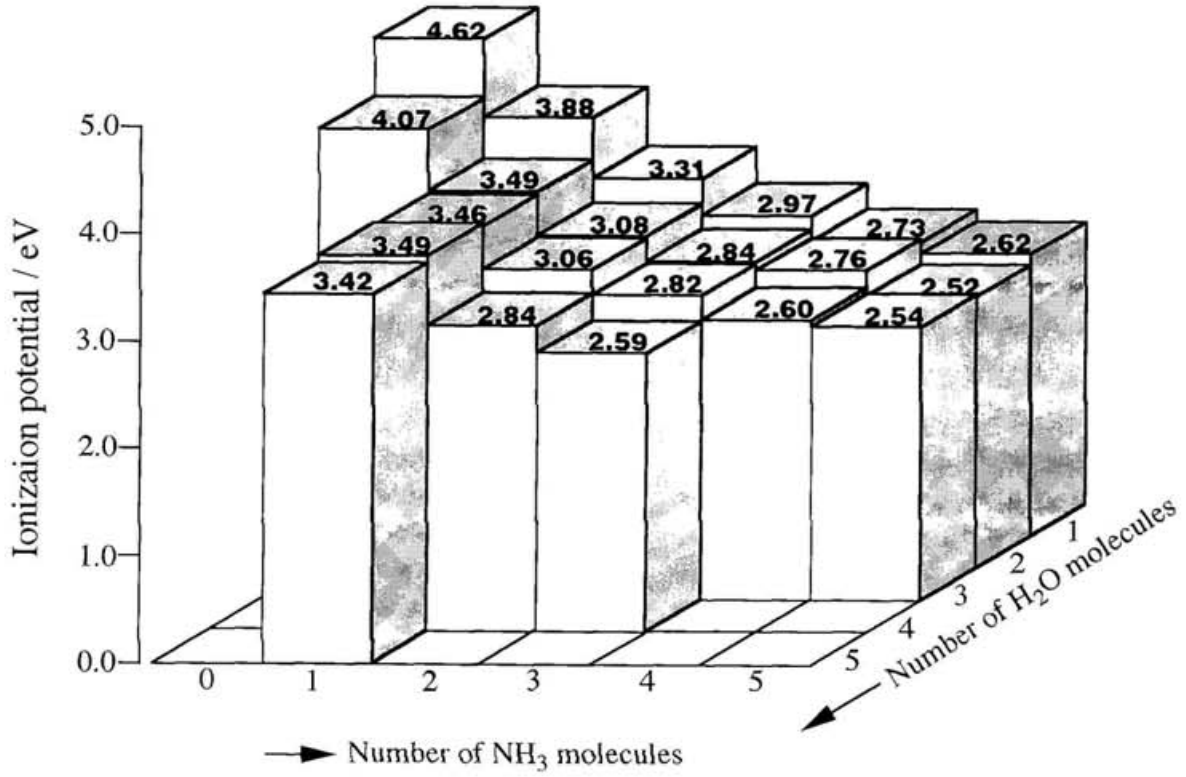

Figure V-17. Ionization potentials of $NH_4(NH_3)_m(H_2O)_n$.

Acknowledgments

The present work was carried out at Instrument Center of the Institute for Molecular Science (IMS) in the Okazaki National Research Institute and Kobe University under direction of Professor Kiyokazu Fuke. The author expresses his gratitude to Professor Fuke for continual advice and encouragement. The author also thanks to Professor Fuminori Misaizu (Tohoku University) for fruitful discussions and helpful advice. The author is grateful to Professor Kenro Hashimoto (Tokyo Metropolitan University) for providing the results of theoretical calculations and valuable suggestions. Special thanks are due to the members of the Instrument Center of the IMS and the stuff of the Equipment Development Center and the Chemical Material Center of the IMS for their grate assistance.

The author sincerely thanks to his family for ceaseless supports and encouragement. This issue is dedicated to them with his gratitude.

Early spring of 1997, in Kobe
TAKASU Ryozo